

Lawrence Radiation Laboratory
UNIVERSITY OF CALIFORNIA
LIVERMORE

UCRL-50230, Rev. 1

**RADIOACTIVITY RELEASED FROM
UNDERGROUND NUCLEAR DETONATIONS:
SOURCE, TRANSPORT, DIFFUSION, AND DEPOSITION**

Joseph B. Knox
Howard A. Tewes
Todd V. Crawford
Thomas A. Gibson Jr.

Foreword

This report first appeared in May 1967. The present edition has been slightly revised, but it still reflects the state of the art in 1967. The results of the Cabriolet, Buggy, and Schooner nuclear cratering experiments have led to significant advances in the last three years, but the theoretical approaches described in this report do not include this new information. Thus, although the basic work discussed in this report is still valid, it is obvious that a new report will be required to summarize our current experience in the production and distribution of radionuclides from nuclear cratering detonations.

Contents

Summary	1
Chapter 1: Introduction	4
Chapter 2: Methods for Estimating the Production and Distribution of Radionuclides from Nuclear Cratering Explosions	8
Chapter 3: Scales of Atmospheric Motion and Their Impact on the Fallout Problem	18
Chapter 4: A Cratering Fallout Model (KFOC)	24
Chapter 5: Fallout from Row-Charge Events—General Discussion	49
Chapter 6: Fallout from Row-Charge Events—Transisthmian Canal	52
Chapter 7: Dynamics of Nuclear Clouds	71
Chapter 8: Diffusion of Nuclear Clouds over Long Ranges	82
Chapter 9: Hot-Spot Mechanisms	99
References	105

RADIOACTIVITY RELEASED FROM UNDERGROUND NUCLEAR DETONATIONS: SOURCE, TRANSPORT, DIFFUSION, AND DEPOSITION

Summary

LRL's K Division is capable of predicting both the close-in external gamma-radiation field produced by a subsurface nuclear explosive and the concentration of airborne radionuclides at long ranges, including changes in the diffusion of the cloud. To elucidate our predictive methods, we present in this report the basis of and the most recent results from the computational physics models of the radionuclides produced (the source), the transport and simultaneous lateral eddy diffusion of the radionuclides initially in the stabilized cloud (the KFOC model), the development of the main nuclear cloud (the GEM and TENSOR models), and the two-dimensional atmospheric diffusion of the initial cloud through a time- and space-dependent diffusion environment (the 2BPUFF model). The calculated results have been compared to observed data in order to develop estimates of reliability as well as indications of key areas that need further investigation.

SOURCE

The radionuclides produced by the detonation of a nuclear excavation explosive come from fission, fusion, and neutron activation of the materials in the explosive and the surrounding rock or soil. Adequate means exist for estimating

the activities produced by fission. However, the principal products of the fusion reaction (e.g., tritium) are probably not known to better than 25%. The latest models for calculating activation products give estimates for the significant nuclides (^{24}Na , ^{54}Mn , ^{185}W , etc.) that are generally within a factor of 2 of observed data. Our results indicate that for calculations of external exposure due to fallout, more than 95% of the induced activity can be represented in the subsurface source (and later in the cloud source) by as few as five nuclides

FRACTIONATION

Fractionation—those processes that make experimentally observed ratios of nuclides in radiochemical samples different from the same ratios in the source—has been documented in the literature for subsurface detonations. Such processes can occur in the cavity, during venting, during cloud formation, and during transport. In Chapter 4, we present evidence and an interpretation indicating that if a significant amount of thermal energy is injected into the atmosphere during venting, then the radionuclides in the stabilized cloud are relatively unfractionated. In a gross sense, not only does the injected energy form a main cloud with

in-cloud circulations (or mixing), but these circulations apparently keep the particulates and gases mixed until the cloud stabilizes. If, however, little energy is vented (and no visible main cloud is formed), then fractionation can occur in the first several minutes. It should be clear that predicting the fractionated source in a stabilized cloud is still a problem. The most recent data suggest that fractionation is important primarily at ranges beyond that where 40- μ -diam particles land. This implies that useful predictions which neglect fractionation can be prepared for close-in fallout.

TRANSPORT

The KFOC cratering fallout model (published in 1964) is presented in Chapter 4 with the most recent information regarding the terminal fall velocities of clusters or ensembles of particles, the dimensions of stabilized clouds, the fraction of activity appearing in close-in patterns, and the relationship between activity and particle size. The model is normalized to Sedan for shots in moist but unsaturated alluvium and to Danny Boy for shots in hard, dry rock. In both cases, shot-time meteorology is used. An independent test case (Teapot Ess) is also presented. These results indicate that when shot-time meteorology is used, the prediction errors are about a factor of 2 in the external exposure (or exposure rate) as a function of distance along the "hot line." All three case studies indicate that after a few hours of cloud travel, the surface-zero winds at shot time are not representative, and thus positioning

errors are introduced into the fallout patterns. Two additional case studies are presented in which a dynamic wind-prediction model is used to calculate the wind that transports the debris during its fall to the earth. This model uses preshot meteorological information. In this limited sample, the positioning errors were reduced.

DYNAMICS OF NUCLEAR CLOUDS

After a review of the literature on numerical simulation of atmospheric convection (Chapter 7), the formation of main nuclear clouds is investigated via two of the codes in use at LRL—TENSOR and GEM. The GEM code was used to simulate the development of the Sedan main cloud in its observed meteorologic environment. The initial conditions for this problem—1 kt of energy coupled to the atmosphere during venting—were a result of our air-blast investigations. The calculated cloud geometry and rate of rise compare favorably with those observed. A further result, obtained from a parameter study, is that the maximum (in-cloud) vertical velocity scales according to the 0.25 to 0.20 power of the input thermal energy.

ROW CHARGES—TRANSISTHMIAN CANAL

The external gamma-exposure pattern from close-in fallout from row charges along the proposed routes of the Transisthmian Canal are calculated and presented in Chapter 6, together with a preliminary parameter study of various cloud heights and radii, wind speeds, and yields. This chapter also explores the

degradation of the prediction that occurs when complete ignorance of the wind in the lower 1000 m of the atmosphere is assumed. Such assumed ignorance can simulate either a real lack of information or an unreliable wind prediction in this layer. Even with the assumed ignorance, two-thirds of the patterns remained in the acceptable fallout sector. In the remaining cases, the particulates having appreciable fall rates and landing outside of the acceptable fallout sector stayed within a 3-hr travel time of the sector boundary. The parameter study is presented to illustrate the capability of the KFOC code and to suggest sensitive parameters that may warrant further investigation. In all of the numerical row-charge experiments, the worst instance of activity being deposited outside of the acceptable fallout sector involved an error of a factor of 2 in the predicted height of the cloud. A high cloud results in the injection of activity into a transport flow toward the islands in the Gulf of Panama. In Chapters 5 and 6, we identify key problems that need to be solved with regard to current feasibility studies (in progress by others).

ATMOSPHERIC DIFFUSION AT LONG RANGES

Chapter 8 discusses the diffusion of kilometer-sized clouds within a coordinate system fixed to the cloud's center over periods of a few days. Within this time- and-space framework, the sparsity of

upper-air observations forces the use of a diffusion theory to deterministically predict the time-dependent cloud concentration. The consequences of using diffusion theory within these time and space scales is discussed. A numerical cloud-diffusion model is developed that uses similarity theories of atmospheric turbulence to predict the horizontal diffusion of a cylindrical cloud and that permits vertical diffusivity to be varied as a function of height and time. Initial and time-dependent meteorological parameters need be specified only generally. Within this model, it is also possible to remove material from the diffusing cloud by assigning a deposition velocity to the cloud particles or by "scrubbing" the cloud with rain. A t^{-n} radioactive-decay option is also available. A sample problem is presented that exercises all of the various options in the computer code and illustrates the output of the code. Although the theories have not yet been validated by well documented case studies, they are consistent with the results of other diffusion studies.*

In Chapter 9, hot-spot-producing mechanisms are discussed and ranked. Our finding, which concurs with the literature, is that wet deposition (rainout involving nucleation and washout involving the removal of activity from the subcloud layer) is the primary producer of hot spots.

* Case studies of two reactor rocket tests and three Plowshare cratering experiments have been done since this report was first written.

Chapter 1:

Introduction

Joseph B. Knox

This report describes our current capabilities for predicting fallout from subsurface nuclear explosions as well as the reliability of calculated fallout fields. By "fallout prediction," we mean the calculation of close-in external gamma exposures* and exposure rates, as well as the more general problem of predicting the life history of radionuclides from the time of subsurface formation to the time of deposition on the earth's surface. Current capabilities include: 1) models for neutron-induced activities (soil and explosive), 2) empirical specifications of initial conditions in stabilized clouds, 3) models of atmospheric transport, diffusion and deposition of particles with radii larger than $10\ \mu$, and 4) methods of calculating airborne concentrations at long ranges.

Recently, some new research areas have become active: namely nuclear-cloud dynamics, analysis of the effect of medium (water content) on the initial conditions in a cratering fallout model, analysis of mechanisms bearing on natural hot spots, and numerical simulation of diffusion in the atmosphere at long ranges. In regard to these, we give their status, the preliminary results, and the key questions that still need to be answered.

We engage in applied research in order to reduce uncertainties in estimating effects from a given Plowshare application, to add depth to physical understanding, and,

*The term "external exposure" is hereafter referred to as exposure.

in some instances, to explore measures of control.

The mechanisms that are important in determining the rate at which radioactivity is injected into the atmosphere from subsurface nuclear detonations are shown in Fig. 1. This is the setting in which fallout processes have an impact on man. Man has been intentionally omitted from the diagram, for investigations of the effects on man are beyond the scope of this study. Our discussion is restricted to only a segment of the fallout problem: the source, venting, cloud formation, and atmospheric transport, diffusion, and deposition.

Our ultimate goal is to develop a capability for predicting isotopic airborne concentrations, surface isotopic deposition patterns for significant nuclides, and gross gamma fields. This includes:

- Atmospheric transport by a large-scale space- and time-variable wind field.
- Atmospheric eddy diffusion.
- Activity versus particle-size distributions for significant nuclides.
- Spatial fractionation in the initial cloud, if known.
- Initial cloud geometries for different detonation environments (dry, wet).
- Precipitation scavenging by rain cells either forming within the base-surge or main cloud or existing above and washing out gaseous and/or fine particulate radioactivity well downwind.

- Different released fractions for significant nuclides.

A summary of existing LRL models and efforts is given in Table 1, which cites the major capabilities of K Division as well as several significant contributions by members of the Chemistry Department. The earlier efforts were oriented towards predicting gamma exposures, including transient atmospheric transport and horizontal eddy diffusion. The effects of fractionation,* whether caused by venting, initial spatial distribution, or differential settling velocities, have received only nominal

*Fractionation is defined by Glasstone²⁵ as "any one of several processes, apart from radioactive decay, which results in change in the composition of the radioactive debris."

attention. Not until recently have proper source inputs and the model of atmospheric diffusion of a cloud moving through a varying diffusion environment been available. Such models should play an important role in data interpretation.

Although it may be common knowledge to the reader, the budget of the radioactivities produced and vented by a nuclear excavation explosion has never been closed—closed in the sense that activities held underground, those in throwout and close-in fallout, and those airborne to long distances have not been independently measured and their sum compared to the activity produced. As a result, there are several ways of specifying the activity in the initial cloud in our fallout models.

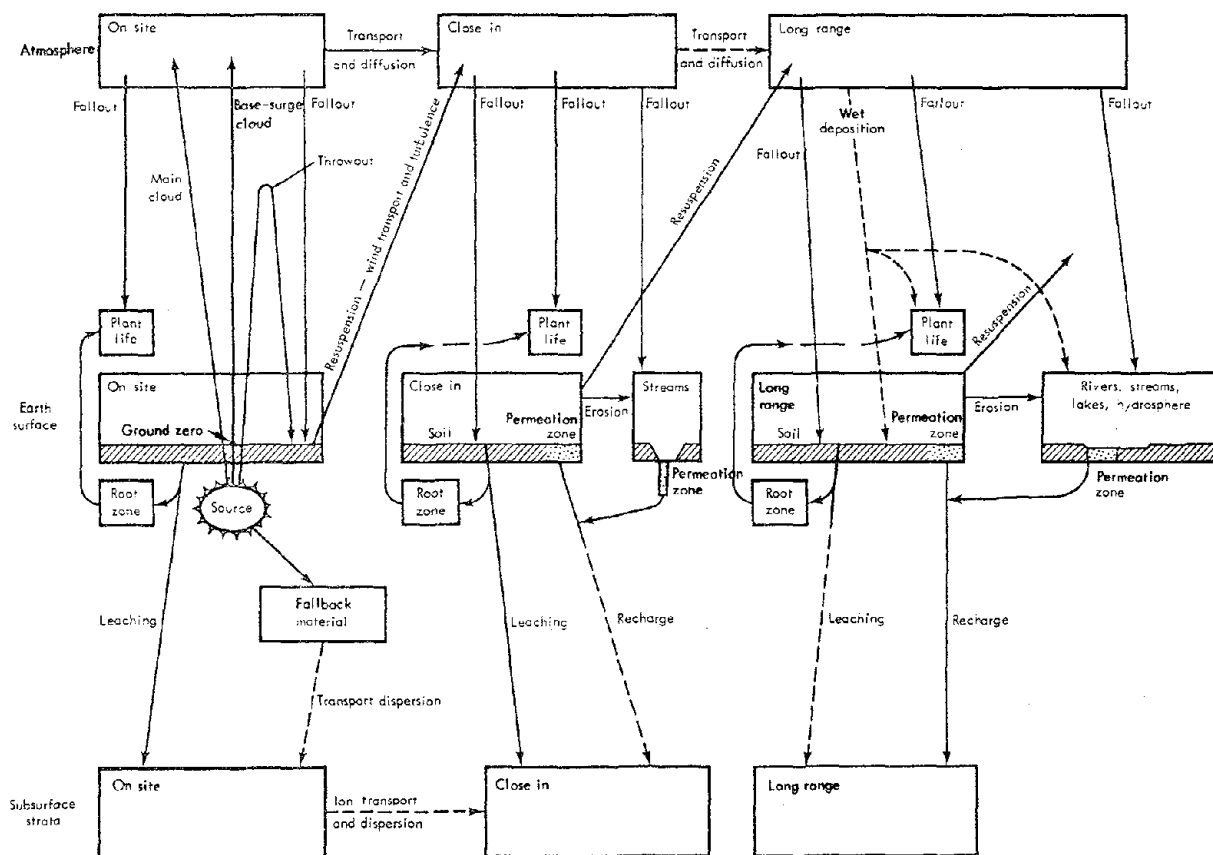


Fig. 1. Mechanisms important in determining the fate of radioactivity injected into the atmosphere from subsurface nuclear detonations.

Table 1. Existing models and efforts.

Investigator	Status	Description
A. V. Shelton ¹	Operational	FLIP — an early fallout-prediction code for gamma exposure rates, using empirical fall velocities but ignoring diffusion completely.
J. B. Knox ²	Operational	GROUNDHOG — a dynamic wind-prediction model for the mid-troposphere. With reasonable assumptions, the code can be used to predict a large-scale four-dimensional wind field in middle latitudes.
J. B. Knox ³	Operational	KFOC — a fallout-prediction code for gamma exposures or exposure rates, including the option of space- and time-variable horizontal wind fields, horizontal eddy diffusion, and spatial fractionation in the initial cloud (if known).
G. Higgins ⁴	Complete	Derivation of the normalization factor for unfractionated fission products — 3380 R/hr at one hour per square mile — and the terrain-shielding factor — about 0.8.
J. B. Knox and A. V. Shelton ⁵	Complete	Comparison of KFOC and FLIP.
M. M. Williamson ⁶	Complete	Comparison of KFOC and FLIP.
T. A. Gibson ⁷	Complete	Comparison of KFOC and FLIP.
T. V. Crawford ⁸	Complete	Prediction and sampling of nuclear clouds from the viewpoint of diffusion theory.
T. V. Crawford ⁹	Operational	2BPUFF — a long-range atmospheric-diffusion code capable of predicting relative concentrations in a cylindrical cloud as the cloud moves through a varying diffusion environment. Radioactive decay and dry and wet deposition are included. At present, the cloud is <u>not</u> explicitly subjected to vertical wind shear.
J. B. Knox ¹⁰	Preliminary	Cloud rise and cloud dimensions.
J. B. Knox and R. Rohrer ¹¹	Preliminary	Cloud dimensions at cloud stabilization. Summarized in Ref. 3.
J. T. Cherry ¹²	In development	Cratering physics and calculation of late-time cavity pressures for comparison with main-cloud growth.
H. A. Tewes ¹³	—	Source-released fractions for significant nuclides.
R. E. Heft and J. S. Kahn ¹⁴	In development	Particle-analysis program.
R. E. Heft ¹⁵	In development	Activity as a function of fall speed for significant nuclides in the Palanquin, Sedan, and Cabriole Events.
J. B. Knox, T. V. Crawford, and H. Ellsaesser ¹⁶	Preliminary	Scavenging of particulates and gases in the base-surge cloud. Oriented toward the Panama Canal.
T. A. Gibson ¹⁷	Operational	Calculation of probability distributions for gamma exposures from given climatological data.
A. Foldvik and M. G. Wurtele ¹⁸	Operational	Model of air flow over arbitrary terrain under arbitrary atmospheric conditions.
J. Vieceili ¹⁹	Preliminary	Numerical calculation of atmospheric effects from the explosion of a 500-Mt device at the surface of the earth.
J. A. Miskel ²⁰	Complete	Characteristics of radioactivity produced in a nuclear explosion.
R. A. James ²¹	Complete	Calculation of radioiodine concentrations in milk.
N. A. Bonner and J. A. Miskel ²²	—	Distribution of radioactivity from cratering in basalt.
J. A. Miskel ²³	—	Radioactivity study for Project Sulky.
R. A. James and E. H. Fleming ²⁴	—	Relative-significance index of radionuclides for canal studies.

Tested Methods

1. Assume an unfractionated fission source for an all-fission explosive or the equivalent kilotons of fission for a thermonuclear explosive. The fallout model is used to calculate the fraction of the source deposited per unit area at different points in the pattern. The fraction deposited is converted to an exposure or exposure rate by using the constant 3380 R/hr per square mile per kiloton of fission, a shielding factor of 0.74, and the released fraction of the activity as a function of the scaled depth of burial. The total radioactivity produced by a nuclear detonation was used in early fallout models; the source treatment noted above has been in use since 1960.
2. Calculate (as discussed in Chapter 2) the activities produced by the device. Using an assumed or measured (if available) vented fraction for each significant nuclide, (a) estimate the equivalent kilotons of fission on par-

ticulates (radius $\geq 10 \mu$) for input to KFOC, and (b) calculate the activity for gaseous or fine-particulate nuclides for input to 2BPUFF.

Proposed and Untested Methods

1. Assume that the measured activities versus fall speeds for significant nuclides are valid for the explosive in question and combine this data with calculations of the activities produced. (This method is untested, and experimental numbers are not yet available.)
2. Given (a) the activities produced by the explosive, and (b) the vented fraction for each significant nuclide, obtain the equivalent fission yield. Assuming a mass/particle-size distribution and a fractionation function, the gamma intensity might be computed from the mass deposition and particle-size information at arbitrary points in the pattern. (This method is untested, and data are not yet available).

Chapter 2:

Methods for Estimating the Production and Distribution of Radionuclides from Nuclear Cratering Explosions

Howard A. Tewes

RADIONUCLIDE PRODUCTION

Model (Sources of Radionuclides)

Fission Products

Although fission-product yields vary as a function of the fissioning nucleus and are sensitive to the energy spectrum of the initiating neutrons, existing studies²⁶⁻²⁸ enable adequate estimates to be made of fission-product production in nuclear excavation devices.

Neutron-Activation Products: Device Components

In this document, "device components" include those portions of a thermonuclear explosive that can be subjected to very high time-integrated neutron fluxes. Radionuclide production in these components can be extensive.* Materials farther away from burning thermonuclear fuel are exposed to somewhat lower time-integrated neutron fluxes; hence, first-order reactions predominate in the production of radionuclides.

Neutron-Activation Products: Canister and Soil

Activation products formed at relatively large distances from neutron sources con-

sist primarily of those made by neutron capture. Since nuclear excavation devices have been envisaged to include a fairly thick neutron blanket (probably boric acid) inside the canister, the neutron spectrum incident upon the canister (and soil) will be relatively deficient in low-energy neutrons, and some threshold reactions will be induced in the canister and inner layer of soil. However, the neutron spectrum "softens" rapidly in the soil, thus causing the overall predominance of (n, γ) reactions.

Calculations (Codes and Procedures)

Computation of Neutron Fluxes

High-Flux Regions—Neutronic calculations may be made of the explosion phase of a thermonuclear device using neutron-diffusion or Monte Carlo computational techniques. Current versions of computer programs using these techniques not only provide for the calculation of neutron fluxes as a function of time (divided into a number of energy groups) in any region included in the problem, but also allow the calculation of nuclide production from multiple reactions occurring in any region.

Existing codes also provide for the estimation of the total number of neutrons emitted from the outermost region included in the problem, again as a function of time and divided into several energy

*For the sake of completeness, multiple neutron-induced reactions that produce radioisotopes far from the stability curve²⁹ are also considered in this report.

groups. Thus, these codes produce a "source term" for additional calculations of relatively low neutron fluxes farther away from the device.

Low-Flux Regions—The number of neutrons emergent from the outermost region considered by the neutronics code is used as input to a Monte Carlo calculation of neutron diffusion into the environs of the neutron source. The Monte Carlo code that is employed in this calculation³⁰ estimates the total number of neutrons deposited in various regions in the vicinity of the source. The output does not directly give the neutron deposition in the various zones about the source; rather, the energy deposition is reported. Hence, the neutron fluxes in the regions of interest must be calculated by hand.

Computation of Cross Sections for Neutron-Induced Reactions

Although a large number of experimentally determined cross sections and excitation functions are available for neutron-induced reactions (see Refs. 31, 32, and 33), neutron cross sections for those nuclides that are involved in the multiple reactions occurring in high-flux regions are not easily measurable and are not available at this time. Hence, appropriate codes are under development to calculate these needed cross sections.

Brancazio's code³⁴ has been used to estimate threshold reaction cross sections. However, inasmuch as this formulation does not explicitly include competition from photon emission, a more adequate code is being constructed.

Truran's BARNCAL code³⁵⁻³⁷ embodies a number of the features of Brancazio's work. For example, the total reaction

cross section is calculated as the sum of contributions from individual neutron resonances at lower energies, and hence it naturally approaches the total inelastic cross section at higher energies. Branching ratios are calculated via the usual statistical theory; the appropriate Coulomb function is used where charged particles are emitted. At low energies ($E_n \leq 1$ MeV), only neutron and radiation widths need be considered; at higher energies, other contributions must be taken into account.

Calculations using BARNCAL are not far advanced, for the code is not yet in final form. Hence, activation estimates to date have been made with hand-calculated approximations.

Activation Calculations

High-Flux Regions—Because of the incidence of multiple reactions in high-flux regions, it has been necessary to develop a "bookkeeping" code to keep track of the nuclide buildup and "depletion" in such regions. Essentially, the code employs a calculated neutron flux at appropriate time intervals during the burn and, using neutron cross sections in the region of interest, calculates the nuclidic composition within the region as a function of time. The availability of an extensive nuclide grid allows multiple reactions to be calculated even with multi-isotopic elements.

Three codes have been developed for this nuclide-accounting operation. The first, NOVA,^{29,38} was originally written to obtain a predictive capability for heavy-element production in uranium targets subjected to intense neutron irradiation during the detonation of a nuclear device. It has since been slightly rewritten to allow

its use with other elements. The second code, WATUSI, is an outgrowth of NOVA. It is designed to utilize more of the neutron-flux data produced by the neutronics codes in order to give a more accurate estimate of nuclide production in regions of especially high flux. The third code, ACT,³⁹ was written for the purpose of determining nuclide production in thermonuclear explosives. It is capable of calculating the radioactive decay of the radionuclides formed.

Low-Flux Regions—Since only single-order reactions are considered in low-flux regions, a much simpler accounting code is required. For instance, there is no need to consider the buildup of nuclides as a function of time. Thus, the output of a Monte Carlo calculation can be coupled with the appropriate compilation of neutron cross sections to obtain the desired result (i.e., a list of nuclides produced in low-flux regions).

The ACTIVE code^{40,41} has been developed to perform this computation as well as to calculate the radioactive decay of the radionuclides formed. It is capable of simultaneously calculating the activation products in all of the regions used in the Monte Carlo computation and then producing a comprehensive compilation of radionuclides, automatically summing those produced in more than one region.

Experimental Checks

The adequacy of the predictions obtained from the calculational procedures outlined above can be tested by comparing them with measured values for radionuclide production. There are two difficulties that contribute to the difficulty of such a test. First, there are uncertain-

ties in the chemical analysis of a device and its environs. This is especially true of past tests, where the need for careful sampling of device materials and soil prior to detonation was not recognized. Second, and more important, the chemical fractionation occurring in vented or contained underground detonations is extreme for some elements, thus making an accurate estimate of the total production of certain radionuclides extremely difficult.^{22,42-44} Consequently, although the calculational check obtained by examining experimental results may be at least semiquantitative for the so-called refractory elements, the data relating to the more volatile elements will probably be relatively unusable for such verification purposes.

Future Developments

Continued Development of Cross-Section Codes

Although the development of an adequate code (BARNCAL) for calculating neutron cross sections is relatively far advanced, some refinements are still being made in the required input. When the code is fully operational, presumably only the atomic number (Z) and mass number (A) of the target nucleus will be needed. In addition to code development, code checking (i.e., the correspondence of calculated cross sections with measured values) still needs to be done.

Continued Modification of Activation Codes

The ACT code is presently used to calculate the production of radionuclides in high-flux regions. It is being reprogrammed to accept the output of a Monte

Carlo neutronics code, and its memory is being enlarged by transferring it from the IBM-7094 to the CDC-6600.

Past Events—A number of device tests exist in which meaningful checks could be made on our current calculational ability for internal device activation. Although the chemical analyses of device components for these tests are not as complete as desirable, adequate calculations could probably be performed nevertheless. The first step in the computational sequence would involve rerunning the appropriate neutronics problems, using device yields that are consistent with the radiochemical diagnostics. The neutron fluxes obtained in this way would then be used as inputs to NOVA or ACT.

Current and Future Events—Underground tests of "clean" devices or prototypes of excavation explosives are certainly prime candidates for calculational tests, as are any cratering events. A continuing examination of proposed tests is indicated so that nuclide yields from other suitable devices can be computed and checked.

DISTRIBUTION OF RADIOACTIVITY*

Model

Butkovich^{46,47} has developed a method of estimating the composition of the cavity gas prior to venting for the detonation of a nuclear device buried at cratering depth. Applying this model (which involves complete mixing of the vaporized, melted, and strongly shocked regions surrounding the detonation site) to silicate rock containing 1% water leads to an environment consist-

ing of melted SiO_2 dispersed in superheated steam at a volume ratio of about 1:100 ($\text{SiO}_2:\text{H}_2\text{O}$). The assumed cavity pressure at this time is 1 to 2 b, and the temperature is about 1800°C . In the case of a more nearly saturated medium (10% water), the $\text{SiO}_2:\text{H}_2\text{O}$ ratio would be more nearly 1:200, the cavity pressure would be 10 to 20 b, and the temperature would be about 2000°C . At these postulated temperatures and pressures, a number of radioactive chemical species (such as niobium, zirconium, yttrium, rhodium, etc.) would have already condensed⁴⁸ and would presumably be associated with the liquid SiO_2 .

Thus, prior to the passage of the cavity gas through the overlying rock, the amount of water in the detonation environment would not appear to have a large effect on the composition of the cavity gas or on the physical state of the radionuclides contained in the gas. However, the gross features of the actual venting (or passage of gas through the "filter bed" of overlying rock[†]) would be considerably different for the two cases outlined previously. For dry rock (1% water), the gas would expand little, if at all, since the pressure relief would be balanced by the cooling of the

[†]One description of the venting process pictures the material overlying the expanding cavity as a filter bed through which all of the radioactive material must pass. Alternative descriptions of the venting process involve different treatments of the details of the passage of cavity material through the overlying layer. All descriptions, however, include an interval during which the overburden interacts with the cavity material. The result of this process is not inconsistent with that which would be produced by filtration of the venting material, hence the term "filter bed."

*A similar treatment of radionuclide partition has been independently published (see Ref. 45).

gas. Therefore, the venting material would have little energy available for pdV work, and almost all of the condensed refractory radionuclides (as well as the liquid silica) would be deposited on the large particles of overburden. Thus, these substances would be found in the local fallout field rather than in the cloud of gases and fine particulates. Presumably, the more volatile radionuclides (i.e., those still in the vapor phase at the time of venting) would condense on the surface of the filter-bed material and would be distributed relatively evenly over the area of the particles found in the cloud and the fallout. Consequently, the specific activity (atoms of radionuclides per gram of inert material) of the volatile radionuclides would be higher for the smaller particles than for the larger ones in the ratio of surface area to volume. Due to the effectiveness of the filter bed in this instance, a large fraction of the surface-deposited material would probably be trapped and deposited as fallout. However, since the cloud would still contain some of the finer particles, it would display a significant content of "volatile" radionuclides or those having volatile precursors, such as antimony, tellurium, cesium, etc.

On the other hand, the gas venting from saturated rock (10% water) would be much more violent, resulting in a well mixed "aerosol" of rapidly cooling silica, water vapor, and crushed overburden. Consequently, the radioactive cloud would contain considerable amounts of refractory radionuclides.⁴⁹ Again, the refractory elements would be "volume-contained," whereas the volatile elements would be surface-deposited. Due to the turbulent

mixing of all vented particulates, both the refractory and the volatile species should be present in the stabilized cloud to about the same extent. However, since the material comprising the so-called "filter bed" would be well pulverized by venting material that has a large amount of energy available for pdV work, the refractory species would be associated with particles having a smaller mean radius than those resulting from a detonation in dry rock.

Chemical Fractionation: Fallout and Cloud

The description of venting in the preceding section underlines the comment of Bonner and Miskel²² that the terms "fraction out" or "percentage vented" must be carefully defined when applied to radioactivity releases from cratering events. Certainly, the processes hypothesized above would produce significant differences in the "fractions out" of the various radionuclides formed in a cratering detonation. However, Gibson's study⁵⁰ of three cratering events shows only moderate variability (factors of 3 or 4) in fractions of different radionuclides deposited in close-in fallout. Thus, it is not surprising that the decay of the fallout gamma field fits a t^{-n} dependence, where n is about 1.3 for the events considered by Gibson. Naturally, this t^{-n} decay will not necessarily apply where neutron-activation products form a large fraction of the fallout. Consequently, it is possible to define a "fraction of total activity" in the fallout field by integrating the actual radiation field at a given time after the detonation and dividing the result by the expected field resulting from the uniform deposition of all radionuclides produced by the detonation.

Where the radioactive cloud is concerned, the term "fraction out" can be applied only to individual radionuclides because of the extreme fractionation that can occur, especially in the case of a detonation in dry rock. Consistent with the model proposed on p. 11, the Danny Boy cloud was rich in volatile species; thus, fine particles and gases were predominant in the cloud. On the other hand, the Sedan cloud showed little fractionation in the samples taken at H + 8 min (shortly after stabilization); the study reported by Heft¹⁵ showed that both the gross and the specific gamma activity varied little (factors of 3 or 4) with the particle size. However, consistent with the model discussed earlier, the refractory nuclides (⁵⁴Mn, ⁶⁰Co, ⁸⁸Y) predominated in the larger particles, while the fine particles were rich in "volatile" species (such as ¹³⁷Cs).

Of course, the cloud composition is indicative of the "far-out" fallout; hence, such fallout should be rich in volatile species. This conclusion agrees with the experimental results for Sedan as reported by Krey and Fried⁵¹ and by Mark et al.⁵²

While we are discussing chemical fractionation, it is in order to examine the state of knowledge regarding a few nuclides that are of interest because of their biological importance. In many cases, the observations regarding these nuclides will reiterate the more general considerations previously included in this section.

Both ⁹⁰Sr and ¹³⁷Cs appeared to be slightly enriched (with respect to the refractory nuclides) in the close-in fallout from Danny Boy, and they were also greatly enriched in the late-time cloud.^{22,50}

Sedan radiochemical studies^{42,53} showed little or no fractionation in the close-in fallout and an enrichment of a factor of 10 in the late-time cloud. Thus, as a first approximation, these radionuclides are unfractionated in the local fallout. The amount in long-range fallout should be sensitive to the medium in which the explosive is detonated, as has already been discussed.

The distribution of ¹³¹I is not as well documented as that of ⁹⁰Sr and ¹³⁷Cs. No data were obtained from Danny Boy,²² and only inconclusive results were obtained from Sedan.⁵³ Some of the data on the Palanquin close-in fallout⁵⁴ indicate little or no fractionation, but no reliable data were obtained on ¹³¹I concentrations in the late-time cloud. Due to the rather atypical nature of the Palanquin Event (as related to its cratering mechanism), radiochemical data from this shot should not be weighted too heavily.

In summary, it is suggested that the approach of James²¹ be used on the ¹³¹I problem. That is, as a first (and conservative) approximation, it should be assumed that this nuclide does not fractionate severely from other fission products.

Chemical Fractionation: Tower Versus Cratering Detonations

As has been shown experimentally, the critical parameters required for the delineation of chemical fractionation are the particle-size distribution produced by a nuclear detonation and the distribution of the various radionuclides as a function of particle size. If the latter parameter is assumed to be somewhat similar for both cratering and tower detonations (i.e., the

refractory species are volume-deposited and the volatile species are surface-deposited), then the nature of the particle-size distribution is critical in evaluating observed chemical fractionation. Thus, specifying the mean particle size (or the natural logarithm of the mean particle radius, $\ln \bar{r}$), the standard deviation (σ) of this quantity, the fraction (w) of all particles present in the close-in fallout that are described by this function, and the fraction (F_c) of the total radioactivity deposited in the close-in fallout should not only provide a first approximation at describing chemical fractionation, but also enable the intensity of the fallout field to be estimated well by the KFOC code.*

Table 2 gives values for some of the above quantities that have been used to calculate fallout fields in four different events.† With regard to far-out fallout (or those radionuclides contained in the nuclear cloud), Table 3 provides a summary of information pertaining to the same four events.

Obviously, the tower detonations show values of F_L that are larger by a factor of 30 to 90 than those for cratering events. The radioactivity present in nuclear clouds from either cratering or tower detonations must be associated with particles having an $\ln \bar{r}$ significantly smaller than the $\ln \bar{r}$ characteristic of the parti-

cles deposited as close-in fallout. It can be postulated that the size distribution of such particles could be characterized by an $\ln \bar{r}$ as small as those observed in the Sedan cloud.

From the foregoing argument, it can be seen that any direct comparison of fractionation and/or radioactivity distribution between tower and cratering detonations (especially at long ranges) must be made only with severe restrictions and reservations.

Predictive Capability

At present, only an empirical curve (see Fig. 2) is available to estimate the fraction of the total activity produced in a cratering event that is deposited in close-in fallout.** Information on the total amount of radioactivity present in the cloud after the deposition of local fallout is based almost entirely on the minimal cloud-sampling activities associated with the Sedan, Danny Boy, and Neptune Events. Thus, current long-range fallout prediction can be accomplished only by scaling from the results of one of these three events, and it is not now possible to confirm the effects that changes in the device environment may produce.

It should be noted from Fig. 2 that events detonated in different media (though at about the same scaled depth of burial) display wide variations in values of F_c . For example, Sedan apparently deposited about 18% of the activity produced as close-in fallout, with the corresponding deposition being only 4% for Danny Boy.

*See Chapter 4 for a full description of this code.

†It should be noted that the KFOC calculations that have been made for these events specify two different particle distributions, each of which is described by an assignment of characteristic values of the above parameters. Only the predominant particle distributions for each event have been included in Table 2.

**"Close-in" fallout is defined in this paper as that which is carried on particles larger than 10μ in radius. It can therefore be treated with the KFOC code.

Table 2. Particle-size parameters for close-in fallout.

Event	Type of shot	F_c	w	$\ln \bar{r}$	σ
Sedan ^a	Cratering	0.18	0.9	3.8	0.69
Danny Boy ^a	Cratering	0.04	0.9	3.0	0.69
Apple II ²	Tower	0.03 to 0.1	0.95	3.8	0.69
Zucchini ²	Tower	0.03 to 0.1	0.95	3.8	0.69

^aSee Chapter 4 of this report.

Table 3. Nuclear-cloud parameters.

Event	F_L^a	$\ln \bar{r}$
Sedan	0.03	~ 3.2 (1.0) ^b
Danny Boy	$\sim 0.01^c$	—
Apple II	0.9 to 0.97	—
Zucchini	0.9 to 0.97	—

^a F_L = fraction of total activity in the cloud several minutes after the time of stabilization. This parameter was experimentally determined for the cratering detonations. For the tower detonations, it was assumed that all radioactivity not accounted for in the close-in fallout was present in the cloud.

^bEstimated from Ref. 15. The principal particle distribution had an $\ln \bar{r}$ of about 3.2 for the early cloud sample (taken at H + 8 min). The late cloud sample (taken at H + 75 min) was characterized by a particle distribution having an $\ln \bar{r}$ of about 1.0; at that time the value of F_L was about 0.01.

^cIn the case of Danny Boy, measured values of F_L for individual radionuclides varied from 0.0011 to 0.13.

Again, Neptune gave an F_c of 0.3%, whereas Sulky (at the same scaled depth of burial) deposited less than 0.1% of the total activity produced. In both of these sets of events, the larger F_c was observed for the device emplaced in the medium having the largest water content, which is consistent with the model outlined on p. 11. However, partly because of the paucity of

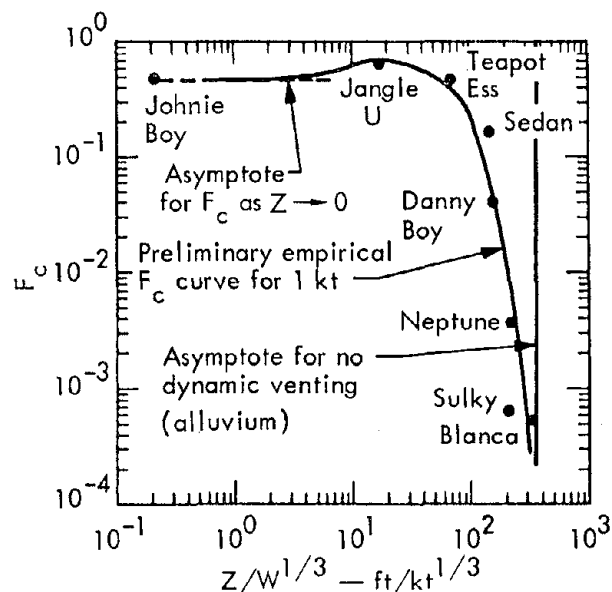


Fig. 2. Fraction of gamma activity appearing in close-in fallout patterns (Z = depth of burial, W = yield).

the experimental data, it is not possible at this time to develop a dependable means of predicting F_c . It is conceivable that one or more other variables in the device environment may have a significant effect on F_c . Elucidation of the activity-release mechanism will definitely require a number of suitably designed nuclear cratering experiments.

If anything, the situation with respect to predicting long-range fallout (late-time cloud burdens) is even less satisfactory than the problem of predicting close-in

fallout. The minimal number of cloud penetrations made for Danny Boy (four) and Sedan (three) do not characterize the radionuclide cloud burdens, concentrations, or particle-size distributions with sufficient accuracy to enable even an approximate scaling prediction to be made with any degree of confidence. Cohen⁵⁵ has shown that, especially in the case of Danny Boy, estimated cloud burdens can easily be in error by an order of magnitude.*

The fraction of radioactive debris that is trapped in the throwout and fallback has never been measured well, and it is generally inferred by difference (i.e., total radioactivity minus that observed in the fallout and the cloud). Obviously, then, the previously discussed uncertainties in the prediction of fallout and cloud burdens are reflected in the indeterminacy of the radionuclide concentrations in and around the crater, although Tami and Day⁵⁶ have made estimates of dose rates within the nuclear crater and lip.

Future Requirements

Development of a Predictive Capability for F_c

Present techniques for measuring fallout fields are sufficiently accurate to establish the F_c for a given detonation to within about $\pm 25\%$. However, in order to develop any theoretical model for esti-

*Recent cloud-sampling programs carried out in conjunction with the Cabriolet and Buggy cratering detonations have permitted a satisfactory estimate to be made for both cloud burdens and the statistical uncertainties of such determinations.

imating F_c , it is first necessary to accumulate considerable experimental data from cratering events carried on in a variety of media and to attempt to correlate this data with the model proposed on p. 11. Until such a program is implemented, there is no adequate method whereby F_c can be predicted other than possibly in a dry shot environment.

Development of a Predictive Capability for Long-Range Fallout

The development of a predictive capability for long-range fallout (and late-time cloud burdens) can be attained by a two-pronged approach:

- In the absence of nuclear cratering events, some understanding of cloud structure and diffusion could be attained by studying, say, radioactive clouds from tests of nuclear rocket engines.[†]
- Collection of relatively long-distance fallout samples should be attempted. This implies the recovery of particulate material from relatively large ground areas. The results should be correlated with existing data obtained with ground-based air samplers, and the particle-size distributions in such samples should be determined.**

[†]Such a program was successfully implemented recently. The methods used and the results obtained are reported in Refs. 57 and 58.

**This program has been successfully carried out in conjunction with both the Cabriolet and Buggy cratering events. The data are still being evaluated.

Again, the measurements that have been previously described should be carried out in detail for the same series of cratering events as has been proposed above. Because of the large apparent differences in the cloud burdens (both in terms of fractions of the total production of individual nuclides and the fractions of total radioactivity produced) between Danny Boy and Sedan, it appears that long-range fallout is at least as sensitive to differing detonation environments as close-in fallout (which is predicted by the proposed model previously discussed).

Development of a Predictive Capability for the Fraction of Activity in Throw-out and Fallback

This goal can be attained by successfully achieving the preceding two requirements. However, in order to obtain a "radioactivity inventory balance," it would be desirable to conduct a carefully designed program of crater and throwout sampling in each of the nuclear cratering events previously proposed. Such a sampling program should be planned for execution soon enough after each event so that redistribution of the radioactive species by weathering is minimal.

Chapter 3:

Scales of Atmospheric Motion and Their Impact on the Fallout Problem

Joseph B. Knox

Even a casual observer of the atmosphere realizes that disturbances in the wind field span many orders of magnitude, from the scale of winter storms (a few thousand kilometers) to the scale of molecular diffusion (1 mean free path at sea level is 5×10^{-6} cm). By measuring the wind components from these scales, we see that the surface wind is a highly variable quantity—or that the atmosphere is a turbulent medium. Table 4 summarizes

some of the scales known to the atmospheric physicist. This table also gives examples within each scale category: the horizontal scale, the vertical scale, the order of magnitude of the vertical velocity (w) associated with each scale, and an estimate of the time scale of the circulation element.

It is useful to illustrate some of the less familiar mesoscale systems referred to in Table 4.

Table 4. Scales of atmospheric motion.

Scale name	Typical element	Horizontal scale (km)	Vertical scale (km)	$ w / v_h ^a$	$ w $	Time scale	Remarks
Planetary	Long waves of westerlies	10,000	~20	~0.0001	~0.001	Several days	
Synoptic	Major storm systems: a) hurricanes b) vertical circulations normal to fronts	~1,000	~20	0.001 to 0.01	0.1 near fronts, 0.01 elsewhere *	2 to 4 days	Terminal velocity of a fallout particle ($\rho = 2.5$, $r > 20 \mu$) is ≥ 0.1 m/sec
Mesoscale	Squall lines: a) waves b) tornados c) land/sea-breeze effects	10 to 100	5 to 10	0.1 to 1.0	10 ~10 ~5	2 to 10 hr	
Convective	Showers	1 to 10	1 to 10	~1.0	10	~1 hr	
Subconvective	Boundary layer	—	—	~1.0	—	<1 hr	
Molecular diffusion	—	1 mean free path = 5×10^{-6} cm	—	—	—	—	

^a w = vertical velocity, v_h = vertical scale.

EXAMPLE 1: THE BIFURCATED SEA BREEZE IN THE LOS ANGELES BASIN

Under certain conditions, the daytime sea breeze in the Los Angeles Basin is split by the Santa Monica Mountains into two flows: 1) one that is relatively smog free entering the San Fernando Valley from the west, and 2) a second one entering the Los Angeles Basin from the west, moving over the city, and entering the San Fernando Valley from the southeast, bearing the smog injected enroute. By the time the two parts of the sea breeze meet in the Valley, they have quite different state parameters and levels of pollution. Through measurements of the wind and state parameters on an appropriate scale, Edinger⁵⁹ has acquired data on this phenomena and has calculated the air-parcel trajectories relative to the line along which the two parts of the sea breeze meet (see Fig. 3). The stippled area depicts the trajectories carrying the smog-laden air from a shallow layer next to the earth, then vertically upward along

the wind-shift line, and finally into the return flow aloft. In this example, the smog serves as a tracer confirming Edinger's diagnostic calculations, which show that the prediction made from the scale analysis in Table 4 is correct—that horizontal and vertical wind speeds have the same order of magnitude in mesoscale systems.

EXAMPLE 2: THE TRANSVERSE MOTION IN AND NEAR FRONTAL ZONES AT MIDDLE LATITUDES

Under certain simplifying assumptions, the transverse motion in a plane normal to a frontal zone can be calculated from hydrodynamic equations and an appropriate description of the state parameters of the atmosphere. Todsén⁶⁰ has performed such a calculation, including the effect of the release of latent heat of condensation on the transverse wind field. The theoretical rates of precipitation, derived from the above, compare favorably with the observed rates of precipitation. Figure 4

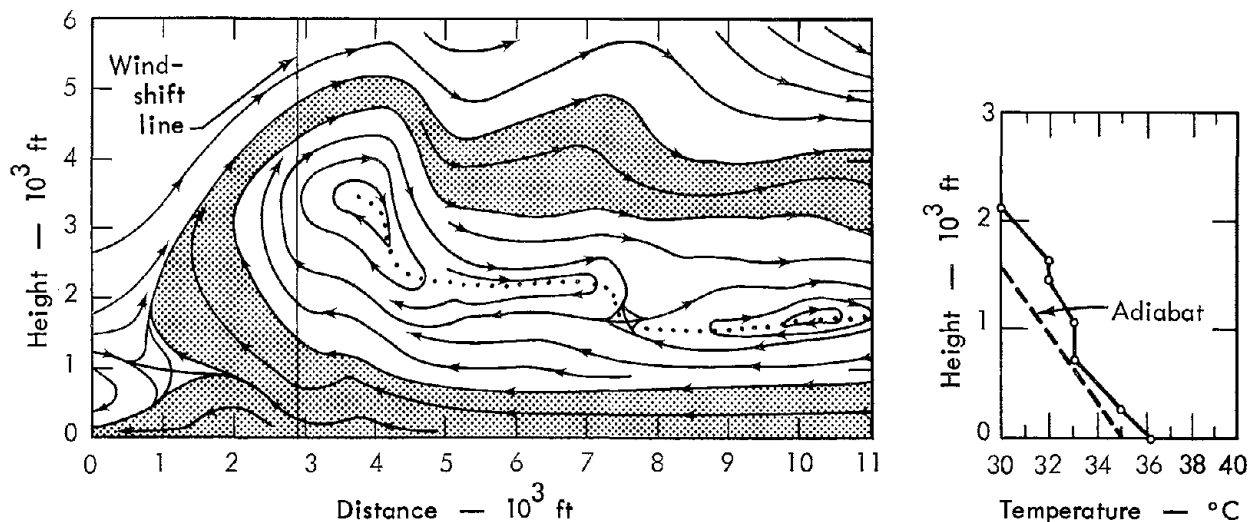


Fig. 3. Air-parcel trajectories in the San Fernando Valley relative to the wind-shift line on July 30, 1957 (taken from Ref. 59).

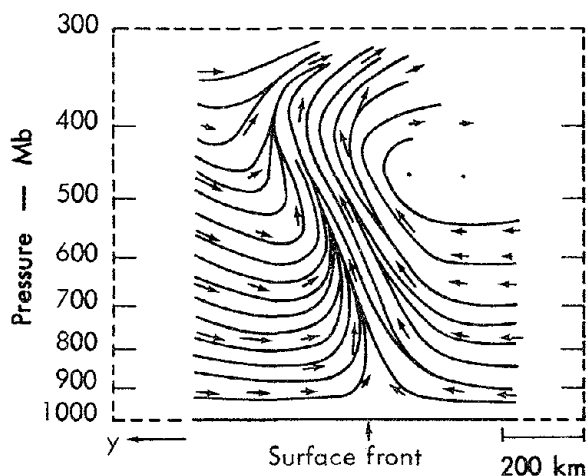


Fig. 4. Stream lines of the total transverse motion relative to the motion of the front. The arrows represent 1.5-hr particle displacements (taken from Ref. 60).

shows the 1.5-hr particle displacements Todsén calculated from the transverse flow. The results are again consistent with the scale predictions shown in Table 4 in that the maximum vertical velocity is about 12 cm/sec, whereas the horizontal component of the transverse motion is about 10 m/sec.

DISCUSSION

The types of observations and diagnostic calculations discussed above are specialized in the sense that they are not, to our knowledge, a part of the meteorological service currently provided in the U.S. The reason for this is that the meteorological observing network was primarily designed to provide the initial conditions for prediction schemes treating the synoptic scale and larger. Currently, mesoscale forecasting is a short-range prediction relying in large measure on radar, visual observation, or indirect evidence, and only in a few cases on data

from a suitable network. Since one can not prepare deterministic predictions for a scale on which there are no adequate initial descriptions, the mesoscale circulation elements are not subject to prediction. (However, as every practicing meteorologist knows, subjective prediction statements, or statistical statements, are used to relate the mesoscale to the predicted features of the synoptic scale.) Thus, one can infer that if the prediction of fallout is to be treated deterministically, then the shot-day conditions must contain relatively little energy in the mesoscale and convective systems. Winds on a scale smaller than that of the observation system can, in the first approximation, be treated or included by diffusion theory.

It should be noted that the terminal velocity of a fallout particle having a density of 2.5 g/cm^3 and a radius of 20μ is about 0.10 m/sec .⁶¹ Thus, if a fallout model based on gravitational sedimentation is to be valid, then frontal zones, with their local maxima of vertical motion, and mesoscale systems must be avoided or included in an approximate way in the calculation. It is in this regard that the scales of atmospheric motion have their impact on the fallout problem.

IMPACT ON THE FALLOUT PROBLEM

In order to maximize the predictability of the trajectories and deposition of fallout debris, shot-day criteria have evolved over the years of nuclear testing. Our understanding of criteria for shot days with planned releases are:

- That the winds in the effective transport layer be directed into a preferred "fallout" sector and that

their stability be confirmed, when technically possible, at the time of the shot by means of measurement.*

- That the debris cloud should not encounter rain or snow during the first several hours.
- That the diffusion environment for the cloud be deemed "good" for the first day or two with regard to the depth of the mixing layer and to the wind-shear theories.

If the practicing meteorologist is successful in meeting these shot-day conditions, then conditions are achieved in which sedimentation fallout models are reasonably valid. To the extent that the practicing meteorologist fails to meet these shot-day criteria, then unexpected trajectories and/or hot spots from mesoscale or convective circulations and precipitation will be somewhat more frequent. According to the late Dr. A. V. Shelton (LRL), the failures in fallout forecasting in the Pacific were often related to unknown or unexpected mesoscale circulations.

Experimental evidence is given for interactions between different scales of motion and their effect on man-made clouds of dust or other material. The first well documented case of this type to appear in the report literature⁸ was the detailed sampling of a Nerva cloud (a cloud of radioactivity produced by a propulsion reactor) some 15.5 to 21.5 hr after its creation at NRDS. The cloud

definition was accomplished by an aircraft repeatedly flying a path between Big Sur and Santa Barbara, California, using an NaI crystal to measure the concentration of radioactivity of the cloud (the spatial resolution of sampling was about 200 m). During the six hours of measurements, the Nerva cloud passed through the profile of the sampling aircraft. A horizontal plan of the isopleths of cloud radioactivity (measured as counts per second in the NaI detector and corrected for background) is produced by transporting the measured points downstream with a speed of 15 knots (see Fig. 5). This set of isopleths illustrates the "lumpiness" or the variability of the concentration within a large-diameter (about 352-km) cloud. One explanation offered for the observed lumpiness is that the radioactivity maxima were produced by mesoscale vertical circulations transporting material to or from the flight level.⁶² If random paths through the center of the cloud were selected for detailed sampling, then the existence of such structure in the cloud radioactivity distribution introduces a range of about a factor of 3 in its mean value for the sampling path.⁶³

Lidar observations of dust and steam clouds produced by high-explosive shots in saturated shale have been reported by Oblanas and Collis.⁶⁴ Figures 6 and 7 show the approximate density isopleths in horizontal plan for 3, 6, and 8.25 min after such a shot. The interior lumpiness of the cloud may be attributable to the variation of the venting of the cavity gases or to the interaction of scales of motion smaller than the dust cloud. The latter could well have been produced by radial/

* This criterion does not preclude the presence of stable orographic-scale winds contributing to transport in the vicinity of surface zero.

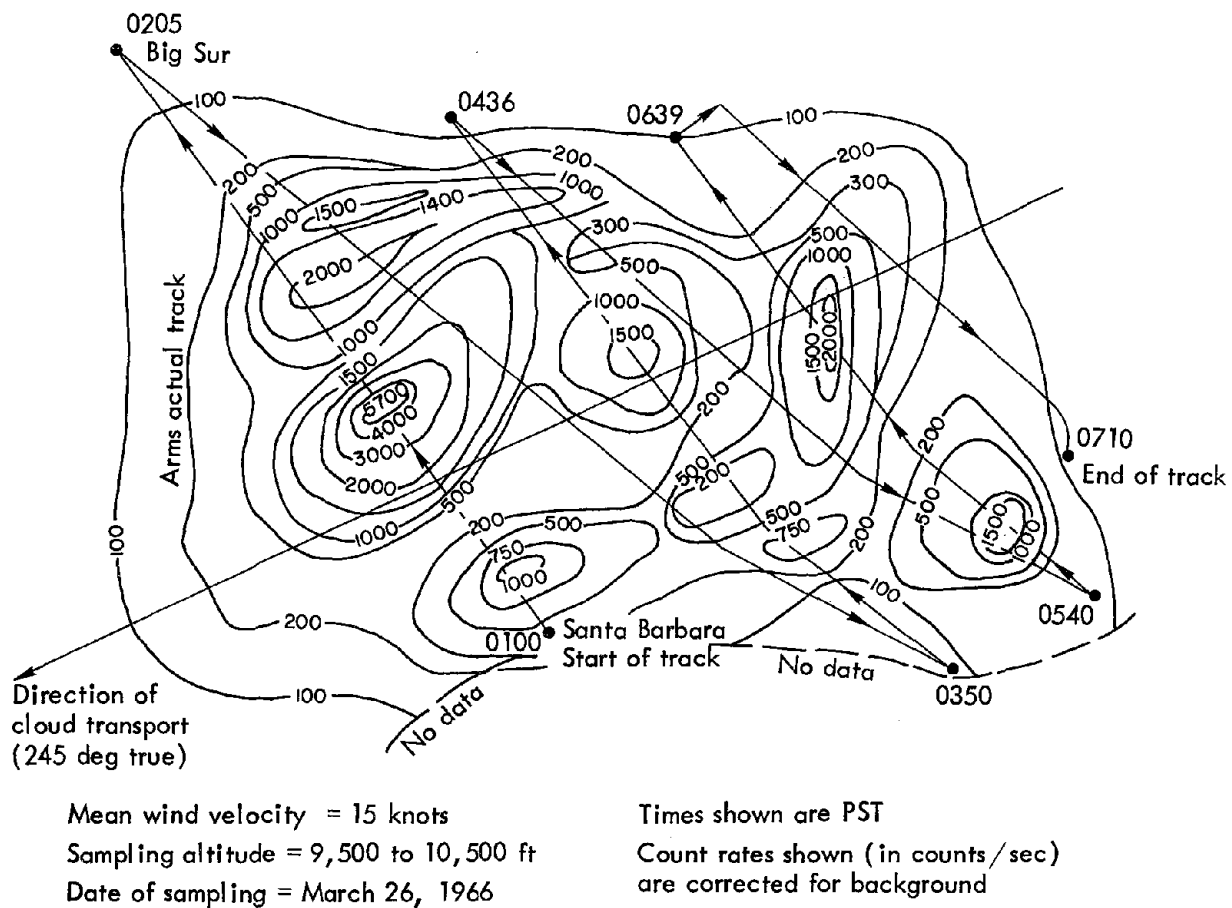


Fig. 5. NATS cloud track: isopleths of counts per second from an NaI crystal. The scale is 1:2,000,000. There has been no correction for decay during the time of data collection, and the time on this figure is for the period 15.5 to 21.5 hr after the cloud was produced.

vertical circulations within the (base-surge) dust cloud or by circulations set

up by the venting hot steam above the dust cloud.

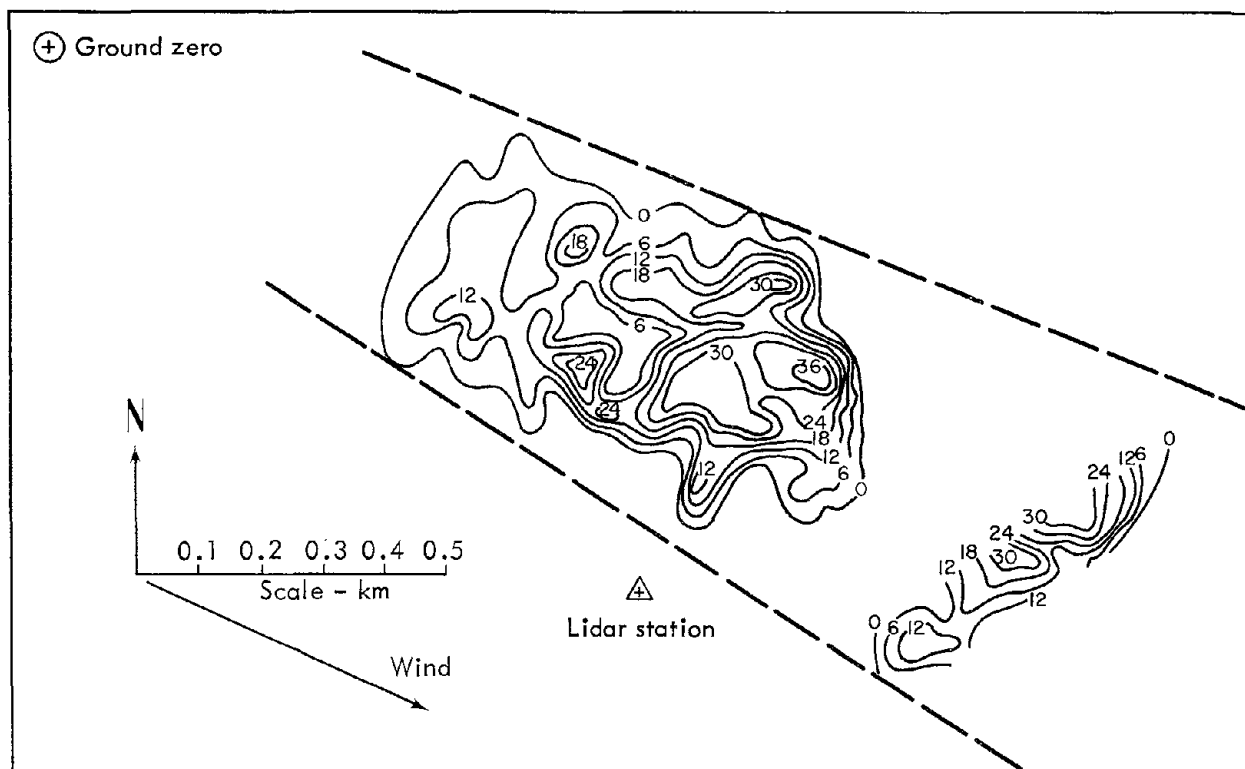


Fig. 6. Approximate density contours for a subvisible cloud inferred from relative-signal-amplitude measurements at 3 min.

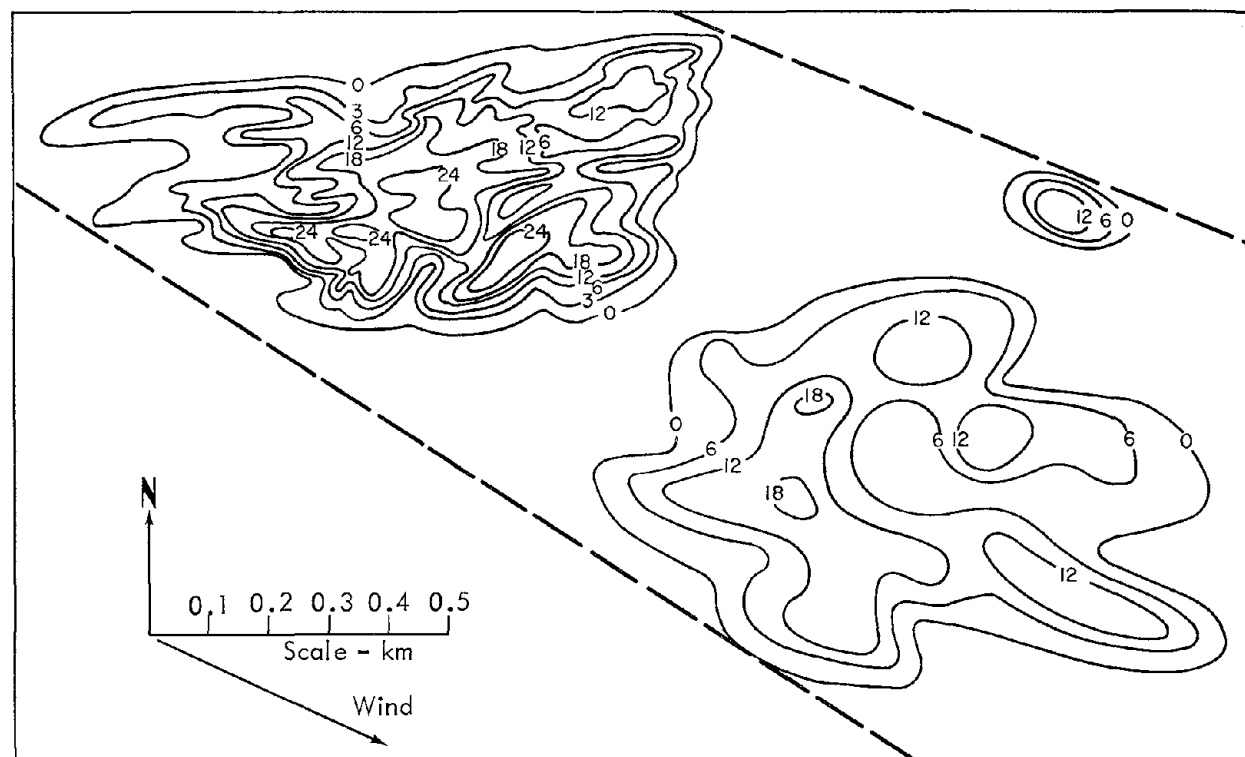


Fig. 7. Approximate density contours for a subvisible cloud inferred from relative-signal-amplitude measurements at 6 and 8.25 min.

Chapter 4:

A Cratering Fallout Model (KFOC)

Joseph B. Knox

This chapter updates a cratering fallout model presented by Knox at the 2nd AEC Fallout Conference in November 1964. The justifications of the assumptions in the model have been strengthened, where possible, and improved input parameters are noted. Verification case studies are presented for fallout prediction based on wind fields predicted by a numerical model (whose initial conditions were determined by meteorological data nine hours prior to shot time).

Calculation of the close-in fallout pattern (i.e., the gamma-exposure field) for a nuclear cratering detonation begins from initial conditions concerning the number of clouds, their geometries, their activity/particle-size distributions, and the wind field that transports and deforms the clouds during their residence in the atmosphere. Each initial cloud is subdivided into 11 clouds on the basis of

particle size, and each of the latter clouds is divided into disks. Figure 8 illustrates these points for the main cloud.

The principal physical processes simulated by the cratering fallout model are: (a) transport of the debris disks by the mean wind in the layer through which the disks fall, (b) the relative advection of the debris disks by the horizontal wind field containing both speed and directional shear, and (c) lateral eddy diffusion that expands the falling disks.

The first two processes are simulated by calculating the transport of the disk centroids by the ambient horizontal wind field during the disk's fall until the disk centroid is on the ground surface. The result of this calculation is the position vector from surface zero to the predicted ground position of each disk centroid and the time of arrival at the ground surface. Process (c) is modeled by the expression

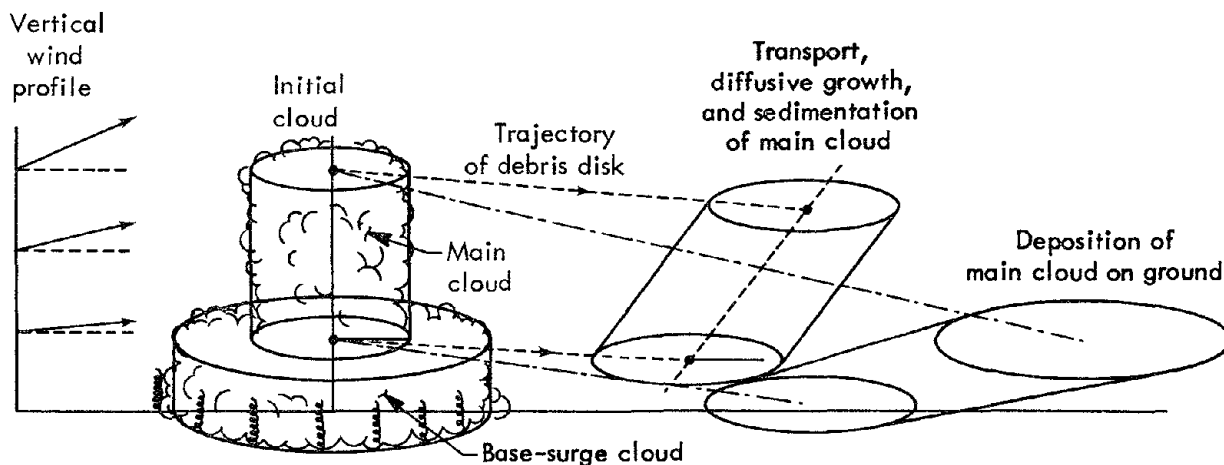


Fig. 8. Model for calculating fallout.

for the disk radius that estimates this radius at the time of arrival at the ground surface.

The gamma-exposure rate at $H + 1$ hr (for a height 3 ft above an infinite plane) is calculated using the method of Batten, Inglehart, and Rapp⁶⁵ modified by Knox² to account for the effect of normal shear (S) and lateral eddy-diffusive disk growth.

BASIS OF FALLOUT MODEL

Knowledge of the following parameters is needed to predict the gamma-exposure rate from a subsurface nuclear explosion:

- The height of the base and top and the radius of each radioactive cloud formed at the time the clouds cease their rapid rise in the atmosphere. The cloud dimensions, measured relative to surface zero, are determined from empirical relationships, given the total energy yield of the explosive (W_t) and the depth of burial (Z).
- The fission yield (W_f), the fraction of gamma-emitting radionuclides expected to appear in the fallout pattern beyond the radius of the direct ejecta (F_c), and the equivalent fission-yield conversion factor needed to simulate gamma exposure from induced activities.
- The activity/particle-size distribution in the main and base-surge clouds, and the fraction of F_c in each cloud.
- The terminal fall velocity of the particles as a function of particle size and height in the atmosphere.
- Either (a) the time and space prediction of the horizontal wind at the

level of each cloud top, along with the specification of the wind shear for the layer through which particles fall, or (b) the wind components as a function of height at shot time.

- The effect of horizontal eddy diffusion on the horizontal radii of disks of particles as they fall.

This information provides the simplest adequate basis for constructing a cratering fallout model. In addition, we assume that the radioactive species are unfractionated and that 1 kt of unfractionated ^{235}U fission products spread uniformly over one square mile corresponds to an exposure rate of 3380 R/hr 3 ft above an infinite plane at 1 hr.⁴ The terrain-shielding factor of 0.74 reduces the value of 3380 R/hr to 2500 R/hr at 1 hr.

Certain simplifications are made in the atmospheric processes for the cratering fallout model:

- The effect of synoptic-scale vertical motions on the vertical displacement of particles is small in comparison to the terminal fall velocity.
- The effect of divergence of the synoptic-scale horizontal wind on the radius of the disk of falling particles is small in comparison to horizontal eddy diffusion.
- After cloud stabilization, the effect of vertical eddy diffusion on deposition is smaller than that of horizontal eddy diffusion.
- The time interval from detonation to cloud stabilization is neglected in comparison to the time of arrival of fallout.
- The development of subsynoptic-scale wind fields is not included.

- Changes in time and space of the normal wind shear are ignored.
- The effect of nucleation and condensation of water on the size and hence the fall rate of particles is neglected.

FRACTION OF GAMMA ACTIVITY IN THE CLOSE-IN PATTERN

To calculate the fallout pattern from a subsurface detonation, the fraction of the total gamma activity produced that appears in the close-in fallout pattern (F_c) must be known. Experimental values of F_c have been reevaluated⁶⁶ for Sedan, Teapot Ess, Jangle U, Neptune, Jangle S, and Johnie Boy. These new estimates of F_c (for alluvium) are shown in Table 5.

The F_c data for shots in basalt (Sulky and Danny Boy) have been included in Table 5 for comparison only; they have not been used in constructing the F_c curve (Fig. 2). In 1963, when this F_c curve was

first derived, physical reasoning indicated that F_c data from basalt and alluvium should, ideally, not be mixed. Analysis of surface motion for cratering physics concepts⁶⁷ provided evidence in support of this contention:

- In hard, dry rock, the principal nuclear cratering mechanism is the change in momentum of the mound material produced by the outward-moving stress wave. The gas-acceleration mechanism was noted to be almost absent in all past experiments of this class. The implication tentatively held at the time was that the cavity-gas pressure is small at late times when the mound disassembles.
- In moist but unsaturated alluvium, both the gas acceleration and the "spall" mechanism were noted to be of equal importance. The implication drawn was that the cavity

Table 5. Experimental F_c data for alluvium.

Event	Yield (kt)	Depth of burial (ft)	F_c^a	Remarks	Medium	Reference
Sedan	100	635	0.18 (~0.10) ^b	8-min cloud sample unfractionated	Alluvium	Williamson ⁶⁶
Teapot Ess	1.2	67	0.41		Alluvium	Williamson ⁶⁶
Jangle U	1.2	17	0.56		Alluvium	Williamson ⁶⁶
Neptune	0.115	100	0.0032		Tuff	Williamson ⁶⁶
Jangle S	1.2	0	0.46		Alluvium	Williamson ⁶⁶
Johnie Boy	0.5	2	0.52		Alluvium	Williamson ⁶⁶
Blanca	19	835	0.0005		Tuff	Knox ³
Sulky	0.1	90	<0.001	Fractionated	Basalt (dry)	Miskel ²³
Danny Boy	0.43	109	0.04	Fractionated	Basalt (dry)	Williamson ⁶⁶

^aThese F_c values (Fig. 2) were derived by using the normalization constant (3380 R/hr per kiloton at H + 1 hr) and terrain-shielding factor (0.74) suggested by Higgins.

^bSee Ref. 3.

pressure in Sedan was significantly larger than 1 b at the time of venting.

More recent calculations (by TENSOR) of the cavity, cavity-pressure, and mound histories for Danny Boy⁶⁸ confirm these earlier conclusions. Using TENSOR output for Danny Boy at about 100 msec, the cavity pressure at the time of venting (600 msec) is estimated to be about 1 b.

Because of the large amount of machine time previously required to calculate the Sedan cratering, no TENSOR calculation of this event is as yet available. Hence, a simple cratering physics model (PUSH)⁶⁹ was used to estimate the cavity pressure and volume for Sedan at the time of venting (3.2 sec) as about 10 to 20 b and $2.7 \times 10^8 \text{ ft}^3$ respectively. The large difference in late-time cavity pressure for a nuclear explosive (at or below optimal depth of burial) in alluvium and basalt gives supportive evidence that experimentally determined values of F_c for these two media can not be compared. Physically, it is anticipated that as the late-time cavity pressure is diminished, smaller and smaller amounts of refractory radio-nuclides will appear in the initial cloud and hence in the fallout pattern. Further, as the late-time cavity pressure diminishes, less energy flows in the atmosphere at the time of venting to form the main cloud. The absence of a main cloud in the Danny Boy and Sulky Events is supportive evidence.

In order to specify the source for KFOC, the fission yield (W_f) and the equivalent fission yield (defined on p. 39) for simulation of the neutron-induced activities must be known. The source in the

stabilized clouds is $(W_f + \sum W_i)F_c$ at some reference time.

CLOUD GEOMETRIES

Figure 9 shows the top, base, and radius for the main and base-surge clouds at the time of stabilization.

Evidence suggests that the cloud geometry at stabilization time is a function of total yield, shot environment, depth of burial, and the meteorological conditions existing during cloud development.¹¹ Cloud-geometry parameters (R_b , H_b , R_m , H_m) have, for the past several years, been evaluated experimentally as functions of yield and depth of burial in alluvium and basalt. We consider now the most recent information in regard to these empirical functions for cloud dimensions.

Alluvium

For a subsurface nuclear detonation in alluvium, two clouds are formed, the main cloud and the base-surge cloud. The main cloud is formed by the thermal energy in the cavity gas venting to the atmosphere. The latest summary of cloud data for alluvium is shown in Fig. 10 through 15.⁷⁰ This summary utilizes all known cloud data from high-explosive and nuclear-explosive detonations in alluvium conducted by the AEC. Implicit in this summary is the assumption that a chemical explosive and a nuclear explosive detonated in alluvium at identical depths of burial and under similar meteorological conditions produce the same cloud geometries.

The primary mechanism for the formation of a base-surge cloud by explosives

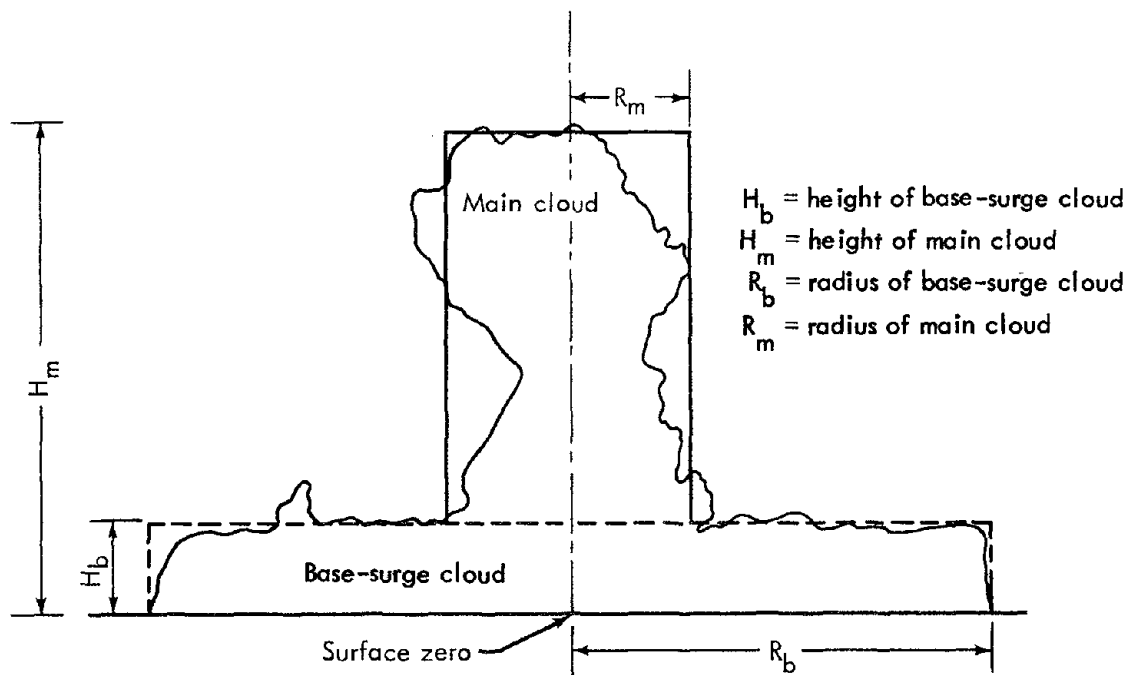


Fig. 9. Definition of cloud dimensions and symbols.

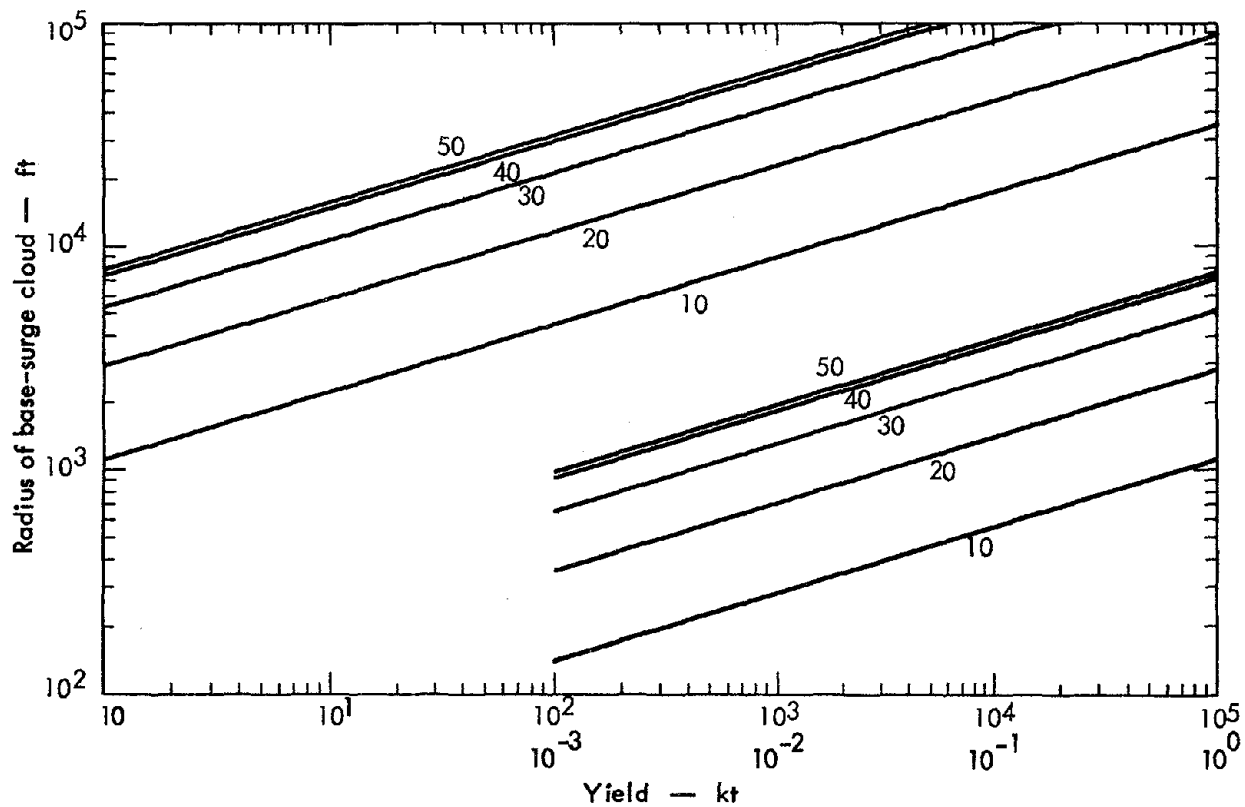


Fig. 10. Radius of base-surge cloud versus yield at scaled depths of burial of 10 to 50 ft/kt^{1/3} in alluvium.

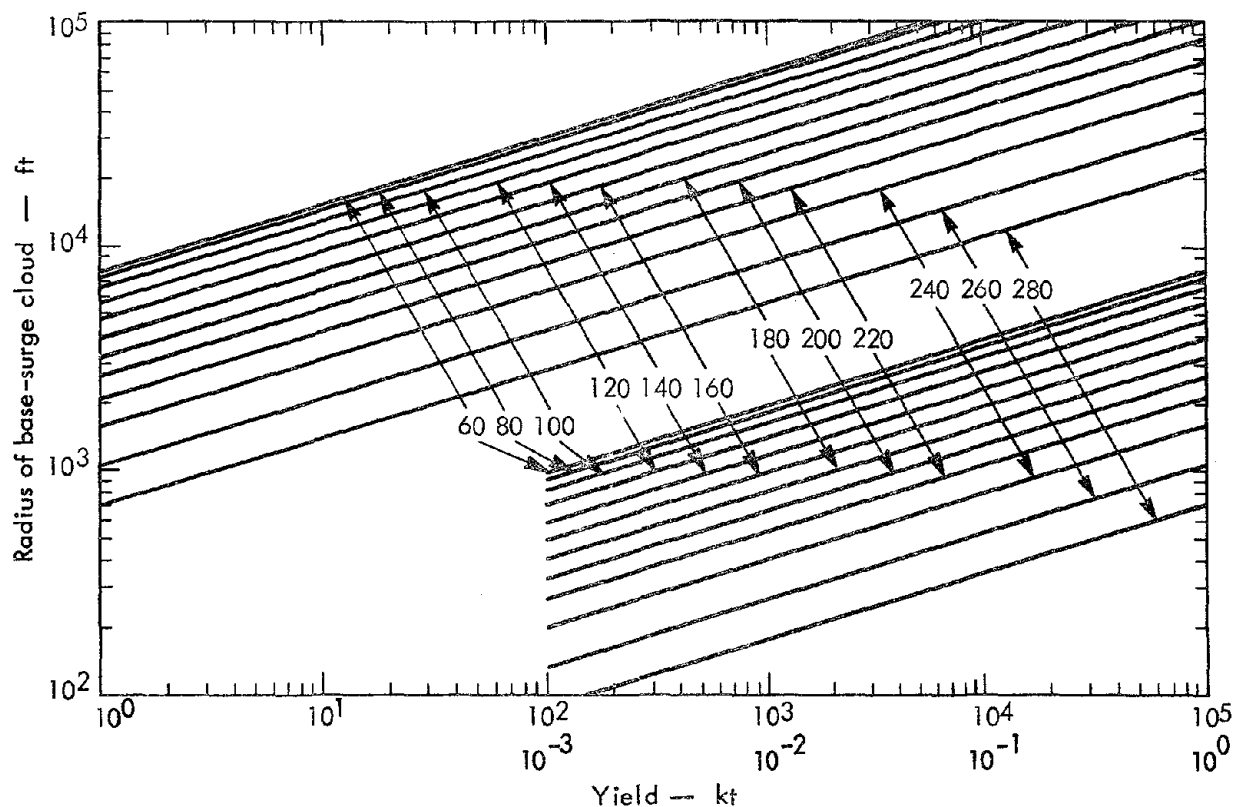


Fig. 11. Radius of base-surge cloud versus yield at scaled depths of burial of 60 to 280 $\text{ft}/\text{kt}^{1/3}$ in alluvium.

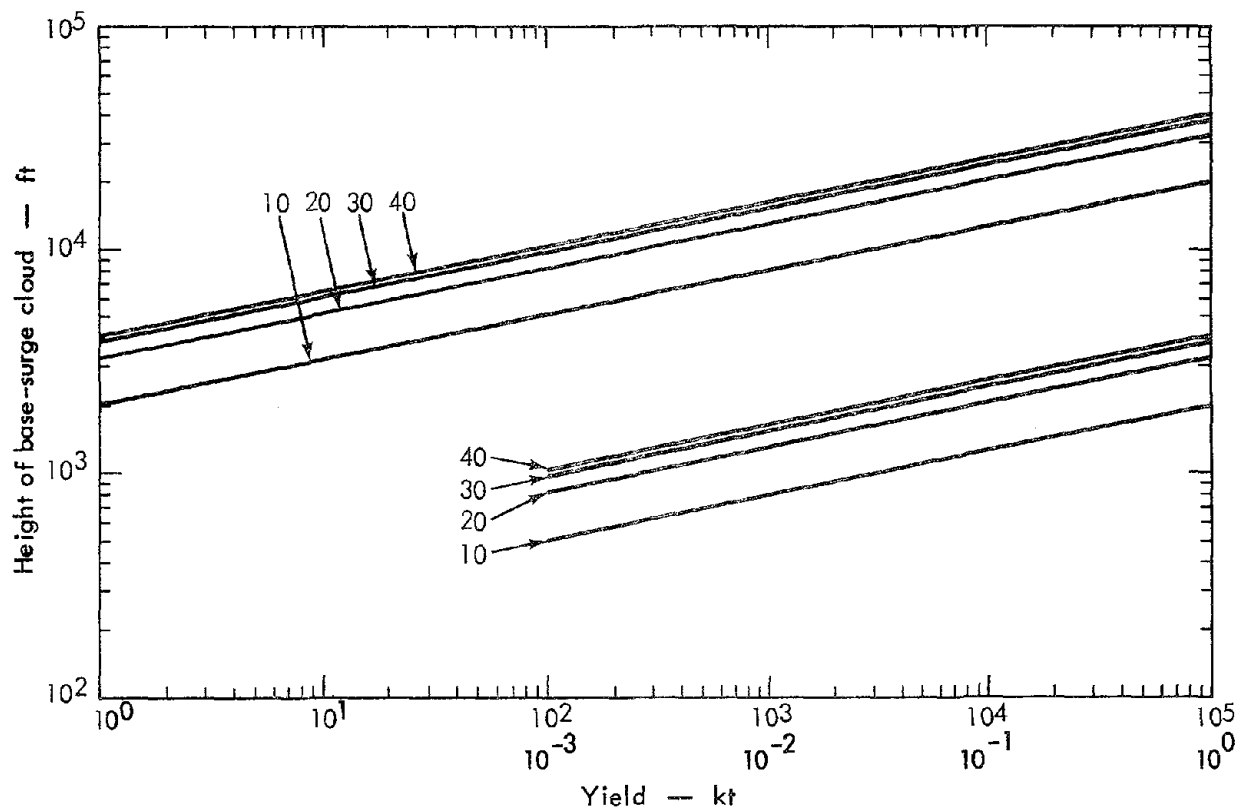


Fig. 12. Height of base-surge cloud versus yield at scaled depths of burial of 10 to 40 $\text{ft}/\text{kt}^{1/3}$ in alluvium.

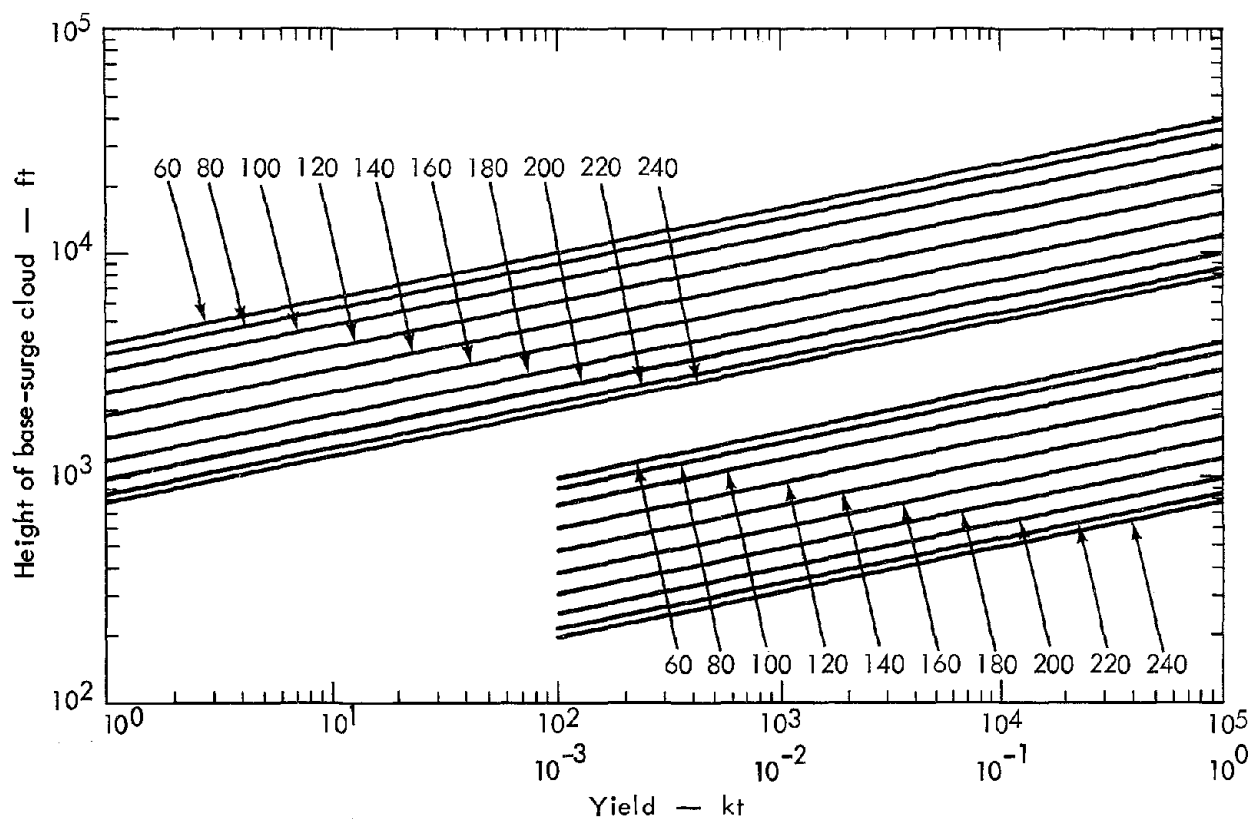


Fig. 13. Height of base-surge cloud versus yield at scaled depths of burial of 60 to 240 $\text{ft}/\text{kt}^{1/3}$ in alluvium.

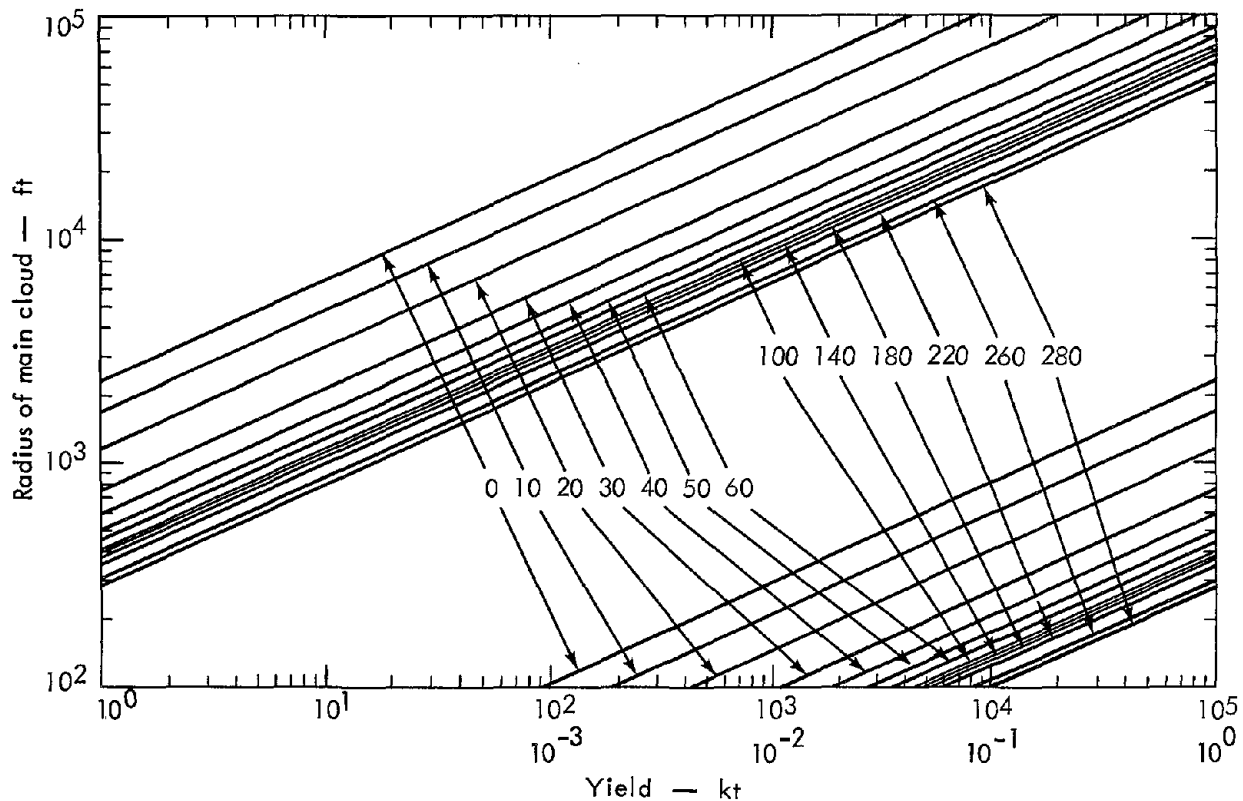


Fig. 14. Radius of main cloud versus yield at scaled depths of burial of 0 to 280 $\text{ft}/\text{kt}^{1/3}$ in alluvium.

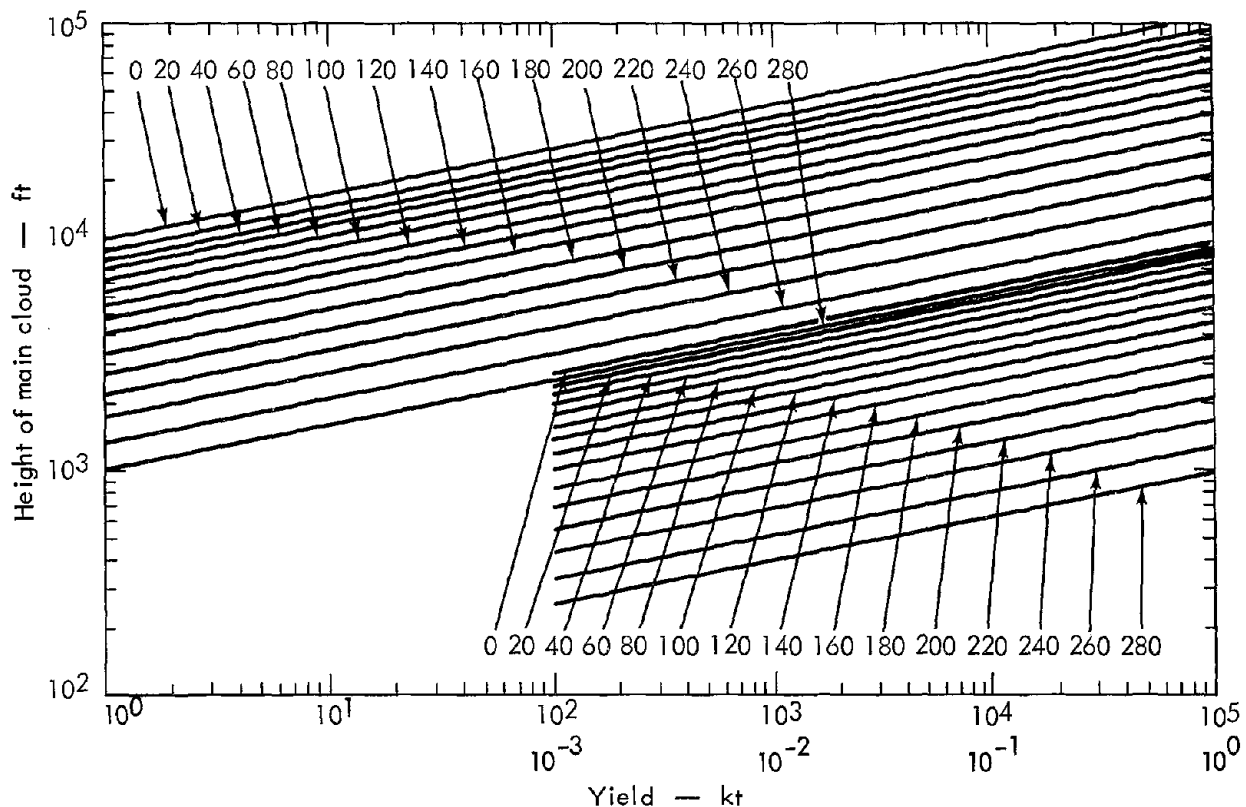


Fig. 15. Height of main cloud versus yield at scaled depths of burial of 0 to 280 ft/kt^{1/3} in alluvium.

emplaced near optimal depth is the potential energy in the suspended aerosol formed from the lofted mound material. The base-surge formation is interpreted physically as a gravity flow of a diffuse man-made aerosol, during which energy is transformed from potential energy to kinetic energy of the gravity flow. This kinetic energy is manifested as work in the displacement of air by the aerosol. The height of rise of the mound material and the particle size/mass distribution of the disassembled mound material are considered to be key factors in determining the initial available potential energy for the base surge. This physical concept of the base surge is supported by the recent calculations (Harlow, Shannon, and Welch)⁷¹ of the gravity flow of an incompressible fluid from behind a truncated

weir using the MAC code. Figure 16 shows a vertical section of the evolution

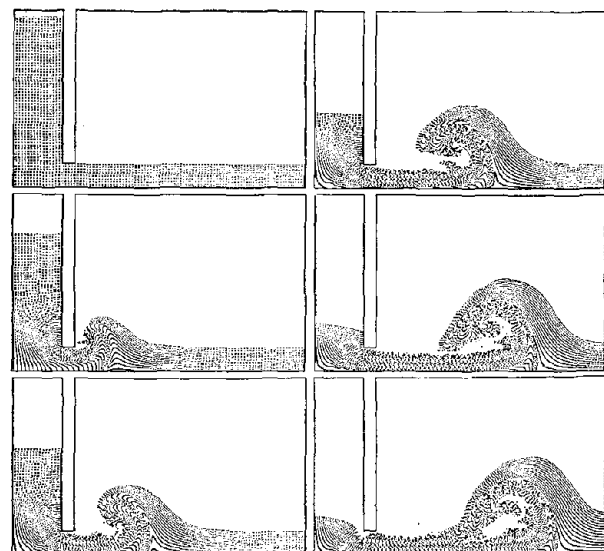


Fig. 16. Sequence of frames, produced by a computer, depicting the escape of water through a newly open sluice gate into a tranquil pond (taken from Ref. 71).

calculated by Harlow, Shannon, and Welch; the resemblance of this calculated evolution to that observed in atmospheric base-surge flows and clouds is immediately evident.

Basalt

The subsurface nuclear detonations thus far conducted in a hard, dry rock have produced only a single visible cloud—the base-surge cloud—as noted in the cases of Danny Boy and Sulky. In all published calculations to date for shots in dry media, it has been assumed that a single radioactive base-surge cloud would exist. No cloud-sampling measurements above the base surge were made to confirm the validity of this assumption in either the Danny Boy or Sulky Events. It may very well be that a nuclear shot emplaced even a small scaled distance above $140 \text{ ft/kt}^{1/3}$ may produce a main cloud. Recent calculations for the Cabriole Event suggest that this may be the case.

Experimental data on the maximum base-surge radius is summarized in Fig. 17 normalized to 1 kt. The yield dependency of the base-surge dimensions⁷² are $W_t^{0.3}$ for the radius and $W_t^{0.2}$ for the height. The difference between the scaled maximum base surge in alluvium and basalt is interpreted to be due to the difference in particle size/mass distribution in the disassembled mound. Figure 18 is a single nomogram for calculating maximum base-surge radii as a function of yield and scaled depth of burst.

Now that we have summarized the empirical knowledge of cloud dimensions from subsurface nuclear detonations, it is necessary to consider the physics of the detonation as well as cavity conditions

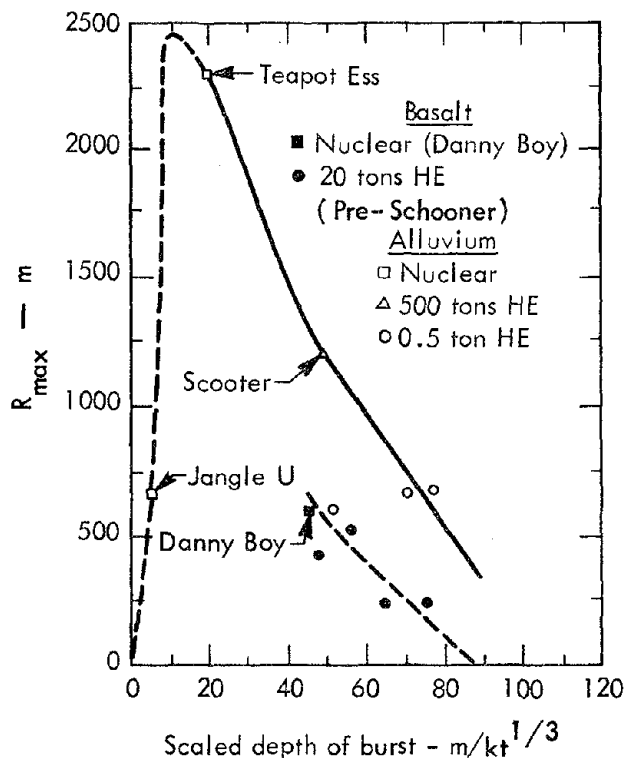


Fig. 17. Maximum crosswind radius of base surge (R_{\max}) as a function of scaled depth of burial corrected for atmospheric temperature structure.⁷³

at late times in order to evaluate the amount of energy injected into the atmosphere for the formation of the main cloud.

To do this, we must now consider venting in more detail than in Chapter 2. Venting is the process whereby the cavity gas is expanded to atmospheric pressure during and after mound disassembly. The pressure in the cavity at the time of venting is interpreted to play a major role in (a) the gas transport of the refractory materials through the mound into the atmosphere, (b) the energy coupled into the atmosphere for formation of the nuclear cloud, and (c) the gas-venting-induced air blast. Butkovich⁷⁴ has studied the effect of variable water content on the cavity-gas pressure; his results show that the water content of the

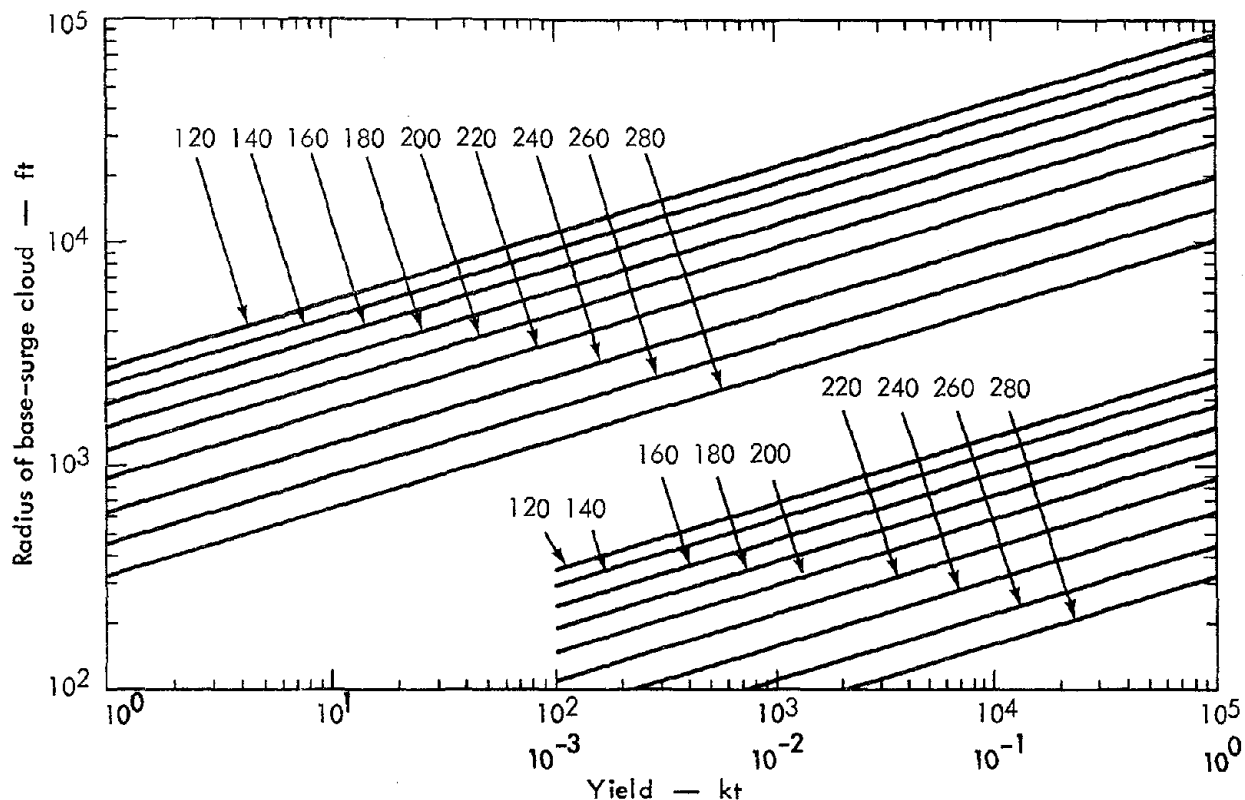


Fig. 18. Radius of base-surge cloud versus yield at scaled depths of burial of 120 to 280 $\text{ft}/\text{kt}^{1/3}$ in basalt.

nuclear shot environment is of major importance in determining the late-time cavity pressure. Table 6 summarizes and relates late-time cavity conditions to the primary cratering mechanism, the vented fraction (F_c), the observed cloud phenomenology, and supportive evidence (from air blast).

The air-blast data, the visual cloud configuration, analysis of the fallout material, and early cloud samples from the Sulky Event all support the interpretation drawn from Danny Boy and Sedan in regard to the importance of water content on late-time cavity pressure and the subsequent phenomena of venting, air blast, and cloud formation.

In the above table, evidence from air-blast overpressure was used to estimate the energy coupled into the atmosphere at the time of venting for Sedan as about 1 kt. This estimate of vented energy corresponds well with the energy required from a surface burst to give rise to the Sedan main-cloud height of 3600 m above surface zero.²⁵

A comparison of venting for Danny Boy and Sedan in Table 6 shows the importance of conditions in the cavity at t_v on the initial conditions of fallout models as to source, number of clouds, and cloud geometry. This comparison is vital to the reader's understanding of the remainder of the report and for consideration of

Table 6. A comparison of Danny Boy, Sedan, and Sulky.^a

Variable or feature	Danny Boy	Sedan	Sulky
Yield	0.42 kt	100 kt	0.1 kt
Depth of burial	Optimal	Optimal	Deeper than optimal
Medium and water content	Basalt, <1 wt%	Alluvium, 7 wt% ⁴⁹	Basalt, <1 wt%
Time of venting (t_v)	600 msec	3.2 sec ⁴⁹	Not known
Cavity pressure at t_v	1 b	10 to 20 b ⁴⁹	<1 b
Energy in cavity	Small	~10%	Small
Principal cratering mechanism	Spall ⁶⁸	Spall plus gas acceleration ⁶⁷	Spall (no crater but a mound)
Main cloud	None observed	Main cloud observed	None observed
Supportive evidence	Air-blast over-pressure from spall exceeded that from venting ⁷⁵	Air-blast over-pressure from venting exceeded that from spall ⁷⁵	Same as Danny Boy ⁷⁵
Fractionation in early air samples	High ²²	Virtually none ⁴²	Very high ²³
F_c	0.04	0.18	<0.001 of refractory species vented ²³

^aThe data in this table are a synopsis of evidence reported in many documents.

large-scale excavation projects in media with unknown water contents.

Cabriolet* Venting

As has been previously mentioned, past experience indicates that a nuclear detonation emplaced at an optimal depth of burial in a moist but unsaturated material (Sedan) produces both a main cloud and a base surge, while a nuclear detonation in a hard, dry rock (Danny Boy), also at an optimal depth of burial, produces only a base surge. For the proposed Cabriolet Event, the depth of burial is about 15 scaled feet shallower than Danny

Boy. The questionable production of a main cloud in the Cabriolet Event is legitimate, for the transition to the creation of a main cloud must occur between a zero scaled depth and that of Danny Boy. The physical argument for the production of a main cloud in Cabriolet proceeds as follows:

1. The cavity pressure and volume at 135 msec calculated using TENSOR are 48 b and 4.77×10^3 m. At 135 msec, the free surface has a speed of about 68 m/sec and is in free fall. It is estimated (Cherry)⁷⁶ that the weak subsurface recompaction wave would not reach the earth's surface, giving a surface gas acceleration. Hence, the free surface should remain in free fall,

* Cabriolet was a 2.3-kt cratering shot fired at NTS in January 1968. The shot environment was dry rhyolite, and the depth of burial was 52 m.

- although continuing to rise, from 135 msec to the time of venting.
2. The time of venting (Cabriolet) is estimated by scaling the Danny Boy venting time according to the cube root of the yield and by adjusting this value for a scaled depth of burial by multiplying by the ratio of the scaled depths. Hence, t_v (Cabriolet) is 960 msec.
 3. Since it has been argued that the free surface should be in free fall from 135 to 960 msec, we can easily calculate the configuration of the free surface at 960 msec (see Fig. 19). If the mound material at 960 msec is assumed to be a homogeneous incompressible fluid with its original density, then the average mound thickness at 960 msec is 20 m (see Fig. 19) and the corresponding cavity volume is $8.59 \times 10^5 \text{ m}^3$.
 4. Adiabatic expansion of the cavity gas from 135 to 960 msec results in a cavity pressure of 2.25 b (for $\gamma = 1.05$), which corresponds to an internal energy in the cavity at the time of venting of about 1 kt. It has

been pointed out⁷⁷ that only 65% of the 1 kt of energy is available to perform work. Our interpretation of Sedan indicates that about 10% of the energy in the cavity at the time of venting actually is coupled into the atmosphere. Hence, we estimate that for Cabriolet about 0.1 kt of energy is injected into the atmosphere to contribute to main-cloud production.

5. Thus, the cloud dimensions predicted for Cabriolet are:

Base surge: Radius = 687 m
Height = 488 m
Main cloud: Radius = 217 m*
Height = 2910 m*

In a later publication, we will compare the measured Cabriolet cloud dimensions and discuss the adequacy of the above method of predicting cloud geometries (at stabilization time) from calculated cavity conditions and a known emplacement depth. This method can only be refined when venting for nuclear detonations in arbitrary shot media is better understood. From the experimental data (Table 6), it appears that the venting mechanism controls the energy available for main-cloud formation, hence the reported (Sedan) early mixing and suppression of fractionation at stabilization time.

ACTIVITY/PARTICLE-SIZE DISTRIBUTION

For a nuclear cratering shot in alluvium (Sedan), and using the current best value of $F_c = 0.18$ (see Ref. 3 for an earlier calculation), it has been assumed

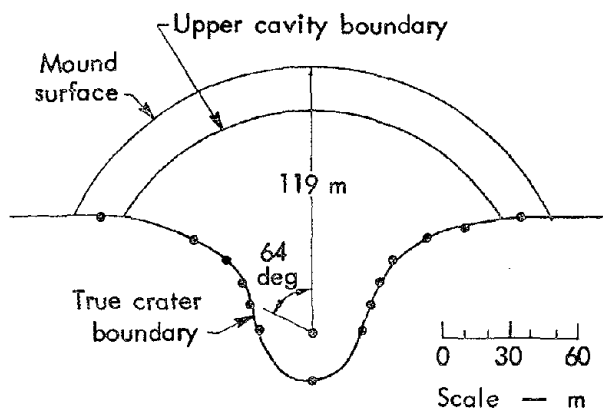


Fig. 19. Cabriolet mound and cavity configuration at vent time.

*Scaling of Sedan main cloud with the 0.25 power of the vented energy.

that 40% of the F_c gamma activity is in the main cloud and 60% is in the base surge. The $0.4 F_c$ main-cloud activity is assumed to be subdivided between two log-normal activity/particle-size distributions. The first activity/particle-size distribution contains the activity $0.4 w_m(1)F_c$ and is characterized by the mean $\ln \bar{r}_m(1)$ and the standard deviation $\sigma_m(1)$. The second activity/particle-size distribution contains the activity $0.4 w_m(2)F_c$ and is characterized by the mean $\ln \bar{r}_m(2)$ and the standard deviation $\sigma_m(2)$. The activity of the first distribution is assumed to be homogeneously mixed through the entire main cloud, while that of the second distribution is assumed to be homogeneously mixed in the lowest one-fifth of the cloud (see Fig. 20). A similar prescription of activity versus particle size is used for the base-surge cloud. At the time the cratering model was designed, there was no information on the mass loading of the debris clouds or whether the activity was

surface- or volume-distributed. By not specifying mass loading, the latter question could remain ambiguous. Several years later, the LRL particle-analysis program furnished evidence indicating that there are two activity/particle distributions in these clouds (Sedan), and that the close-in fallout is characterized by volume-distributed activity on particles 40μ in diameter and larger.¹⁵

For a nuclear cratering shot in basalt, $1.0 F_c$ is placed in the base surge. The parameters governing the activity/particle-size distributions are determined by mathematical experimentation that is discussed in later sections.

TERMINAL FALL VELOCITY OF FALLOUT PARTICLES

The fall velocities of fallout particles are modeled as the terminal fall velocities of smooth spheres having a density of 2.5 g/cm^3 in an ICAO standard atmosphere as computed by McDonald⁶¹ for

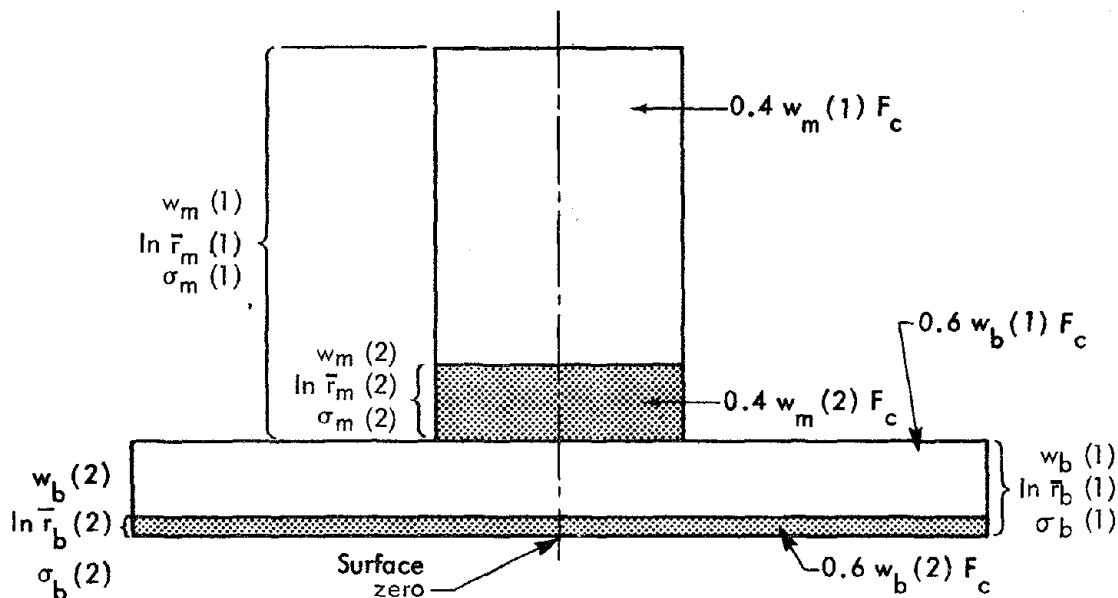


Fig. 20. An idealized cloud from a subsurface detonation, showing the spatial relations of the activity/particle-size distribution assumed in the model.

both the Stokes-law region and the aerodynamic region (where the Reynolds number exceeds 1). If in reality some fallout particles are clusters of small spheres attached to a large central particle, these complex particles are assumed to fall with the speed of an equivalent smooth spherical particle having the same mass. Experimental evidence has been obtained by Rapp and Sartor⁷⁸ to support this assumption. Thus, in the cratering fallout model the centroids of the debris disks of particles having a radius r are assumed to fall with the same terminal fall velocity as the individual fallout particle of size r .

To date, this assumption has been the basis of most fallout models, but it has not, to our knowledge, been justified. Khorguani⁷⁹ has shown that if the individual particles of uniform size in a particle system are characterized by a particle separation of 30 to 50 particle diameters, then the particle system falls with the speed of the individual particles. If, however, this condition of separation is not obtained and the particles are closer together, then the particle system can fall at a speed up to several times that of the individual particles. We will now test this condition of separation in regard to the Danny Boy Event at the time of cloud stabilization. On Danny Boy, 2×10^{11} g of material were ejected into the atmosphere. If we assume that 5% of this material goes into fallout with a mean particle radius of 40μ , then there are about 100 such particles per cubic centimeter. This corresponds to a particle separation in the homogeneous stabilized cloud of 32 particle diameters. Hence, it is justifiable to assume that

particle systems fall with the settling velocity of the individual particles after cloud-stabilization time. However, it should be noted that lack of homogeneity at times earlier than stabilization would qualitatively contribute to uneven deposition.

SPECIFICATION OF THE HORIZONTAL WIND FIELD FOR THE MODEL

The horizontal wind that transports the debris disk during its fall to the earth's surface can be specified in the cratering fallout model in the following ways.

Option 1. Idealized Wind Hodograph

If H denotes height above surface zero, then the horizontal wind (\underline{v}_h) at height H for a simple wind hodograph (see Fig. 21) is

$$\underline{v}_h(H) = \underline{v}_h(H_m) \frac{A(p)}{A(p_m)} - S(H_m - H)\underline{n},$$

where $\underline{v}_h(H_m)$ can be specified either as a steady-state wind at the cloud-top level

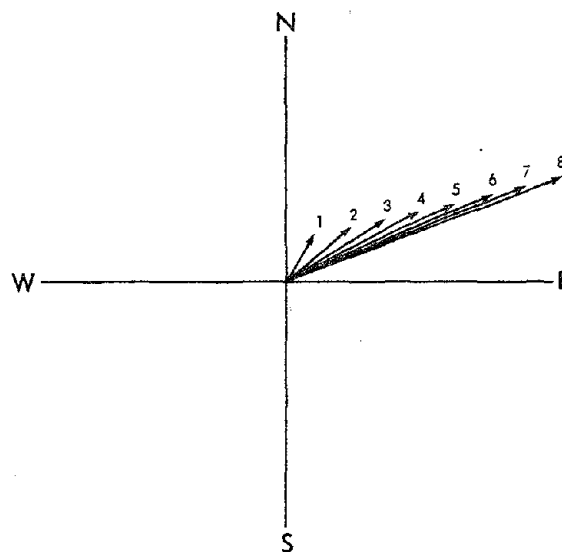


Fig. 21. Idealized wind hodograph assumed in the model for wind specification.

(H_m) or as a function of time and space in either wind-component form by means of a stream function (from a dynamic prediction model), $A(p)$ characterizes the wind-shear component tangential to the horizontal wind at cloud-top level, $A(p_m)$ is the value of $A(p)$ at the height of $y_h(H_m)$, S is the wind-shear component normal to the horizontal wind at cloud-top level, \underline{n} is the unit vector normal to $y_h(H_m)$ in a right-handed (vector) system, and p is the atmospheric pressure corresponding to H .

Option 2. Arbitrary Hodograph

In Option 2, the horizontal wind can be specified in wind-component form for as fine a vertical interval as desired.

DEBRIS-DISK RADIUS AS A FUNCTION OF TIME

The radius of a debris disk ($R_e(t)$) that is expanding by horizontal eddy diffusion during its fall is estimated by

$$R_e(t) = (R_{e,0} + 2Dt')^{1/2},$$

where t' is the distance traveled by the disk centroid divided by the mean horizontal wind speed in the layer through which the disk has settled, $R_{e,0}$ is the initial disk radius, and D is the Richardson's diffusion coefficient ($0.2 \times (\ell)^{4/3}$, where ℓ is the standard deviation of the position of the particle relative to the disk centroid). Since ℓ is only vaguely known in nuclear debris clouds, it is assumed to be equal to $R_{e,0}$ if accelerated relative diffusion is to be approximated in the fallout model.

In the summer of 1967, a logic error in KFOC was discovered in which the ℓ in the Richardson's diffusion coefficient was

in units of meters rather than centimeters. Runs with this "erroneous" diffusion coefficient, however, reproduced pattern breadth and dose quite well. Subsequently, KFOC was corrected using the scheme of Crawford⁵⁷ to calculate the time-dependent D and $R_e(t)$ of the disk at the time of arrival. Fortunately, there is a negligible difference in the results. The present method of calculating $R_e(t)$ is as follows. Initially, σ_0 is set equal to 0.7 R (in centimeters) and the dissipation (ϵ) is set equal to $(300/z)(U/5)^3$, where z is the height (in feet) of the cloud center above the ground, U is the wind speed (in meters per second), and ϵ is given in cm^2/sec^3 . Defining $z = \sigma_0^{2/3} \epsilon^{-1/3}$, and if the time down (t_d) is less than t , then

$$R_e(t) = 0.01 \left[\sigma_0^2 + 1.33(\epsilon \sigma_0)^{2/3} t^2 \right]^{1/2},$$

and if t_d is more than t , then

$$R_e(t) = 0.01 \left(2.33 \sigma_0^2 + 0.333 \epsilon t^3 \right)^{1/2}.$$

The latter two equations correspond to Eqs. (15) and (17) in Chapter 8, and the constant 0.01 converts $R_e(t)$ to meters.

CALCULATION OF EXPOSURE AND EXPOSURE RATE

The external gamma-exposure rate (\dot{X}) at a reference time (t_r) of 1 hr is calculated at the 121 predicted ground positions of the disk centroids (for 11 particle sizes and 11 initial heights) for each cloud by

$$\dot{X}_{t_r} = 2500 F_c \left(W_f + \sum W_i \right) f_d w,$$

where 2500 is the exposure rate (in roentgens per hour) at a 3-ft height at $H + 1$ hr per square mile per kiloton, assuming

uniform distribution of unfractionated ^{235}U fission products on a terrain with a shielding factor of 0.74 (if ^{239}Pu is used, the 2500 is replaced by 1920), F_c is the fraction of the gamma emitters that appears in the close-in fallout pattern, f_d is the fraction of the activity down from the given cloud for an assumed dual particle-size/activity distribution, w is the fraction of F_c in the stabilized cloud (either base surge or main cloud), W_f is the fission yield (in kilotons), and W_i is the equivalent fission yield of the induced isotope i at 1 hr.

In addition, the following equations⁷ are used to calculate exposure from fission products and neutron-induced radioactivities.

For Fission Products:

$$\text{Exposure rate} = \dot{X}(\text{fp}) = \dot{X}_r(\text{fp}) \left(\frac{t}{t_r} \right)^{-n}. \quad (1)$$

$$\begin{aligned} \text{Exposure} = X(\text{fp}) \Big|_{t_a}^{t_b} &= \frac{1}{n-1} \\ &\times \left[\dot{X}_a(\text{fp}) t_a - \dot{X}_b(\text{fp}) t_b \right]. \end{aligned} \quad (2)$$

$$X(\text{fp}) \Big|_{t_a}^{\infty} = \frac{1}{n-1} \dot{X}_a t_a \quad (3)$$

$$= \frac{1}{n-1} \dot{X}_r(\text{fp}) t_r^n t_a^{1-n}. \quad (4)$$

For $r = 1$ hr,

$$X(\text{fp}) \Big|_{t_a}^{\infty} = \frac{1}{n-1} \dot{X}_{1\text{hr}}(\text{fp}) t_a^{1-n}. \quad (5)$$

For Induced Radioactivities:

$$X(i) \Big|_{t_a}^{\infty} = X(i) \Big|_0^{\infty} e^{-\lambda_i t_a}. \quad (6)$$

For Total Exposure (from fission products and induced radioactivities):

$$X = X(\text{fp}) \Big|_{t_a}^{\infty} + \sum X(i) \Big|_{t_a}^{\infty} e^{-\lambda_i t_a} \quad (7)$$

or

$$X = \frac{1}{n-1} \dot{X}_{1\text{hr}}(\text{fp}) \left[t_a^{1-n} + \sum \frac{W_i}{W_f} e^{-\lambda_i t_a} \right], \quad (8)$$

where

$$W_i = \frac{N_i X_i^*}{n_f X_f^*},$$

N_i is the number of atoms of i produced, n_f is the number of fissions per kiloton of fission, X_i^* is the exposure due to one disintegration of isotope i per unit area from 0 hr to infinity, X_f^* is the exposure due to the disintegration of 1-hr-old fission products from one fission per unit area from 1 hr to infinity, and t_a is the time of arrival.

This treatment is based on the assumption that the same percentage of the induced activities is vented as for the fission products in the close-in pattern. This implies, of course, that fractionation effects can be ignored for a first approximation in cratering events. This assumption is supported by experimental results, as previously discussed in Chapter 2.

OUTPUT OF THE CRATERING FALLOUT MODEL

The following quantities are calculated in the model and are output* in the indicated modes:

	Print-out	CRT display
Position of surface zero.		X
Exposure rate at H + 1 hr at the predicted ground position of each disk centroid for each cloud.	X	
Predicted ground position of each disk centroid for each cloud.	X	X
Envelope containing the area affected by the fallout from each cloud.		X
Time of beginning and end of fallout deposition at each ground-position centroid for each cloud.	X	
Isopleths of the exposure rate at H + 1 hr for any specified interval of dose rate (each contributing cloud and total pattern).		X
Exposure rate at H + 1 hr as a function of distance along the hot line (each cloud and total pattern).		X

DIAGNOSTIC CALCULATION FOR SEDAN

As described earlier,² the calibration of the fallout model to the Sedan fallout pattern for an F_c of 0.18 has been done by Gibson. We have found by mathematic experimentation the input parameters that yield a reasonable calculated fallout pattern. The values of the activity/particle-size parameters corresponding to an F_c of 0.18 are:

$$\left. \begin{array}{l} w_m(1) = w_b(1) = 0.9 \\ w_m(2) = w_b(2) = 0.1 \\ \ln \bar{F}_m(1) = \ln \bar{F}_b(1) = 3.8 \\ \ln \bar{F}_m(2) = \ln \bar{F}_b(2) = 5.7 \\ \sigma_m(1) = \sigma_b(1) = 0.69 \\ \sigma_m(2) = \sigma_b(2) = 0.59 \end{array} \right\} \begin{array}{l} \text{Base surge} \\ \text{contains 60\% of} \\ F_c; \text{ main cloud} \\ \text{contains 40\% of} \\ F_c. \end{array}$$

Figure 22 shows the observed and calculated gamma-exposure rates at H + 1 hr

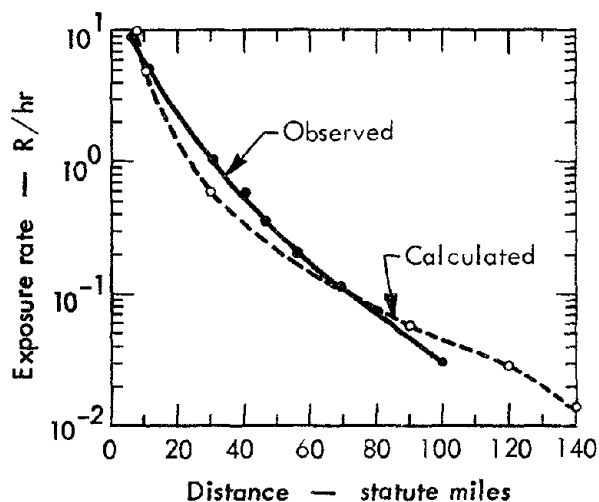


Fig. 22. Gamma-exposure rate at H + 1 hr as a function of distance along the hot line of the Sedan pattern (diagnostic calculation).

from the fission products alone as a function of distance along the hot line for the Sedan Event, using the winds at shot time. Reference to Fig. 23 indicates reasonable agreement between the observed gamma-exposure rate pattern at H + 1 hr and that calculated as to areal extent of exposure-rate isopleths; the error in the direction of the hot line reflects a change in the wind field during the period of deposition.

DIAGNOSTIC CALCULATION FOR DANNY BOY

The Danny Boy Event was a 0.42-kt nuclear cratering detonation emplaced at

* Additional outputs developed since 1964 are discussed in Chapter 6.

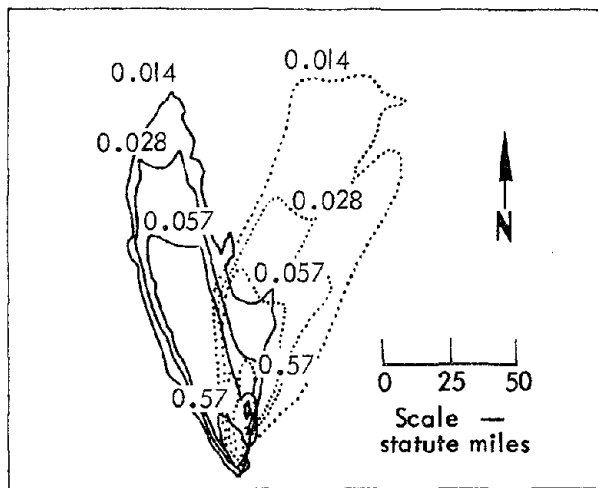


Fig. 23. Sedan gamma-exposure rates (in roentgens per hour) at H + 1 hr. The calculated rates (solid lines) were determined with shot-time winds. The observed rates (dotted lines) include an actual wind shift and are corrected for decay.

a depth of 109 ft in dry basalt. The observed gamma fallout pattern for Danny Boy has been published.⁸⁰ By mathematical experimentation with the cratering fallout model, we can adjust the activity/particle-size parameters in order to duplicate the observed Danny Boy fallout pattern. In this shot, no visible main cloud was observed.⁸⁰ Thus, in the diagnostic calculation with the cratering fallout model, we assume that 100% of the F_c gamma activity is in the base-surge cloud, and a preliminary value of $F_c = 0.05$ is assumed. The activity/particle-size parameters determined in this calculation are:

$$\begin{aligned} w_b(1) &= 0.9 \\ w_b(2) &= 0.1 \\ \ln \bar{r}_b(1) &= 3.0 \\ \ln \bar{r}_b(2) &= 5.7 \\ \sigma_b(1) &= 0.69 \\ \sigma_b(2) &= 0.59 \end{aligned}$$

Figure 24 shows the calculated exposure rate at H + 1 hr obtained with the model as well as the observed exposure rate. As was previously mentioned, the value of F_c used in the cratering fallout model was 0.05; if the value of 0.04 reported later⁸⁰ had been used, the agreement between the calculated and observed

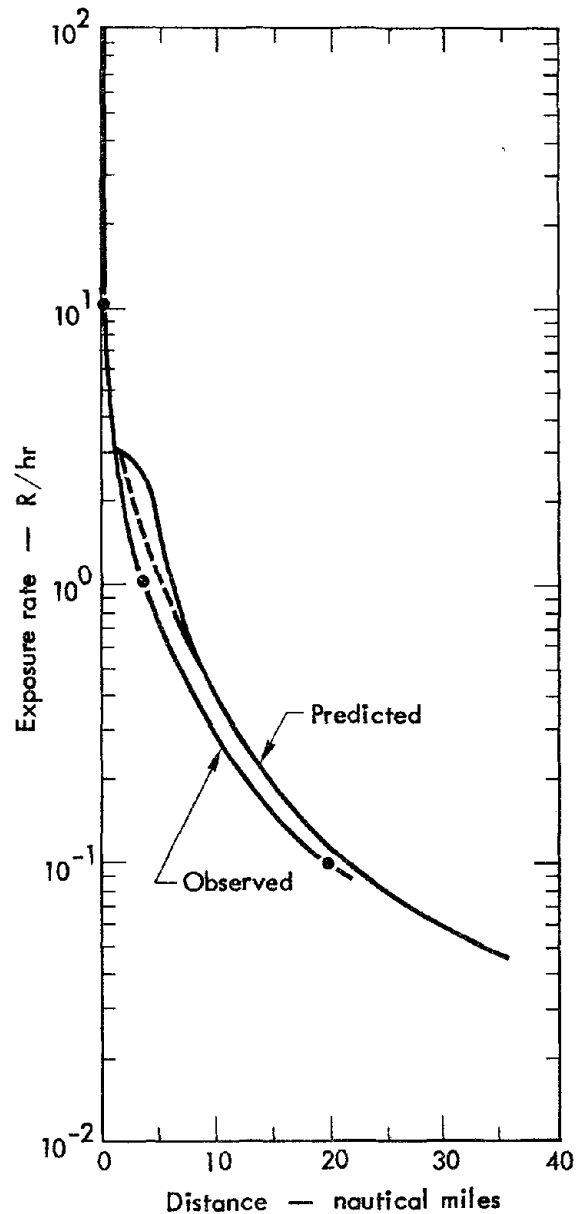


Fig. 24. Calculated and observed gamma-exposure rates at H + 1 hr as a function of distance along the hot line of the Danny Boy pattern (diagnostic calculation). $F_c = 0.04$.

exposure rates would have been better than is shown in Fig. 22.

Figure 25 shows the machine-plotted exposure-rate pattern for the Danny Boy diagnostic calculation. The calculated

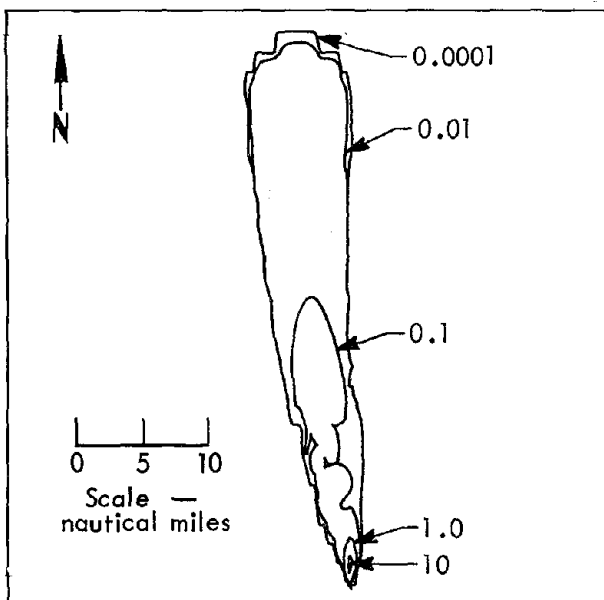


Fig. 25. Machine-plotted gamma-exposure-rate pattern (in roentgens per hour) at H + 1 hr for the Danny Boy shot (diagnostic calculation).

pattern breadth at 25 miles downwind is about 7 miles, and the breadth of the observed pattern at this distance is 5.5 miles. It should be noted that the closure of the isoexposure-rate line of 0.0001 R/hr in the plotted pattern is artificial and is the result of the logic used for the computer plotting, rather than the result of the cratering fallout model.* All isoexposure-rate lines will apparently be closed at the downwind edge of the pattern if the computed dose-rate information is insufficient for their appropriate extension downwind.

*More recent work on the pattern-plotting routine has eliminated this defect. The patterns in Chapter 6 do not have fictitious closures.

The observed gamma-exposure-rate pattern at H + 1 hr for Danny Boy is shown in Fig. 26 for comparison with the computer-plotted pattern.

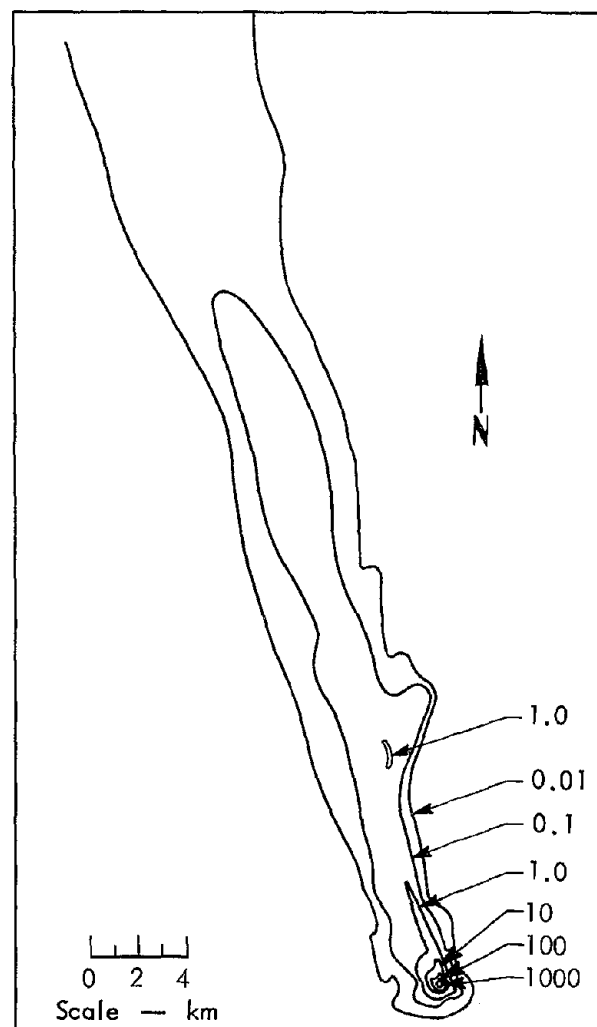


Fig. 26. Preliminary gamma-isodose-rate contours (in roentgens per hour) observed at H + 1 hr. The data are taken from Nuclear Defense Laboratory ground surveys (close-in); EG&G, Inc., aerial surveys (intermediate range); and U. S. Geological Survey aerial surveys (long-range).

INDEPENDENT TESTS OF THE MODEL

Case 1: Teapot Ess

An independent test calculation of the cratering fallout model (calibrated to

Sedan) was performed using the Teapot Ess Event (see Table 5 for description). The observed winds at shot time, the observed cloud geometry, the published fission yield of 1.2 kt, and $F_c = 0.41$ (from Fig. 8) were input to the model. Figure 27 shows the calculated and two estimated gamma-exposure rates at $H + 1$ hr as a function of distance along the hot line of the pattern. A comparison of the two curves shows that the largest error between calculation and observation is on the order of a factor of 2.0. An examination of the NTS radiosonde observation near shot time indicates that the vertical temperature distribution of the layer through which the particles were falling was slightly superadiabatic. Under such conditions, it is possible that the vertical eddy diffusion on the Teapot Ess shot day was larger than average. If enhanced vertical eddy diffusion were operative, the observed exposure rate would be

lower near ground zero and somewhat enhanced downwind in comparison with the calculated pattern.

Figure 28 shows a comparison of the calculated and observed exposure-rate patterns at $H + 1$ hr. It is clear that the transport of the debris disks as calculated from shot-time winds alone has introduced errors in positioning the fallout pattern, whereas the exposure rate versus distance along the hot line is in reasonable agreement with the estimates of the observed exposure rate. Time and spatial variations in the wind field transporting the debris disks appears to be one of the major sources of error in fallout prediction.

Case 2: Apple II²

To provide an independent test of the hydrodynamic part of fallout prediction, the Apple II tower shot (28.5 kt) was selected. It is granted that the vented

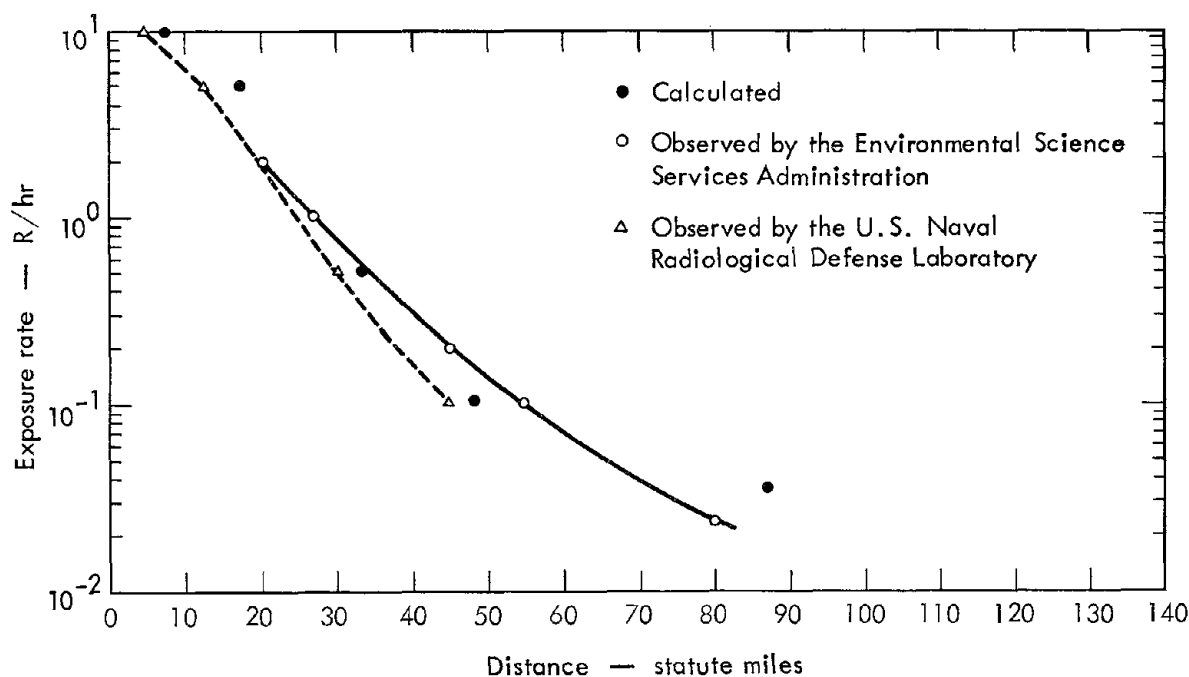


Fig. 27. Gamma-exposure rate at $H + 1$ hr as a function of distance along the hot line of the Teapot Ess pattern (diagnostic calculation).

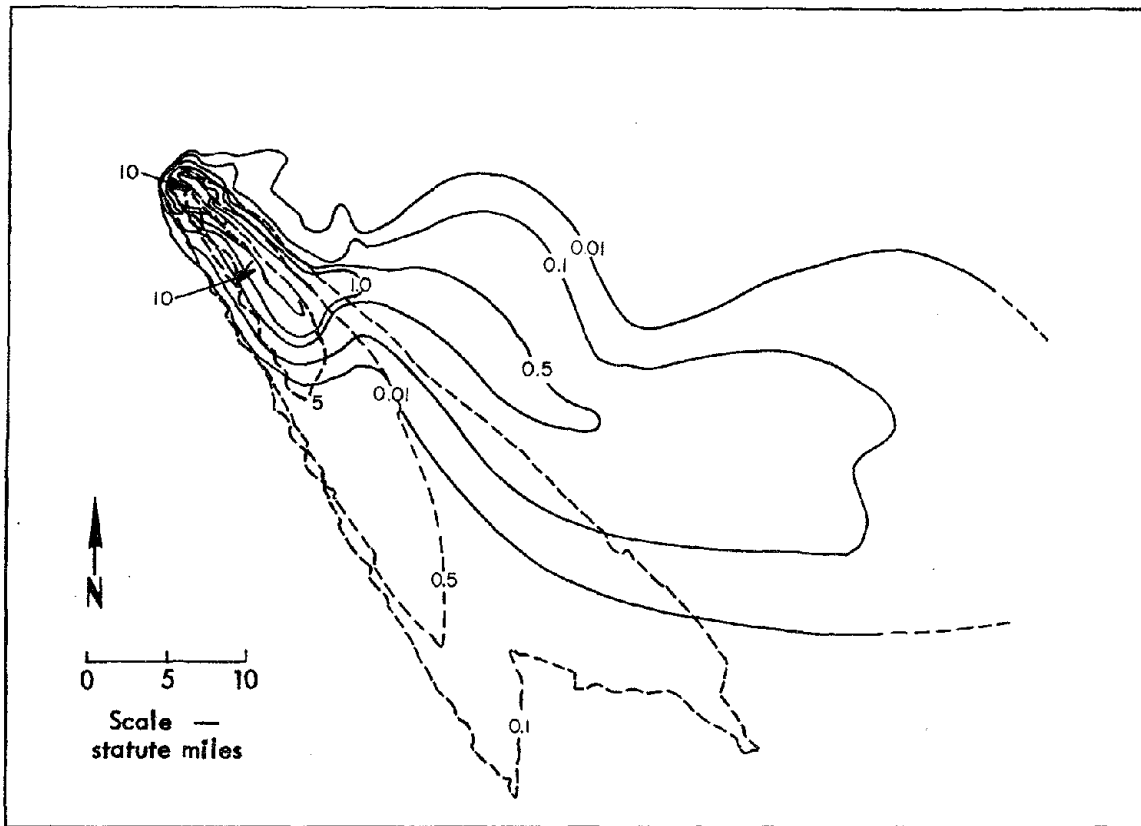


Fig. 28. Teapot Ess gamma-exposure rate (in roentgens per hour) at H + 1 hr (observed, solid line; calculated, dashed line).

fraction (F_c), the activity/particle-size distributions, and the cloud geometry are indeed different for the Apple II Event than they would be for a cratering shot or a surface burst. However, assuming the observed cloud geometry and the activity/particle-size distribution of a hypothetical surface burst, we can treat the activity from Apple II as a tracer to determine where particles of similar size would land in a space- and time-dependent transport field. Hence, the GROUNDHOG code was used to make the dynamic wind prediction for midtropospheric levels from meteorological data nine hours prior to shot time. The winds in the midtroposphere were predicted at shot time and for 15 hr thereafter. The debris disks from the hypothetical surface burst

were transported with the predicted wind field and deposited on the ground, including the effects of lateral eddy diffusion. Figures 29 and 30 show the calculated isoexposure-rate field, the calculated envelope of the radioactivity (from the assumed surface burst), and the observed envelope. With the addition of diffusion, the pattern becomes more nearly equal in width to that observed and the isoexposure-rate lines shift towards ground zero (GZ). In this calculation, the isoexposure-rate lines are incorrect in the space interval between the GZ and the ground position of the first disks deposited a few miles from the GZ. This, however, is to be expected, for the model was never intended to predict the very-close-in exposure-rate field surrounding the GZ. The shape

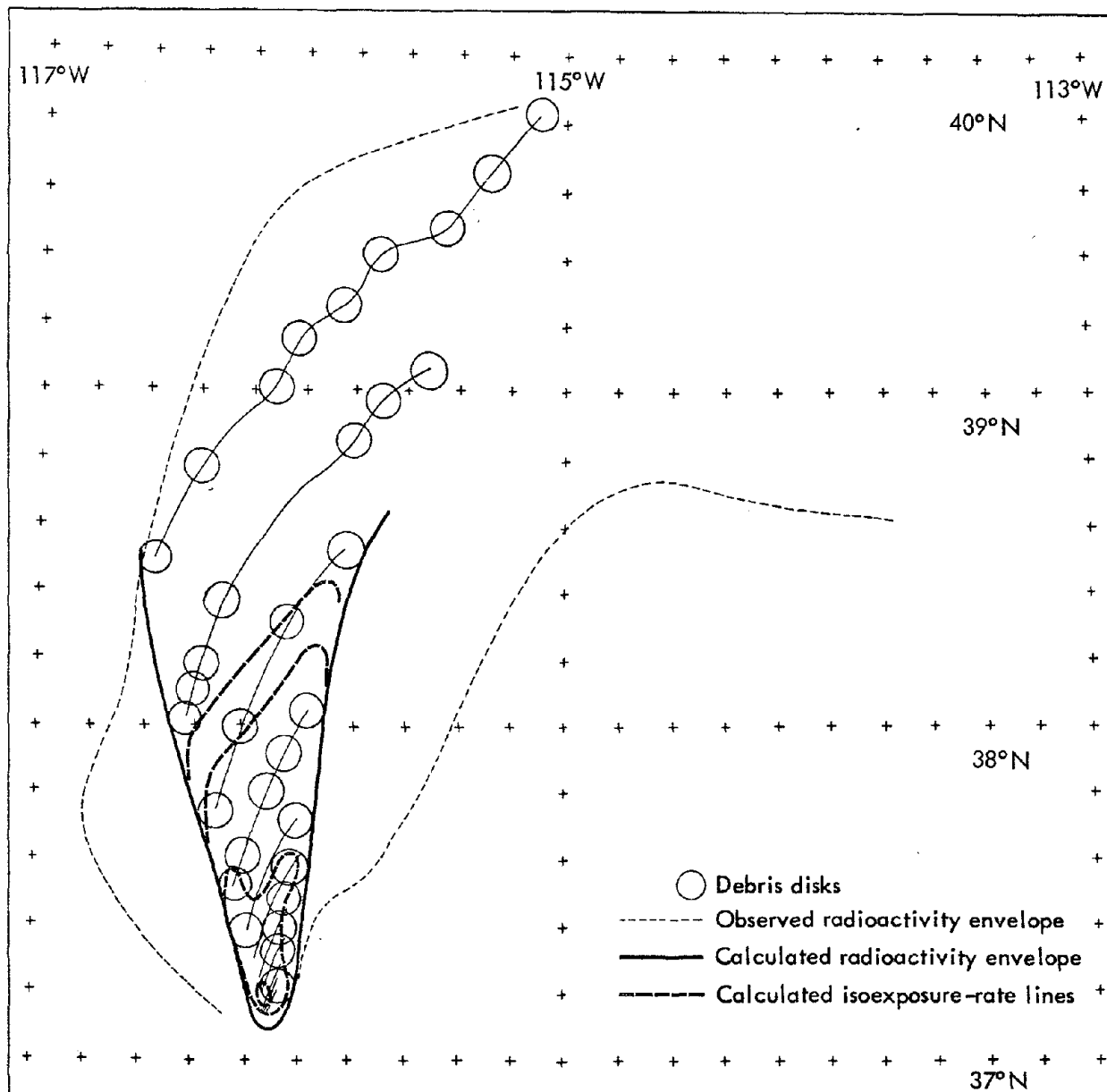


Fig. 29. Calculated exposure rate for the Apple II Event assuming a hypothetical surface burst (lateral eddy diffusion ignored).

of the calculated field, first oriented to the north and then changing towards the east, is caused by the time- and space-variable winds. The resemblance to the measured pattern is the result of a very good prediction of the tropospheric wind field. This result, along with that of the subsequent case study, was used to argue in 1962 that the modern tools

of dynamic weather prediction could be applied, with promise, to the prediction of fallout.

Case 3: Zucchini²

The purpose of displaying the Zucchini case study is similar to that for Apple II; namely, to test the capabilities of the GROUNDHOG code and to handle the

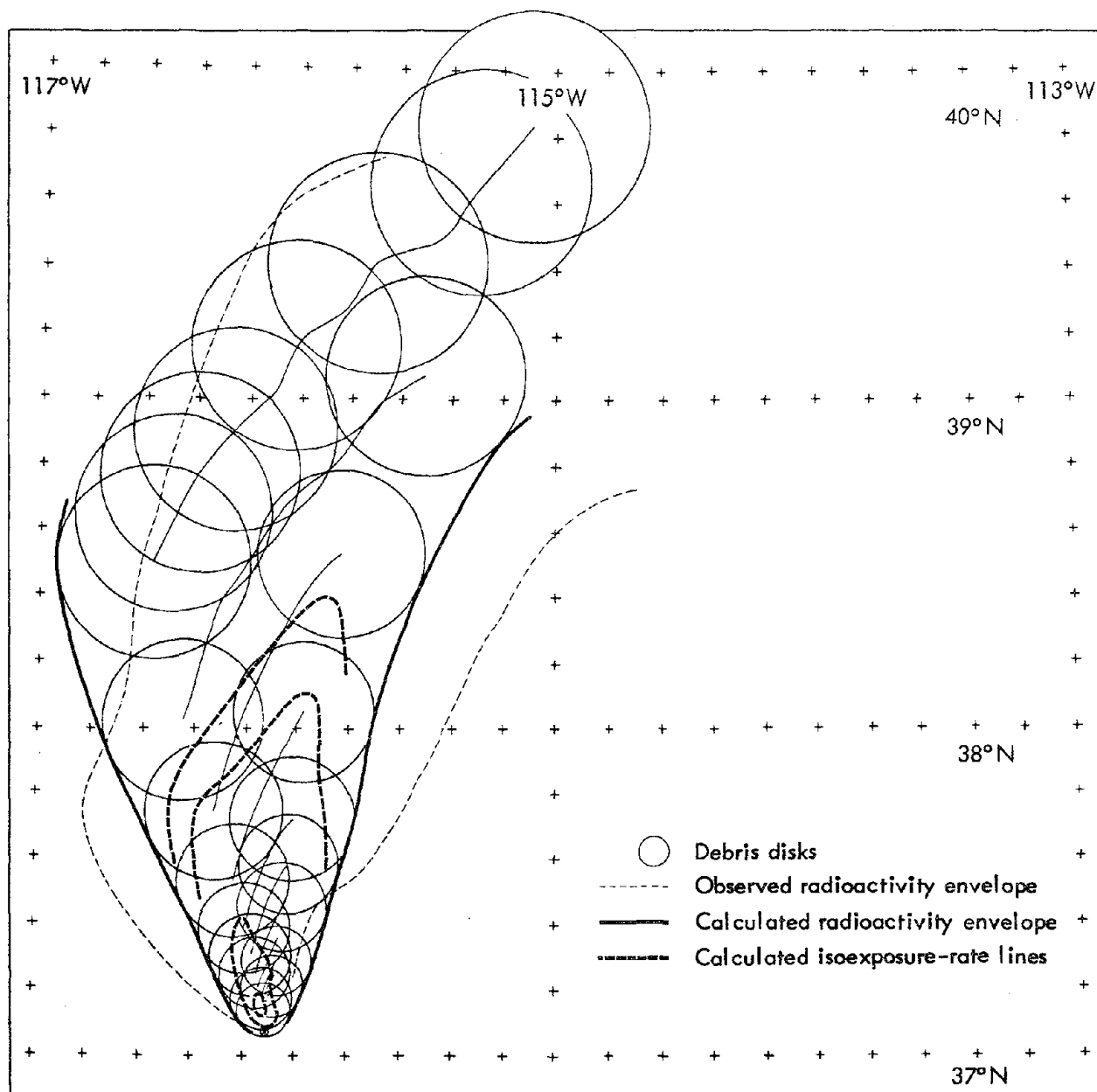


Fig. 30. Calculated exposure rate for the Apple II Event assuming a hypothetical surface burst (diffusion included).

hydrodynamic aspects of fallout prediction. The results of the calculations for Zucchini are shown in Figs. 31 and 32. The comparison of the calculated exposure-rate field to the observed field indicates that the fallout pattern is calculated better with diffusion included than with diffusion ignored. Two errors, however, are worthy of comment. First, in

the vicinity of the GZ, the transport from the northwest was not correctly characterized. In this regard, the northwesterly wind in this part of the prediction period was not forecast in this part of the pattern because of the assumption of a constant S in time. Second, the pattern width at times of several hours is incorrectly calculated. This error probably

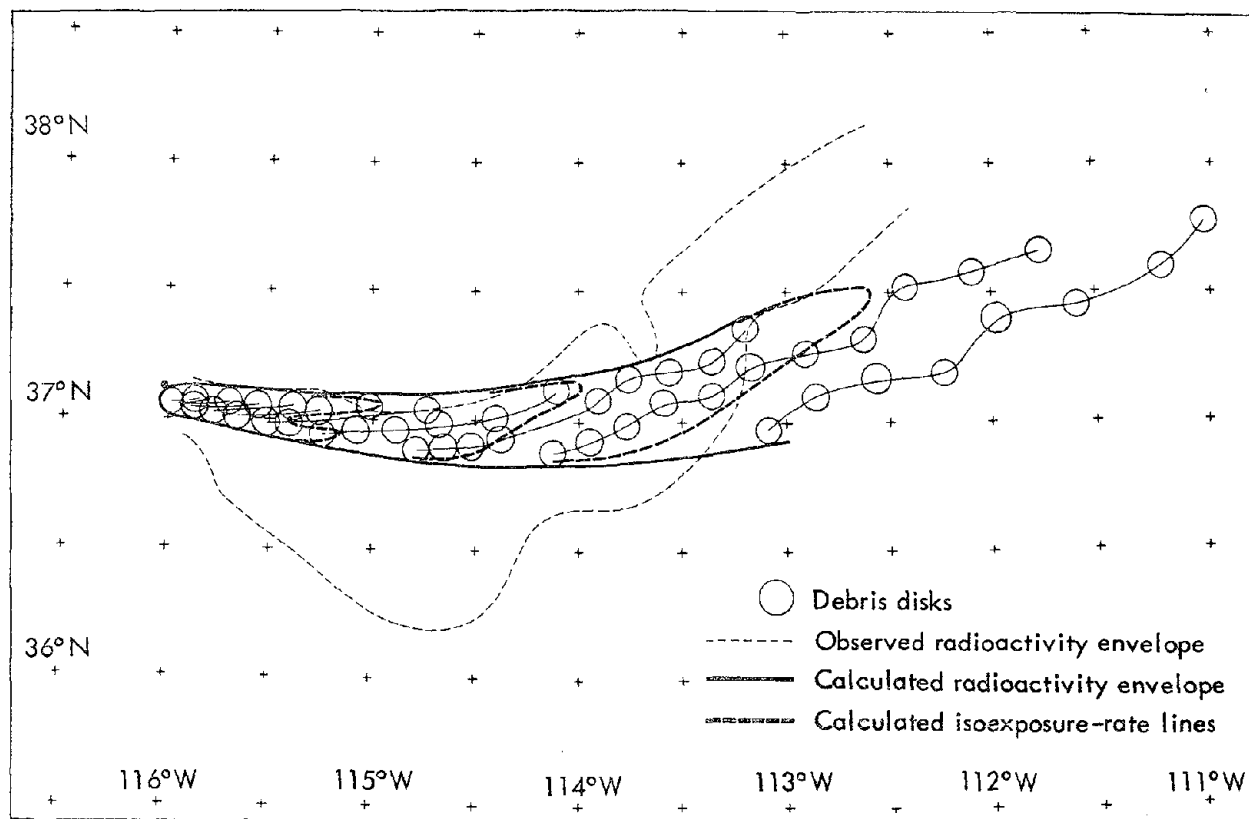


Fig. 31. Calculated exposure rate for the Zucchini Event assuming a hypothetical surface burst (lateral eddy diffusion ignored).

reflects a real deficiency in the prediction in that the debris disks are assumed to be cylindrical at all times. In reality, the synoptic-scale field of deformation could distort the disks into long ellipsoids, suppressing normal lateral growth by eddy diffusion. Judging from the actual Zucchini pattern, this probably occurred.

CONCLUDING REMARKS

In conclusion, it may be stated that the cratering fallout model gives reasonable results for the prediction of the area of

the pattern, the geometry of the exposure-rate contours, and the exposure rate versus distance along the hot line. Independent testing of the model should be extended to include more cases as data becomes available.

The maximum error in the calculated exposure rate on the hot line for the independent case is about a factor of 2. In view of the fact that the induced activities are not known to better than a factor of 2, this error in fallout modeling, reflected in the exposure rate, appears to be acceptable.

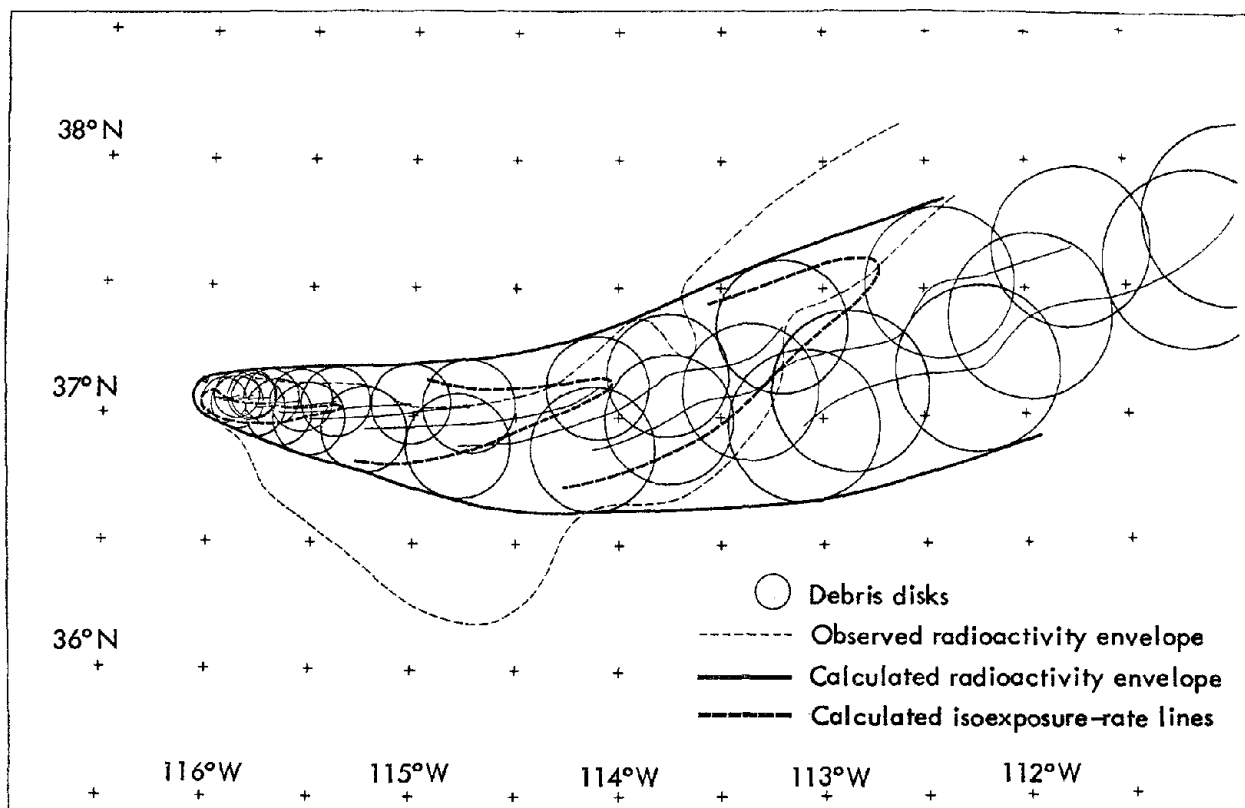


Fig. 32. Calculated exposure rate for the Zucchini Event assuming a hypothetical surface burst (diffusion included).

Chapter 5: Fallout from Row-Charge Events – General Discussion

Joseph B. Knox

In regard to fallout from nuclear row-charge detonations, it is possible to identify several key questions:

- What fraction of the gamma radioactivity appears in the close-in fallout pattern?
- What are the cloud geometries of the base-surge and main clouds at the time of stabilization?
- What effect does increasing water content in the shot medium have on cloud geometries?
- How sensitive is the close-in fallout pattern to the orientation of the channel with respect to the wind effective for atmospheric transport?
- What F_c occurs for row-charge detonations connecting to another row-charge crater?

DISCUSSION

F_c for Row-Charge Events

In the absence of F_c information for nuclear row charges, Graves, Wray, and Pierce⁸¹ performed chemical single- and row-charge detonations in which the fraction of a ¹⁴⁰La tracer in the close-in fallout was measured. The experimental evidence reported can be interpreted to imply that the F_c for a row-charge event could be about twice that from single-charge events.³ The F_c from row charge events is not now well defined and indeed will not be defined until further experience is obtained.

Cloud Geometries for Row Charges

Base Surge

Empirical methods for predicting the crosswind radius and the height of the base surge originating from HE row-charge events have been discussed by Knox and Rohrer.¹¹ It was shown that for five equal charges, equally spaced and emplaced at the same depth beneath flat terrain, the resulting base-surge cloud had about the same radius as the base-surge cloud that would be formed from a single shot with the same total yield at the same scaled depth. The base-surge height for the five-charge event is well approximated by scaling the height of the base-surge cloud for a single-charge event by the 0.2 power of the total yield of the detonation.

Main Cloud (1)

A study of time-lapse photography of the main clouds forming from multiple HE detonations suggests that the following is reasonable. The individual main clouds should be treated separately; their radius and height may be taken from the curves given by Day (Chapter 4). Hence, for a row charge of five nuclear explosives, there would be one base-surge cloud and five individual main clouds at the time of stabilization.

Main Cloud (2)

In preparing calculated fallout patterns for large projects (like the Panama Canal),

the activity in the individual main clouds is assumed to be all in the main cloud produced by the largest charge. This simplification significantly reduces the magnitude of the calculation and results in initial geometries suitable for KFOC. The assumption of Sedan venting and cloud geometry leads to the cloud-dimension-versus-yield relationships shown in Fig. 33.⁷⁰

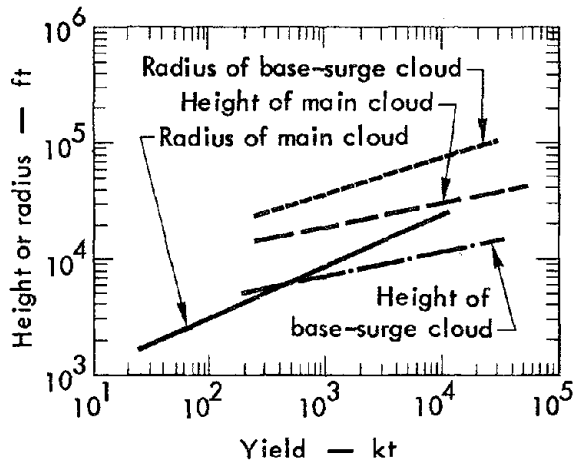


Fig. 33. Cloud dimensions for row charges composed of five individual nuclear excavation explosives.

Effect of Increasing Water-Vapor Content in the Shot Environment

The effect of increasing water content within the volume of vaporized rock is to increase the pressure in the cavity at the time of venting.⁴⁷ Because of this increased cavity pressure, it is physically reasonable to expect, in both single- and row-charge events, that:

- The column of suspended aerosol driving the base surge would be larger and hence that the "stabilized" base surge would be larger.⁸²
- The energy vented into the atmosphere may well be larger and hence

that the main cloud dimensions would increase.

- The vented fraction of the refractory radionuclides would increase.

Any future nuclear row-charge experiment should be so designed as to obtain relevant data on the above effects.

If the mound material is saturated, this may result in a modification of the potential energy in the aerosol that is associated with the base-surge phenomena. It is possible that the analysis and interpretation of data from the Pre-Gondola series will contribute information on this effect.

The experience of the Naval Ordnance Laboratory on base-surge experiments (Young)⁸² is interesting in this regard. Young reports as follows: "Day to day variations in the moisture content [of the mound materials in the small 100-lb experiments] will also occur during rainy periods. This variation in soil properties is probably responsible in part for the lack of symmetry of the dust clouds produced by most of the explosions studied. In many cases radial throwout and base surge development is pronounced on one side of the charge and relatively minor on the other." Without a comparison of the throwout or mass deposition with the measured preshot soil-moisture distribution, Young's experience is not conclusive.

Adequate information on the above is not available at this time. Hence, for feasibility studies there is no alternative but to estimate the base-surge radii of cratering shots in saturated or moist media by scaling the Sedan base-surge radius.

Orientation

To examine the effect of the orientation of a row charge to the direction of wind on the fallout pattern, we performed the following pair of calculations. The exposure-rate patterns at $H + 1$ hr were computed for 10 Danny Boy detonations on an east-west line with charge centers separated by 33.5 m, and 10 Danny Boy detonations on a north-south line with charge centers separated by 33.5 m (see Figs. 34 and 35).

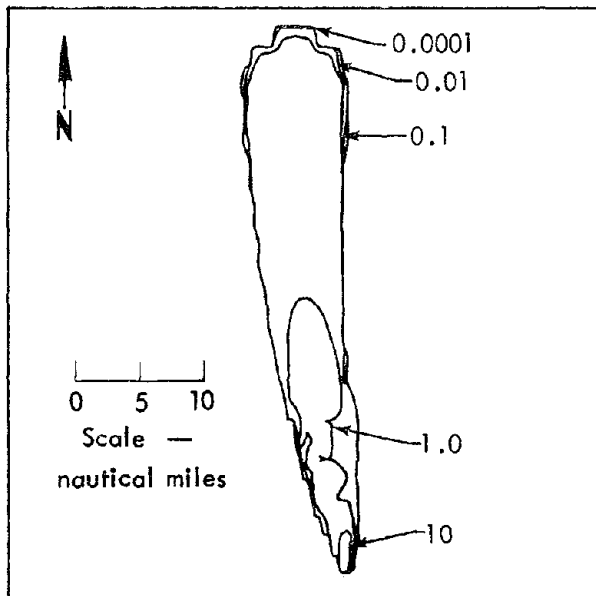


Fig. 34. The $H + 1$ hr gamma-exposure-rate pattern computed for 10 Danny Boy detonations on an east-west line with charge centers separated by 33.5 m. Values are in roentgens per hour.

For these calculations, we assume $F_C = 0.05$ for each detonation. The individual clouds are assumed to be the same as those of Danny Boy, and the input wind for each problem is assumed to be the shot-time wind for Danny Boy. These two row-charge fallout patterns, although de-

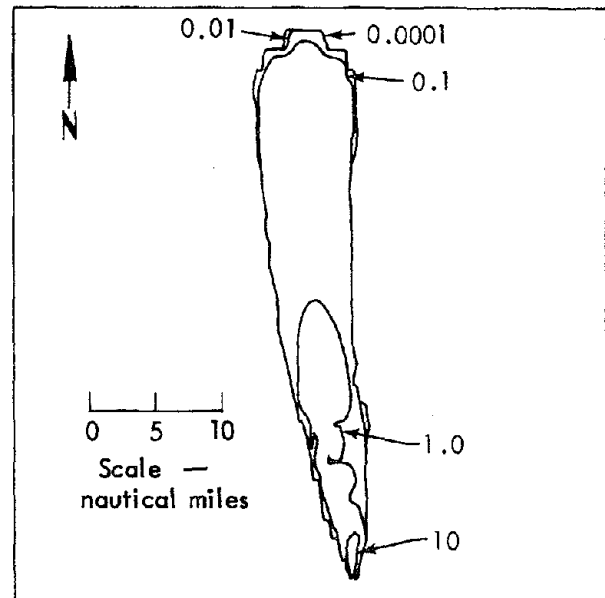


Fig. 35. The $H + 1$ hr gamma-exposure-rate pattern computed for 10 Danny Boy detonations on a north-south line with charge centers separated by 33.5 m. Values are in roentgens per hour.

tectably different, appear to be similar. The pattern widths differ by 10 times the charge spacing, which is exactly what one would expect. The results suggest that the exposure rate as a function of distance from a row-charge event involving only 10 charges is not sensitive to the orientation of the wind relative to the alignment of the charges.

F_C from a Connecting Row-Charge Detonation

It is obvious that in regard to F_C from a connecting row-charge detonation, we have no knowledge. This problem is sufficiently complex so that the only hope of obtaining relevant data is by means of HE or nuclear experiments in appropriate shot environments.

Chapter 6: Fallout from Row-Charge Events — Transisthmian Canal

Joseph B. Knox and Thomas A. Gibson Jr.

In the next few years, the safety questions and feasibility of the Atlantic-Pacific Transisthmian Canal will be under study by several technical working groups, including one on radioactivity. The capabilities of KFOC, some preliminary calculational results, the sensitivity of exposure patterns to parameter variations, and strategic questions herein discussed are not presented to pre-empt the technical working groups in any way, but rather to provide a synopsis of current capabilities with illustrations. The options employed in our examples of Transisthmian fallout patterns are:

- The horizontal wind-field input is in u,v components as a function of height from climatological wind data selected to give fallout only in the sector between 180 and 240 deg from true north.
- The code can accommodate up to 50 debris clouds of differing geometries, up to 5 significant induced radionuclides, and up to 200 climatological wind conditions. The exposure rate at H + 1 hr and the exposure calculated from the time of arrival to infinity for each cloud are stored in memory, and the patterns from the 50 clouds are superimposed to give the total pattern for each input set of winds.
- The resulting patterns for each wind condition (50 clouds) can be held in memory for analysis and

preparation of probability distributions for exposure.

- On selected (one-detonation, two-cloud) problems, we assume that the wind field in the lowest 1000 m is not known. When a debris disk is falling through this layer of unknown (or uncertain) winds, a random selection of wind direction (0 to 360 deg) and wind speed (0 to 15 knots) is made. For any given problem, the randomization is made once and the wind so selected is held constant in time and space during the calculations. Physically, this corresponds to a fixed error in the "transporting" wind induced by ignorance and/or uncertainty.

Figure 36 is a schematic outline of the input information and the output available from KFOC and the plotting routine. The code capacity for handling up to 200 different wind situations for up to 25 detonations resulting in two debris clouds makes KFOC a valuable tool for calculating exposure patterns.

DESCRIPTION OF PATTERNS PRESENTED

On pp. 58 through 70, we present four sets of problems showing computed fallout (total external gamma exposure) patterns for Transisthmian Canal Route 17A. (Figure 37 shows a map of the area for general orientation.)

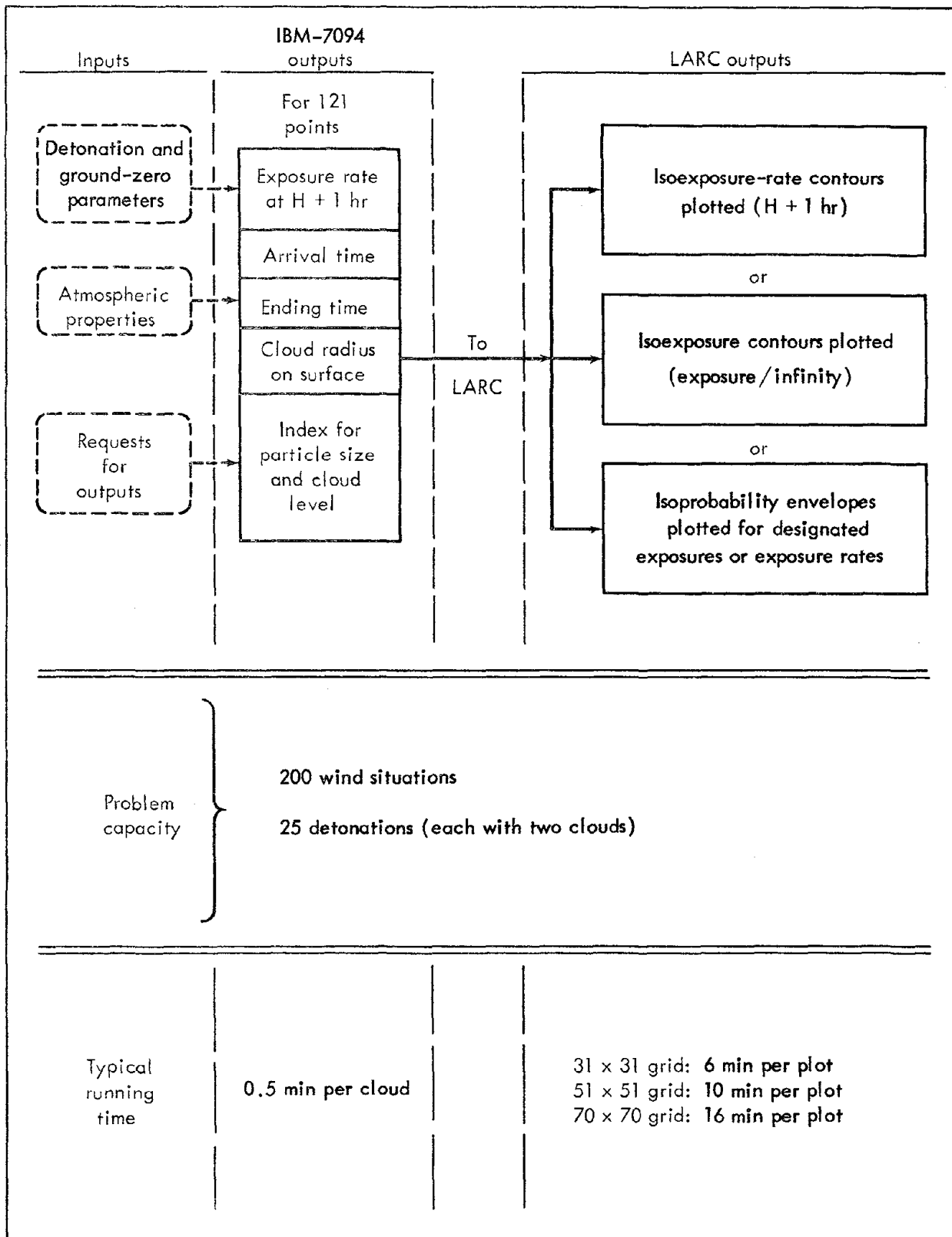


Fig. 36. Flow chart for the Knox fallout code (KFOC) and the treatment of its output.

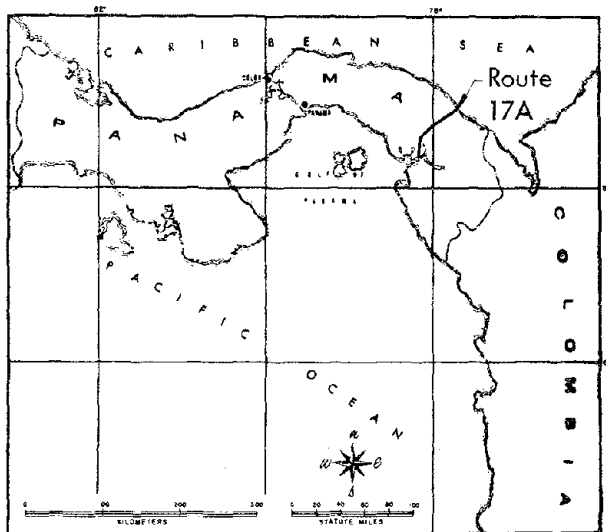


Fig. 37. Location of the Transisthmian Canal Route 17A.

Set 1 (problems 1 through 5) considers a nuclear detonation (five devices) with a total yield of 18 Mt (1964 alignment) and a variation of input parameters in regard to base-surge radius and height, height of main cloud, variation of wind speed, and randomization of low-level winds. The radioactive source* is kept constant in problems 1 through 5. (Each problem is preceded by a description showing the characteristics of the detonation and the input parameters.)

Set 2 (problems 6 and 7) shows the fallout pattern that is expected for the smallest detonation selected from the 1966 alignment of the "first pass—Route 17A" provided by the Nuclear Cratering Group, Corps of Engineers. The total yield of the source for the patterns shown is 1 Mt;

*In February 1967, the AEC declassified information⁸³ which indicates that the amount of radioactivity released to the atmosphere by future cratering applications is expected to be as low as the radioactivity source terms quoted in the following section. This reference also lists a number of the individual radionuclides that are expected to be present.

appearing as fallout are the fission products from 100 tons of fission and induced activities equivalent to 280 tons of fission yield.

Set 3 (problems 8 and 9) shows the fallout patterns calculated for two different wind situations for the largest source selected from the 1966 alignment of the "first pass—Route 17A." The total yield of the source is 30 Mt; appearing as fallout are the fission products from 80 tons of fission and induced activities equivalent to 1.46 kt of fission yield.

Set 4 (problem 10) shows the total fallout pattern calculated on the assumption that all 25 detonations of the "first pass—Route 17A" were on the same day. The yield of the 25 detonations was taken from the 1966 alignment.

DISCUSSION OF SALIENT FEATURES OF THE PROBLEMS

Problem Set 1

The effect of changing the base-surge radius from 33,000 to 18,000 m (problems 1 and 2) is that the isopleths of total exposure have been extended in range along the hot line associated with the base-surge deposition as follows: The 1-R isopleth has about 4 miles of additional range, the 0.5-R isopleth has about 8 miles of additional range, and the 0.2-R isopleth has about 20 miles of additional range. Physically, such an extension occurs because the fraction of the radioactivity per unit area along this hot line is increased by decreasing the initial base-surge radius. It appears that even a variation of a factor of 2 in the base-surge radius will not produce a significant alteration in the predicted total exposure.

In problems 2 and 3, the base-surge height was decreased by 1200 m. The

resulting effect on the total exposure pattern is slight.

Problem 4 illustrates the total exposure pattern that would occur if (a) there were complete ignorance of the wind direction in the lowest 1000 m of the atmosphere, and (b) the wind speed were randomly selected between 0 and 15 knots in this layer. This problem illustrates patterns that, under these randomly selected wind conditions, do not remain in the previously described sector. In all, 30 such fallout patterns were calculated. It should be noted that about two-thirds of these patterns remained in the sector defined for the 1964 studies.⁸⁴ The radioactivity associated with the smallest particles falling out of the sector lies within a 3-hr travel time from the edge of the sector. Thus, it would appear that if the meteorological program defined some layer of the atmosphere in which the winds were unpredictable (due to local topography, solar insolation effects, or land/water distributions), then the uncertainty in the calculated pattern should be equivalent to a 3-hr travel time at the edge of the predicted pattern.

Problem 5, when compared to problem 1, illustrates the change that can occur in the fallout pattern if both the base-surge and the main-cloud height are increased by a factor of 2. It is clear in this case that if the clouds were twice as high as predicted, the fallout pattern would extend both over the islands in the Gulf of Panama and towards the Azuero Peninsula.

Problem Sets 2 and 3

Problems 6 and 7 show the fallout patterns for the smallest radioactive source and the smallest total yield (1966 align-

ment) for two different in-sector wind conditions. These two patterns should be compared to the patterns associated with the largest radioactive source and cloud dimensions and the same two wind conditions (set 3, problems 8 and 9). It is obvious that the area covered by the pattern from the small source is at least a factor of 2 less than the area from the larger.

It should be noted that the maximum range in problems 6 and 7 to the edge of the 0.5-R isopleth is 25 miles. If this maximum range is compared to the average sector width of 45 miles in the 1964 alignment, it can be concluded that the 0.5-R isopleth from these two small detonations would be contained in the sector, even if the wind direction had been different by nearly 90 deg. The implications of this are that detonations involving smaller clouds and smaller radioactive sources may not require as rigid meteorological restrictions as larger detonation do to keep them within the exclusion zone. This characteristic of fallout patterns was suspected by H. Ellsaesser,⁸⁵ and it may have a definite impact on operational shot schedules.

From the extent of the 0.1-R isopleth in problems 8 and 9, one can conclude that in-sector winds, or very light winds, must be selected for the largest detonations in order to avoid out-of-sector deposition of 0.1 R.

Problem Set 4

Problem 10 shows the total exposure pattern from all detonations of the 1966 alignment of the "first pass—Route 17A," assuming that they were all detonated on the same day and under the same wind

conditions. The patterns were found to be somewhat variable on five different days; the range to the in-sector exposure isopleths is 80 to 90 miles for the 0.5-R isopleth and 140 to 240 miles for the 0.1-R isopleth.

It should be stressed that this problem uses a method of estimating the exposure from the time of arrival to infinity that has been used in many past studies of large-scale nuclear excavation. We feel that, in view of the results of problem sets 2 and 3, this historical method is invalid because the fallout pattern from each detonation is calculated with some assumed shot-time wind. In reality, the wind associated with each detonation would be different and hence result in a broader, less intense pattern.

GAMING ANALYSIS OF THE RADIO-ACTIVITY PROBLEM ASSOCIATED WITH CANAL DIGGING

With the capabilities just illustrated regarding KFOC, we feel that a gaming analysis of the external-gamma-radioactivity problems associated with nuclear canal digging could be performed. Assume that:

1. A randomly selected but complete year of wind data is available.
2. The operational and engineering teams on-site are capable of holding a small, a medium, and a large detonation in readiness for firing so that any single one could be fired if suitable wind conditions arose.
3. An appropriate exclusion zone is definable.

Methodology

1. Beginning with the first day, the winds are tested with a KFOC cal-

culution to ascertain if the fallout patterns of the small, medium, or large detonation satisfy the yet-to-be-defined criteria of an acceptable shot day as a function of the yield.

2. If the answer to the preceding step is "yes" (i.e., that at least one detonation could be fired), the calculated total exposure pattern of the larger (or largest) detonation is stored in memory and we record which of the detonations is fired. In addition, one should consider firing more than one detonation, though not simultaneously, during a favorable day.
3. We assume that Y days intervene, during which the expended detonations are not available, but if other ready detonations can be fired, they are.
4. The game is continued according to the above assumptions and steps.
5. The results of the game are analyzed in order to ascertain how many of the canal detonations could have been fired in the year selected.
6. The completed results of the game are investigated with regard to air blast and engineering in order to ascertain the impact of those areas on the completed analysis. For air blast, it should be ascertained how many of the selected shot days would have been eliminated on the basis of adverse ducting conditions in the upper atmosphere. For engineering, it should be ascertained if the assumed schedule is reasonable or unreasonable. This feedback would then be included in order to alter the results. The completed

games would offer a basis for answering the question, "How feasible is it to dig a transisthmian canal by nuclear means?"

Key Questions

1. What is an acceptable shot day for each route (if different) for a small source?
2. What is an acceptable shot day for a large source?
3. What is the climatology of shot days 1 and 2 for each route?
4. To assure that the definitions of shot days 1 and 2 are appropriate, what is the sensitivity of cloud height to (a) water content in the initial bubble, (b) water content in the environment, and (c) atmospheric thermal structure? These factors, in our opinion, have not been adequately evaluated to date with regard to large-scale excavation in saturated material. The importance of these factors on calculated cloud-growth histories for different yields has been previously reported by Huebsch.⁸⁶
5. What is the range of water content in typical shot environments?
6. If a nuclear cratering experiment should be conducted in saturated materials, the following features should be thoroughly explored with measurements:
 - a) Partitioning of radioactivity between the base-surge and main clouds.
 - b) Shifts in radioactivity/particle-size distributions for significant

nuclides resulting from the different shot environment or yield.

- c) Shift in F_c resulting from a large water content in the shot environment.
- d) Any marked changes in the vented fraction for significant species.

Other key questions are enumerated in Chapter 5. Answers to these questions are clearly not available at this time; however, the Technical Working Group on Radioactivity will need to determine the feasibility of nuclear excavation of the transisthmian canal (from their point of view) in the absence of answers to these questions. The capabilities (KFOC) described in Chapters 4 and 6 can be used to examine the consequences of ignorances in these key areas on the frequency of acceptable shot days and hence on feasibility.

In regard to the radioactivity studies for the transisthmian canal, it is necessary to know or to make a judgement on whether NTS fallout experience, influenced by the shot-day criteria discussed in Chapter 3, is applicable. In this regard, it is indeed fortunate that in Panama the season of highest frequency of acceptable winds is during the dry season,¹⁶ for it will be during this season that, in our opinion, the shot-day criteria for the Panama environment may resemble those at NTS. It may very well be that it is only during the Central American dry season that our fallout-prediction experience gained at middle latitudes can be transferred to this tropical region with reasonable confidence.

Example 1

Number of detonations:

1

Total yield:

18 Mt

Number of devices:

5

Individual device yields:

5, 5, 5, 2, and 1 Mt

Total fission yield vented:

100 tons

Induced equivalent fission yield vented:

3.0 kt

Distribution of vented radioactivity:

60% in base surge

40% in main cloud

Base-surge dimensions:

Height 5,200 m

Radius 33,000 m

Main-cloud dimensions:

Height 8,800 m

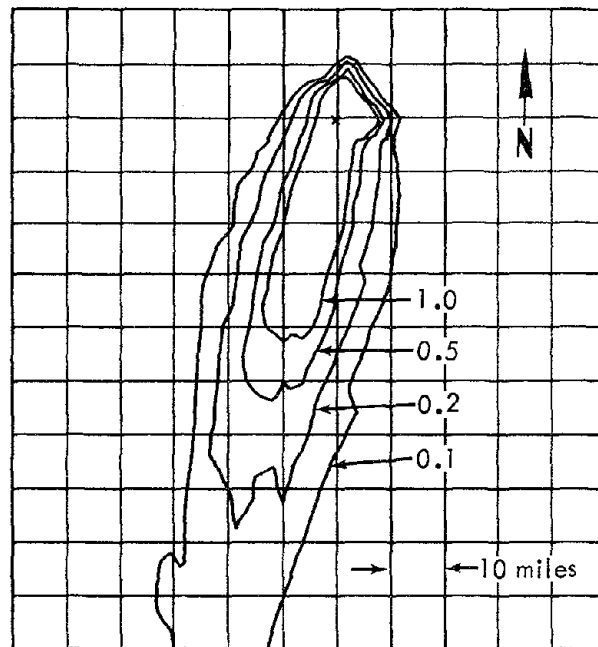
Radius 5,500 m

Particle radii:

Largest 500 μ

Smallest 10 μ

The activity/particle-size distributions are taken from Chapter 4 (Sedan), and the wind parameters are given below the fallout pattern. The isoexposure lines in the fallout pattern represent exposures (in roentgens) from the time of arrival to infinity.



Height (m)	0	500	1000	1500	2000	2500	3000	4000	5000	6000	7000	8000	9000	10,000
Direction (deg)	12	13	14	16	14	4	8	6	5	4	4	51	64	80
Speed (m/sec)	3.9	4.9	2	1	1	2	3	3.9	4.9	2	1	5.9	7.9	7.9

Example 2

Number of detonations:

1

Total yield:

18 Mt

Number of devices:

5

Individual device yields:

5, 5, 5, 2, and 1 Mt

Total fission yield vented:

100 tons

Induced equivalent fission yield vented:

3.0 kt

Distribution of vented radioactivity:

60% in base surge

40% in main cloud

Base-surge dimensions:

Height 5,200 m

Radius 18,000 m

Main-cloud dimensions:

Height 8,800 m

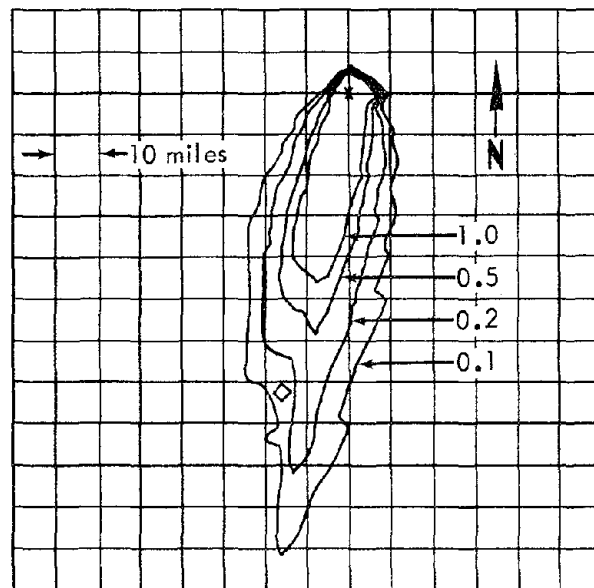
Radius 5,500 m

Particle radii:

Largest 500 μ

Smallest 10 μ

The activity/particle-size distributions are taken from Chapter 4 (Sedan), and the wind parameters, which are the same as those in example 1, are given below the fallout pattern. The isoexposure lines in the fallout pattern represent exposures (in roentgens) from the time of arrival to infinity.



Height (m)	0	500	1000	1500	2000	2500	3000	4000	5000	6000	7000	8000	9000	10,000
Direction (deg)	12	13	14	16	14	4	8	6	5	4	4	51	64	80
Speed (m·sec)	3.9	4.9	2	1	1	2	3	3.9	4.9	2	1	5.9	7.9	7.9

Example 3

Number of detonations:

1

Total yield:

18 Mt

Number of devices:

5

Individual device yields:

5, 5, 5, 2, and 1 Mt

Total fission yield vented:

100 tons

Induced equivalent fission yield vented:

3.0 kt

Distribution of vented radioactivity:

60% in base surge

40% in main cloud

Base-surge dimensions:

Height 4,000 m

Radius 18,000 m

Main-cloud dimensions:

Height 8,800 m

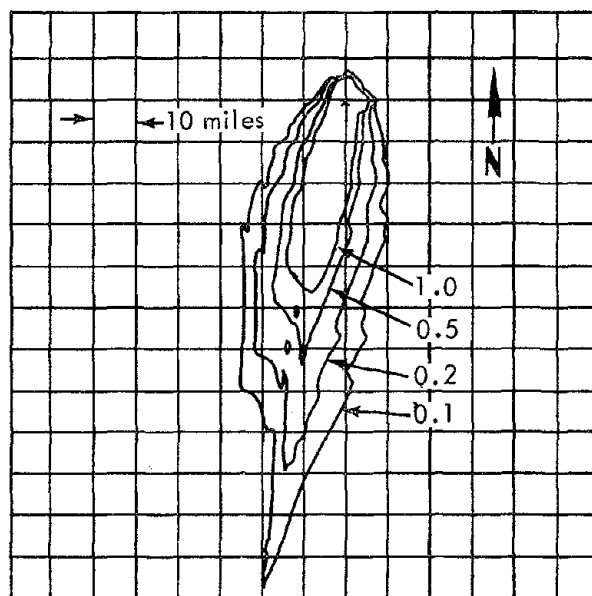
Radius 5,500 m

Particle radii:

Largest 500 μ

Smallest 10 μ

The activity/particle-size distributions are taken from Chapter 4 (Sedan), and the wind parameters, which are the same as those in example 1, are given below the fallout pattern. The isoexposure lines in the fallout pattern represent exposures (in roentgens) from the time of arrival to infinity.



Height (m)	0	500	1000	1500	2000	2500	3000	4000	5000	6000	7000	8000	9000	10,000
Direction (deg)	12	13	14	16	14	4	8	6	5	4	4	51	64	80
Speed (m/sec)	3.9	4.9	2	1	1	2	3	3.9	4.9	2	1	5.9	7.9	7.9

Example 4

Number of detonations:

1

Total yield:

18 Mt

Number of devices:

5

Individual device yields:

5, 5, 5, 2, and 1 Mt

Total fission yield vented:

100 tons

Induced equivalent fission yield vented:

3.0 kt

Distribution of vented radioactivity:

60% in base surge

40% in main cloud

Base-surge dimensions:

Height 4,000 m

Radius 18,000 m

Main-cloud dimensions:

Height 8,000 m

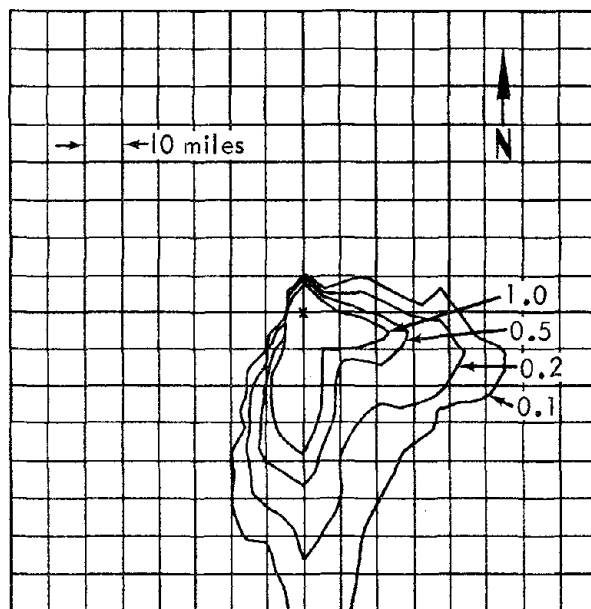
Radius 5,500 m

Particle radii:

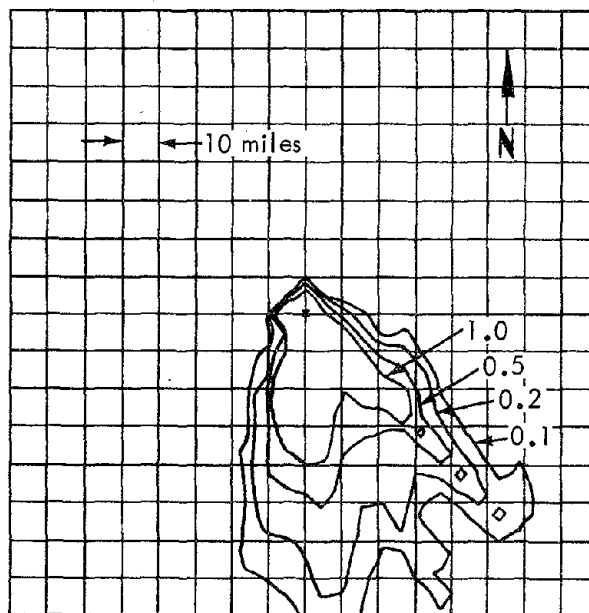
Largest 500 μ

Smallest 10 μ

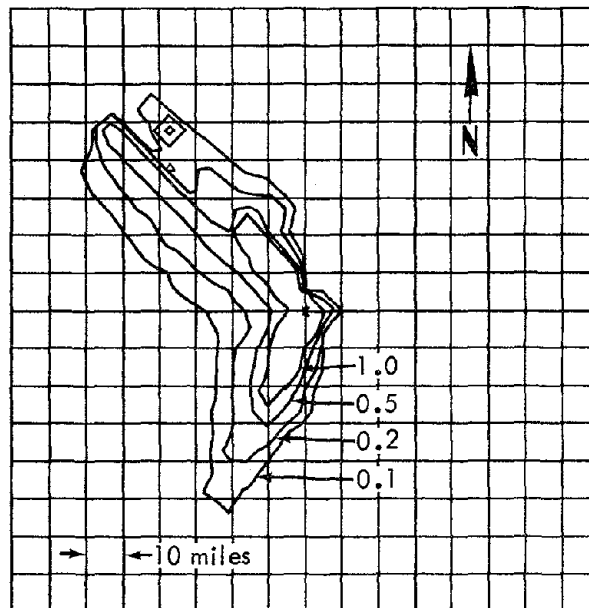
The activity/particle-size distributions are taken from Chapter 4 (Sedan), and the wind parameters, which are the same as those in example 1 except for random winds in the lowest 500 m, are given below the fallout patterns. The isosexposure lines in the fallout patterns represent exposures (in roentgens) from the time of arrival to infinity.



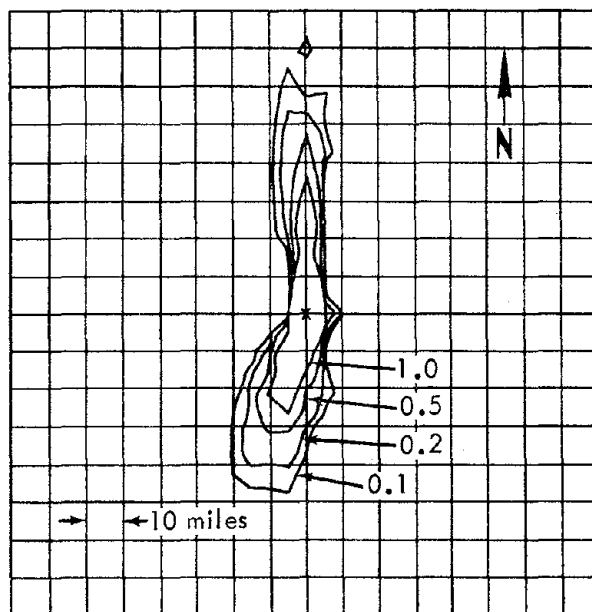
Height (m)	0	500	1000	1500	2000	2500	3000	4000	5000	6000	7000	8000	9000	10,000
Direction (deg)	204	179	14	16	14	4	8	6	5	4	4	51	64	80
Speed (m/sec)	1.2	5.8	2	1	1	2	3	3.9	4.9	2	1	5.9	7.9	7.9



Height (m)	0	500	1000	1500	2000	2500	3000	4000	5000	6000	7000	8000	9000	10,000
Direction (deg)	28	258	14	16	14	4	8	6	5	4	4	51	64	80
Speed (m sec)	3.7	4.2	2	1	1	2	3	3.9	4.9	2	1	5.9	7.9	7.9



Height (m)	0	500	1000	1500	2000	2500	3000	4000	5000	6000	7000	8000	9000	10,000
Direction (deg)	316	312	14	16	14	4	8	6	5	4	4	51	64	80
Speed (m sec)	0.8	6.4	2	1	1	2	3	3.9	4.9	2	1	5.9	7.9	7.9



Height (m)	0	500	1000	1500	2000	2500	3000	4000	5000	6000	7000	8000	9000	10,000
Direction (deg)	355	145	14	16	14	4	8	6	5	4	4	51	64	80
Speed (m sec)	0.6	7.6	2	1	1	2	3	3.9	4.9	2	1	5.9	7.9	7.9

Example 5

Number of detonations:

1

Total yield:

18 Mt

Number of devices:

5

Individual device yields:

5, 5, 5, 2, and 1 Mt

Total fission yield vented:

100 tons

Induced equivalent fission yield vented:

3.0 kt

Distribution of vented radioactivity:

60% in base surge

40% in main cloud

Base-surge dimensions:

Height 8,000 m

Radius 33,000 m

Main-cloud dimensions:

Height 17,600 m

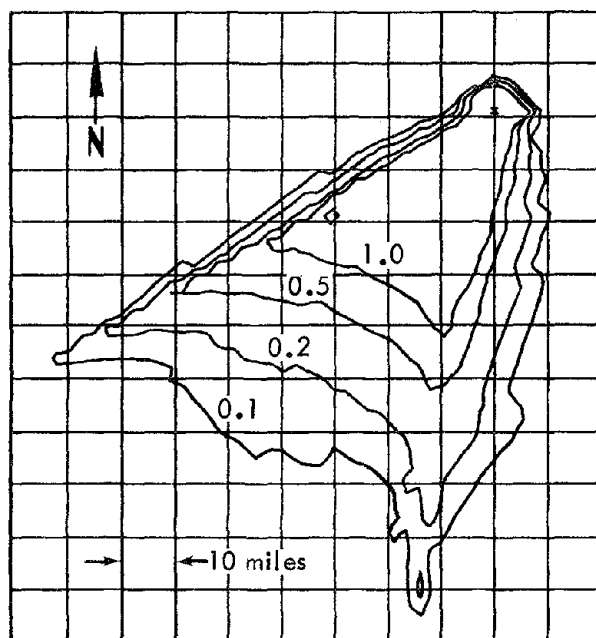
Radius 5,500 m

Particle radii:

Largest 500 μ

Smallest 10 μ

The activity/particle-size distributions are taken from Chapter 4 (Sedan), and the wind parameters, which are the same as those in example 1, are given below the fallout pattern. The isoexposure lines in the fallout pattern represent exposures (in roentgens) from the time of arrival to infinity.



Height (m)	0	500	1000	1500	2000	2500	3000	4000	5000	6000	7000	8000	9000	10,000	14,000	18,000
Direction (deg)	12	13	14	16	14	4	8	6	5	4	4	51	64	80	80	80
Speed (m/sec)	3.9	4.9	2	1	1	2	3	3.9	4.9	2	1	5.9	7.9	7.9	7.9	7.9

Examples 6 and 7

Number of detonations:

1

Total yield:

1.0 Mt

Number of devices:

5

Individual device yields:

200 kt each

Total fission yield vented:

100 tons

Induced equivalent fission yield vented:

280 kt

Distribution of vented radioactivity:

60% in base surge

40% in main cloud

Base-surge dimensions:

Height 2,200 m

Radius 11,000 m

Main-cloud dimensions:

Height 5,800 m

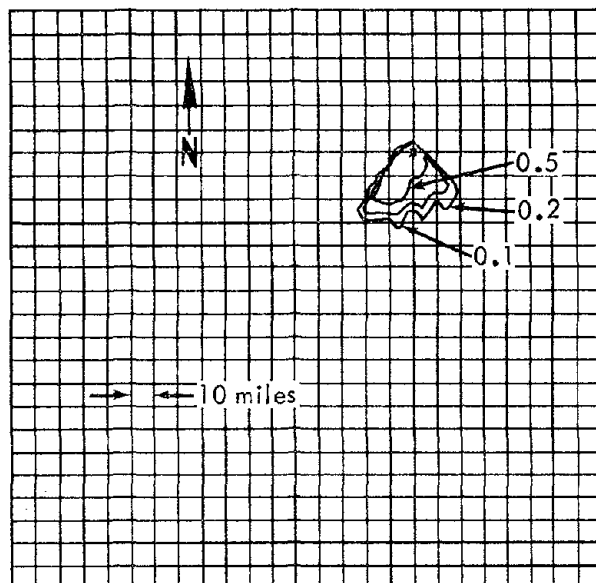
Radius 1,300 m

Particle radii:

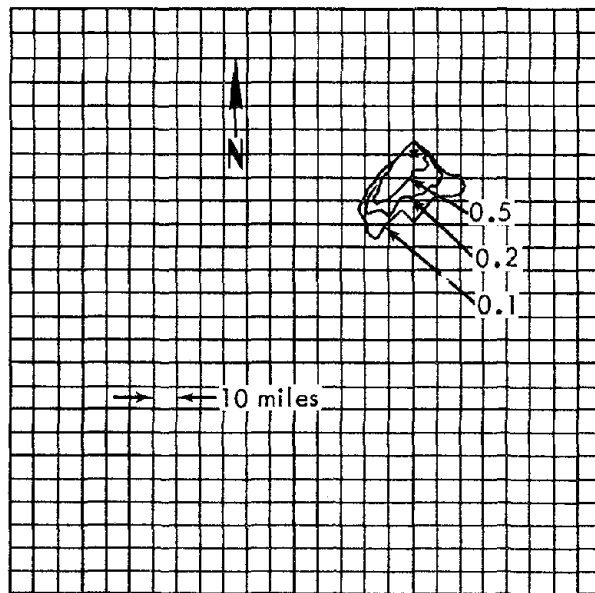
Largest 500 μ

Smallest 10 μ

The activity/particle-size distributions are taken from Chapter 4 (Sedan), and the wind parameters are given below the fallout patterns. The isoexposure lines in the fallout patterns represent exposures (in roentgens) from the time of arrival to infinity.



Height (m)	0	150	300	500	1000	1500	2000	2500	3000	4000	5000	6000	7000	8000	9000	10,000	11,000	12,000
Direction (deg)	10	315	325	336	10	30	40	55	60	90	230	305	310	310	270	270	220	210
Speed (m sec)	4	5	6	6	8	7	6	5	9	7	3	3	6	7	5	4	5	16



Height (m)	0	150	300	500	1000	1500	2000	2500	3000	4000	5000	6000	7000	8000	9000	10,000	11,000	12,000
Direction (deg)	283	315	360	15	30	35	40	40	60	53	90	30	10	267	290	285	310	140
Speed (m sec)	5	5	4	5	6	4	5	6	5	4	3	3	2	5	4	3	1	2

Examples 8 and 9

Number of detonations:

1

Total yield:

30 Mt

Number of devices:

4

Individual device yields:

10, 10, 5, and 5 Mt

Total fission yield vented:

80 tons

Induced equivalent fission yield vented:

1.46 kt

Distribution of vented radioactivity:

60% in base surge

40% in main cloud

Base-surge dimensions:

Height 4,250 m

Radius 30,500 m

Main-cloud dimensions:

Height 11,400 m

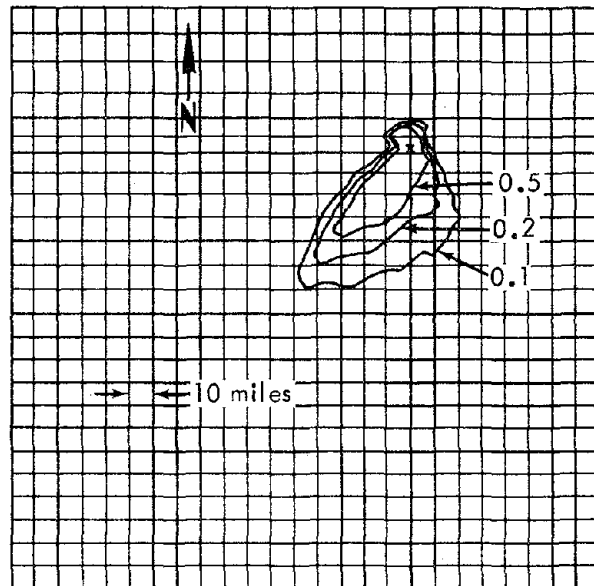
Radius 7,600 m

Particle radii:

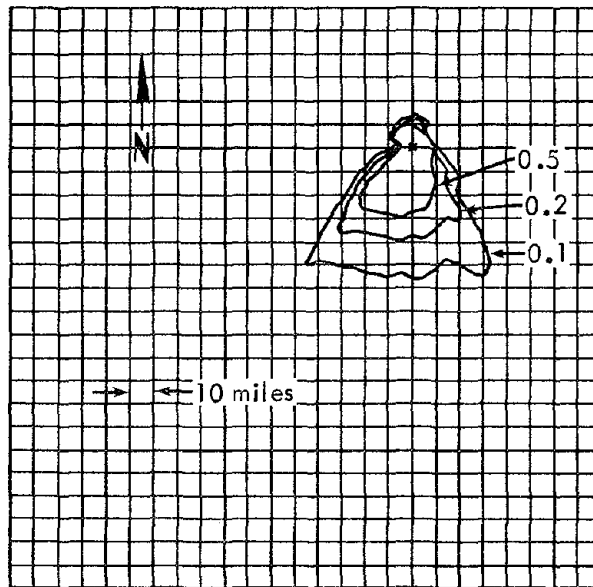
Largest 500 μ

Smallest 10 μ

The activity/particle-size distributions are taken from Chapter 4 (Sedan), and the wind parameters are given below the fallout patterns. The isoexposure lines in the fallout patterns represent exposures (in roentgens) from the time of arrival to infinity.



Height (m)	0	150	300	500	1000	1500	2000	2500	3000	4000	5000	6000	7000	8000	9000	10,000	11,000	12,000
Direction (deg)	283	315	326	15	30	35	40	40	60	53	90	30	10	267	290	285	310	140
Speed (m sec)	5	5	4	5	6	4	5	6	5	4	3	3	2	5	4	3	1	2



Height (m)	0	150	300	500	1000	1500	2000	2500	3000	4000	5000	6000	7000	8000	9000	10,000	11,000	12,000
Direction (deg)	310	315	325	336	10	30	40	55	60	90	230	305	310	310	270	270	220	210
Speed (m sec)	4	5	6	6	8	7	6	5	9	7	3	3	6	7	5	4	5	16

Example 10

Number of detonations:

25

Radius 30,500 m (largest)
11,000 m (smallest)

Total yield:

162 Mt

Main-cloud dimensions:

Height 11,400 m (largest)
5,800 m (smallest)

Number of devices:

149

Radius 7,600 m (largest)
1,300 m (smallest)

Individual device yields:

See table below

Total fission yield vented:

3 kt

Particle radii:

Largest 500 μ
Smallest 10 μ

Induced equivalent fission yield vented:

18.6 kt

Distribution of vented radioactivity:

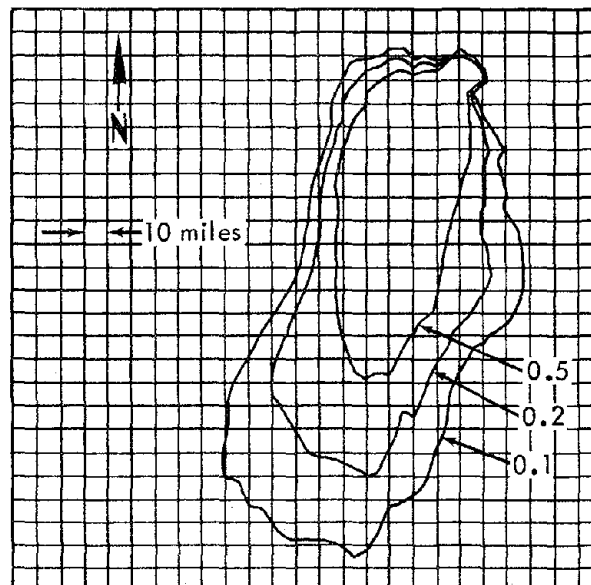
60% in base surge

40% in main cloud

Base-surge dimensions:

Height 4,250 m (largest)
2,200 m (smallest)

The activity/particle-size distributions are taken from Chapter 4 (Sedan), and the wind parameters are given below the fallout pattern. The isoexposure lines in the fallout pattern represent exposures (in roentgens) from the time of arrival to infinity.



Height (m)	0	150	300	500	1000	1500	2000	2500	3000	4000	5000	6000	7000	8000	9000	10,000	11,000	12,000
Direction (deg)	90	75	45	15	325	24	10	345	360	360	35	60	60	45	341	16	100	200
Speed (m sec)	3	3	2	2	2	1	2	2	3	3	4	6	6	3	3	3	1	1

Individual device yields in example 10

Detonation No.	Total number of devices in detonation	Number of devices in detonation having yields of:					
		0.2 Mt	0.5 Mt	1.0 Mt	2.0 Mt	5.0 Mt	10.0 Mt
1	6	6					
2	5	4	1				
3	5		5				
4	5	3	2				
5	10		10				
6	6		3	1	1	1	
7	5	1	2	1	1		
8	5	5					
9	6	6					
10	6	6					
11	6	6					
12	5	3	2				
13	5		5				
14	10			10			
15	5			5			
16	6		6				
17	5		5				
18	10		10				
19	10		10				
20	5			2	2	1	
21	5		4	1			
22	4					4	
23	4				1	3	
24	4					2	2
25	6			2	2	2	

Chapter 7: Dynamics of Nuclear Clouds

Joseph B. Knox

DESCRIPTIVE KNOWLEDGE OF NUCLEAR CLOUDS

Some descriptive information on nuclear clouds from subsurface detonations has been given in prior chapters; we summarize it briefly here.

- The dimensions of "stabilized" clouds formed by subsurface nuclear detonations in alluvium (with several weight percent of water) were discussed and summarized in Chapter 4.
- The dimensions of base-surge clouds from subsurface nuclear detonations were also discussed in Chapter 4 for a basalt medium (water content < 1 wt%).
- Preliminary schemes (developed from HE events) were proposed in Chapter 5 for specifying cloud dimensions at cloud-stabilization time for row-charge events. These schemes are preliminary in the sense that if and when actual dimensions for nuclear row-charge clouds become available, the schemes should be tested and altered, if necessary.
- In Chapter 6, we varied certain KFOC input parameters separately and compared the effects of the parameter change on the exposure pattern for Panama Canal applications. Results indicated that errors in cloud-height prediction produced

larger errors in the exposure pattern than a comparable error in cloud radius.

KEY QUESTIONS

Given below are the key questions regarding nuclear clouds resulting from cratering shots:

- For different fractions of the vented explosive energy, what is the variation in the in-cloud circulation and the cloud development?
- How long can the toroidal (in-cloud) motion have velocities significantly larger than the sedimentation velocities of the particles?
- What variation in the thermodynamics of cloud rise can be expected as (a) the water content in the shot environment is altered, (b) the water-vapor content of the atmospheric environment is altered, and (c) the thermal structure of the atmosphere is changed?
- What tools are available to explore these questions? What, if any, large-amplitude, two-dimensional atmospheric-convection calculations have been performed?

Past work on numerical simulation of atmospheric convection has been restricted to consideration of initial conditions involving warm finite-size bubbles of air in which the temperature is about 1°C higher

than that in the environment. Such convection we term small-amplitude convection. Most of the interest of atmospheric scientists has been in this area with or without the inclusion of the conservation equation for water vapor and/or liquid water. By large-amplitude convection, we mean that the initial warm bubble in the atmosphere is of finite size and that the temperature of the air within the bubble significantly exceeds that of the

surrounding air. Table 7 summarizes numerical-simulation work on both large- and small-amplitude convection.

A TENSOR SIMULATION OF LARGE-AMPLITUDE CONVECTION

The first large-amplitude, two-dimensional (with cylindrical symmetry) numerical simulation of dry convection was performed at LRL as a result of the interest of the LRL air-blast study group

Table 7. Summary of numerical-simulation work on convection in the atmosphere.

Kind of convection	Description of work in:	
	One dimension in space	Two dimensions in space
Small amplitude, dry	—	Malkus and Witt ⁸⁷ —Eulerian calculation with diffusivity of heat and momentum equal. Since fluid speeds are much less than the speed of sound, the incompressibility assumption is made in calculating velocities. Computational stability problems restricted the calculations in time. Lilly ⁸⁸ —Eulerian calculation with a staggered grid and nonlinear viscous terms. Integrations physical to 40 min depicted the organizing, rising, and decaying phases of a convective cell.
Small amplitude, moist	—	Lilly ⁸⁹ Ogura ⁹⁰ Orville ⁹¹
Small amplitude, moist (including the antibuoyancy effect of liquid water)	—	Murray and Hollinden ⁹² —Eulerian calculation with the incompressibility approximation made for the computation of the field of motion. A nonlinear viscous term was used involving only the vertical velocity.
Large amplitude, dry or moist	Huebsch ⁸⁶ —Lagrangian solution of the rise of a finite-size bubble through a stratified atmosphere.	
Large amplitude, dry	—	LRL—application of TENSOR and CEL (1965-66). Viecelli ¹⁹ Knox ⁹³

in the venting of cavity gas as an air-blast source. This background is given so that the reader may understand the initial conditions and the zoning employed in the problem presented. Following an examination of truncation error,¹⁹ it was determined that in order to calculate with TENSOR the propagation of air-blast energies to distances on the order of 300 km with a grid spacing of 3 km, the initial energy source would have to be on the order of 500 Mt. The initial conditions selected were (a) a sound-speed profile that increased linearly with height to a representative stratospheric temperature at 60 km, (b) a free surface at 60 km, and (c) 500 Mt of energy uniformly distributed in a right cylinder 3 km in radius and 3 km in height. With appropriate modifications in the equation, TENSOR⁹⁴ is a two-dimensional Lagrangian equation-of-state hydrodynamics code for the atmosphere. It is possible to trace the evolution of the initial zone containing the source energy and hence, if one correlates the position of the thermal energy with that of radioactive tracers, the expansion and hydrodynamic growth of the buoyant bubble or the debris cloud. Figures 38, 39, 40, 41, and 42 show the evolution of the particle-velocity field, the configuration of the free surface at 60 km, and the fireball position. The most interesting features of these figures for cloud dynamics are (a) the excitation of very large waves on the free surface of the atmosphere and the corresponding vertical circulation, and (b) the evolution of the cloud boundary and the in-cloud circulation. Salient features are:

- The vertical asymmetry of the particle-velocity field and the shock

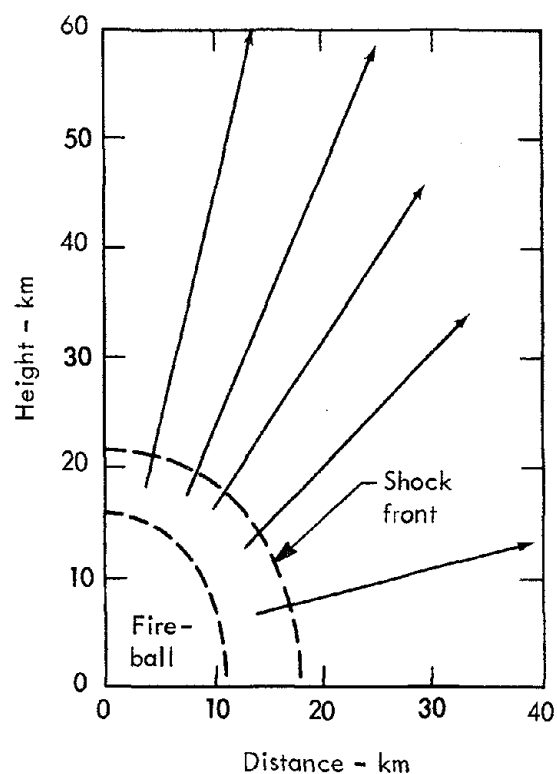


Fig. 38. TENSOR calculation of large-amplitude convection (time = 10.2 sec).

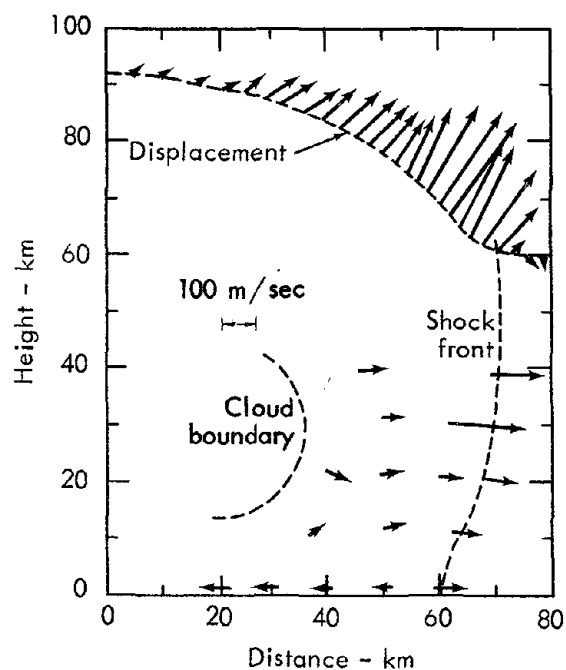


Fig. 39. TENSOR calculation of large-amplitude convection (time = 110 sec).

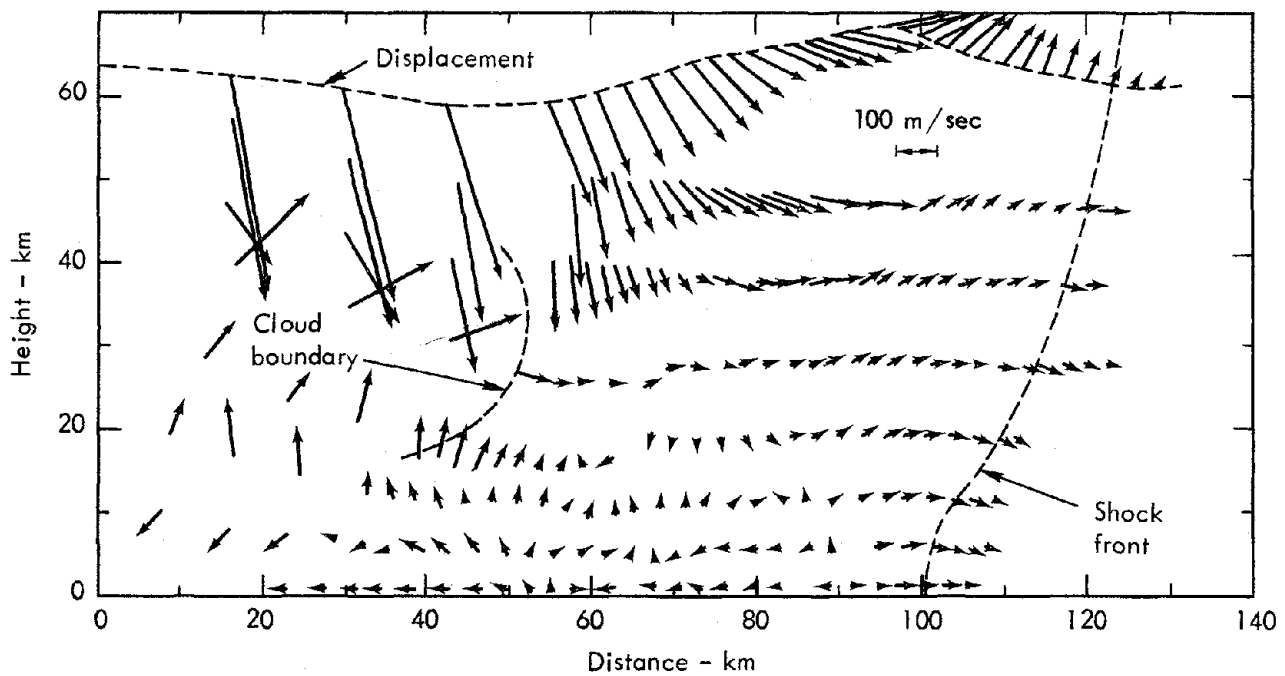


Fig. 40. TENSOR calculation of large-amplitude convection (time = 210 sec).

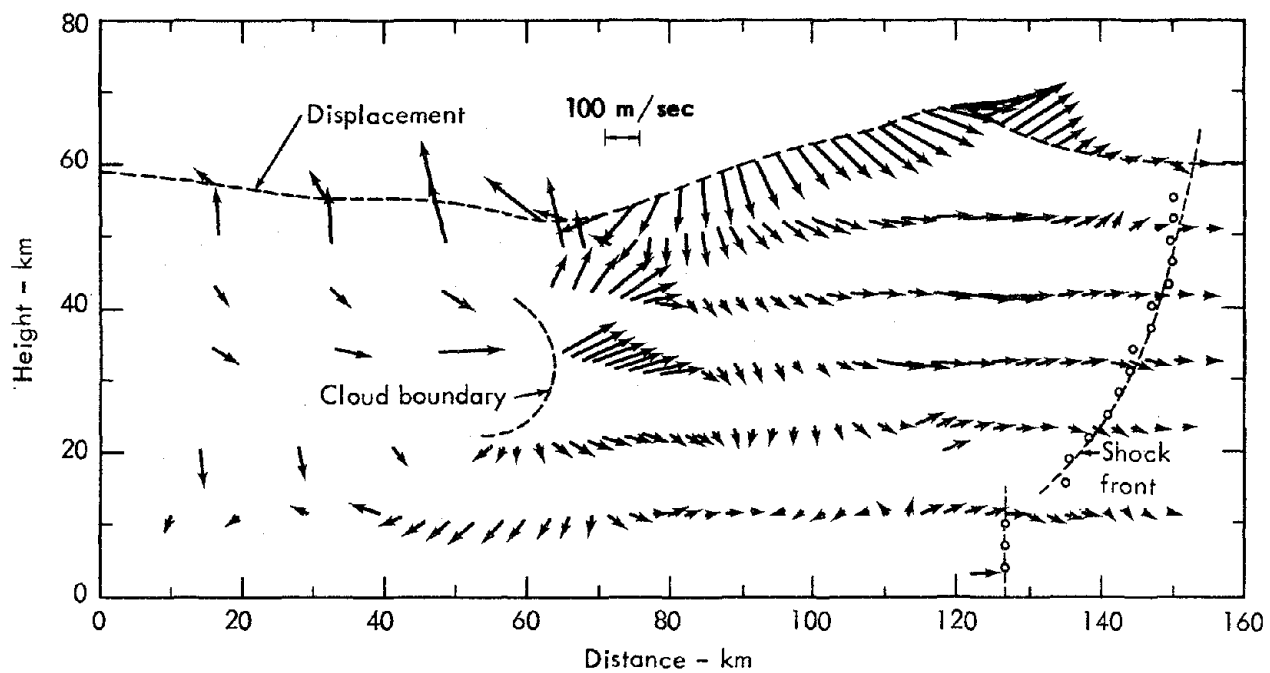


Fig. 41. TENSOR calculation of large-amplitude convection (time = 274 sec).

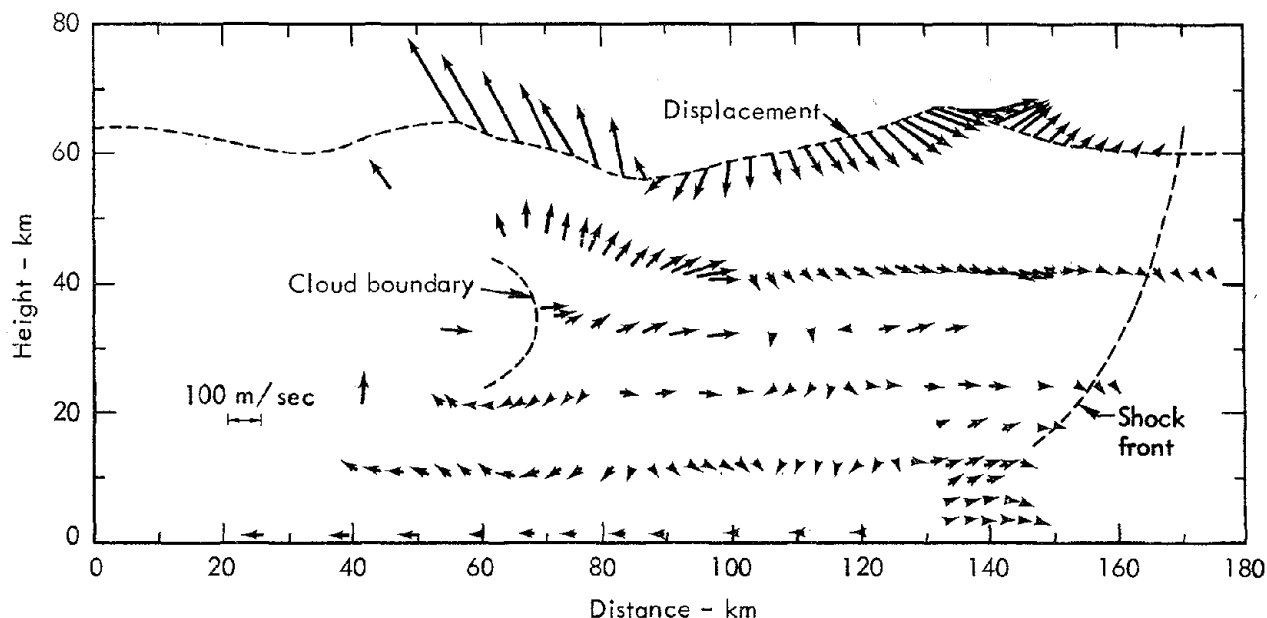


Fig. 42. TENSOR calculation of large-amplitude convection (time = 310 sec),

configuration at 10 sec (Fig. 38) is quite striking. Between 10 and 110 sec, rapid expansion and hydrodynamic growth of the debris cloud occurs, and a toroidal circulation develops. The resulting upward velocities in the debris cloud are sufficiently high that it is doubtful if any deposition occurs during this time interval.

- Figure 39 shows that the free surface originally at 60 km is elevated about 30 km above its original position after 110 sec. This results in the excitation of gravity waves, whose velocity fields are comparable at this high yield with those in the in-cloud (toroidal) circulation.
- Figures 40, 41, and 42 show the continued growth of the debris cloud and the interaction of the toroidal circulation and the velocity field from the gravity waves. Further,

it should be noted that the cloud stabilizes in height at about 6 min, whereas radial growth is calculated to be still in progress at that time.

In regard to verification of the cloud-height calculation, Fig. 43 shows mean cloud height (from Viecelli¹⁹) and mean cloud radius (from Glasstone²⁵) as a function of yield, with the latter curve extended to the 500-Mt range. It is interesting to note that the calculated cloud

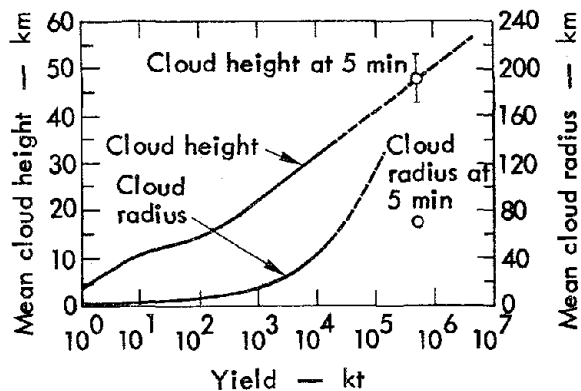


Fig. 43. Cloud-radius and -height curves from Viecelli¹⁹ and Glasstone.²⁵

height at 5 min compares well with the extension of the predicted curve. The calculated cloud radius, however, is about a factor of 2 smaller than that extrapolated from Glasstone.²⁵ At 5 min, the calculated cloud was still expanding fairly rapidly, whereas the vertical cloud growth was, by and large, stabilized by this time.

The results of this calculation of large-amplitude dry convection have important implications for fallout problems from a large energy release near the surface of the earth. It is clear that the in-cloud circulation will have sufficient strength and duration to have profound effects on the early deposition of particulate radioactivity. Existing sedimentation fallout models, if applied to such large energy releases near the surface, would not become valid until long (about 30 min) after the time of energy release. Another significant result is that under these conditions, the fields of motion driven by the gravity wave at the top of the atmosphere would interact with the cloud circulation to play an important role in the early distribution of radioactivity. This physical discussion of this problem was reported by Knox.⁹³

The next task was to check the calculated cloud evolution for Sedan against documentary photography. This we illustrate in the next sample calculation.

GEM SIMULATION OF THE DEVELOPMENT OF THE SEDAN MAIN CLOUD

With the development of a two-dimensional ray-tracing code for acoustical energy,⁹⁵ a tool was acquired for back-calculating, from observed long-range overpressures, the overpressure that must have existed in the warm bubble

resulting from the venting of the Sedan cavity gases. In this manner, Viecelli estimated that 1 kt of energy was injected into the atmosphere at the time of venting for Sedan. Hence, a reasonable estimate of the thermal source for the main cloud was obtained. With the specification of the thermal stratification of the atmosphere at shot time for Sedan, a GEM (two-dimensional Eulerian hydrodynamics) calculation of the main-cloud evolution could be made. Figures 44 and 45 show

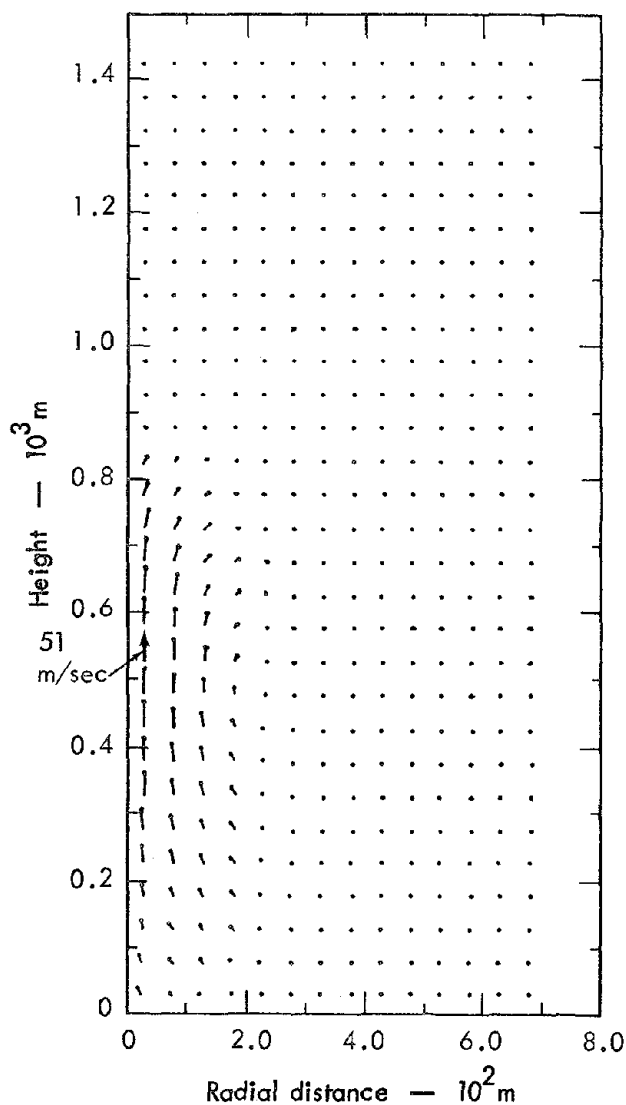


Fig. 44. Two-dimensional hydrodynamic calculation of the particle-velocity field in the Sedan main cloud at 30 sec.

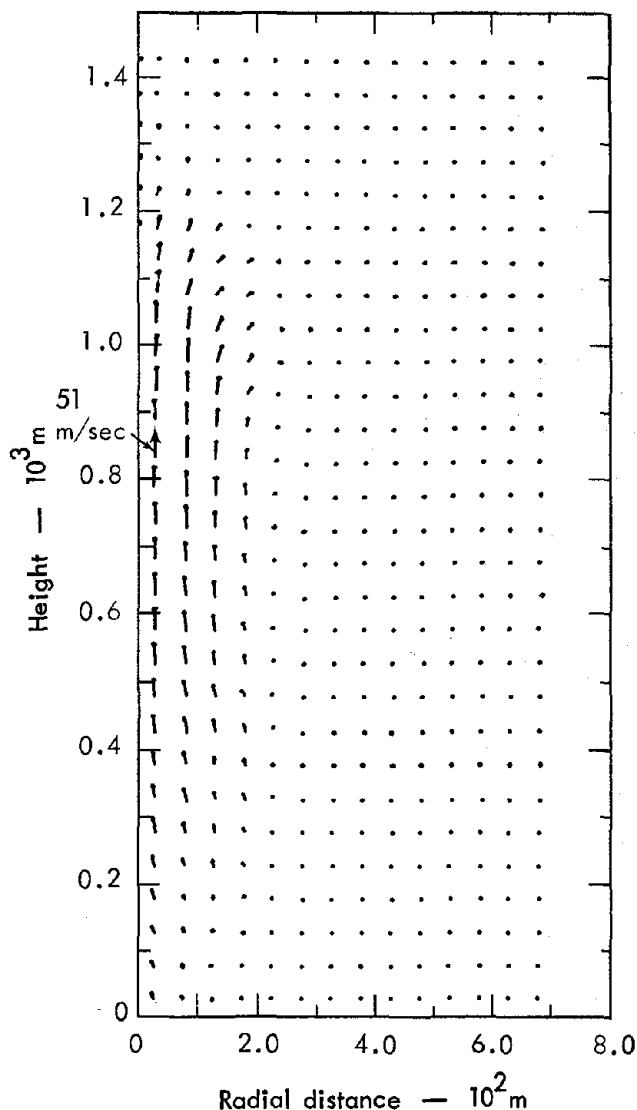


Fig. 45. Two-dimensional hydrodynamic calculation of the particle-velocity field in the Sedan main cloud at 44 sec.

the particle-velocity field in vertical section at 30 and 44 sec respectively. Figures 46, 47, 48, 49, and 50 show vertical sections of the temperature field at times of 10, 20, 30, 40, and 44 sec respectively.

At 10 sec, the shock has propagated out far enough so that the toroidal velocity field has begun organizing, and the originally spherical isotherms at a few seconds have already become distorted in this flow

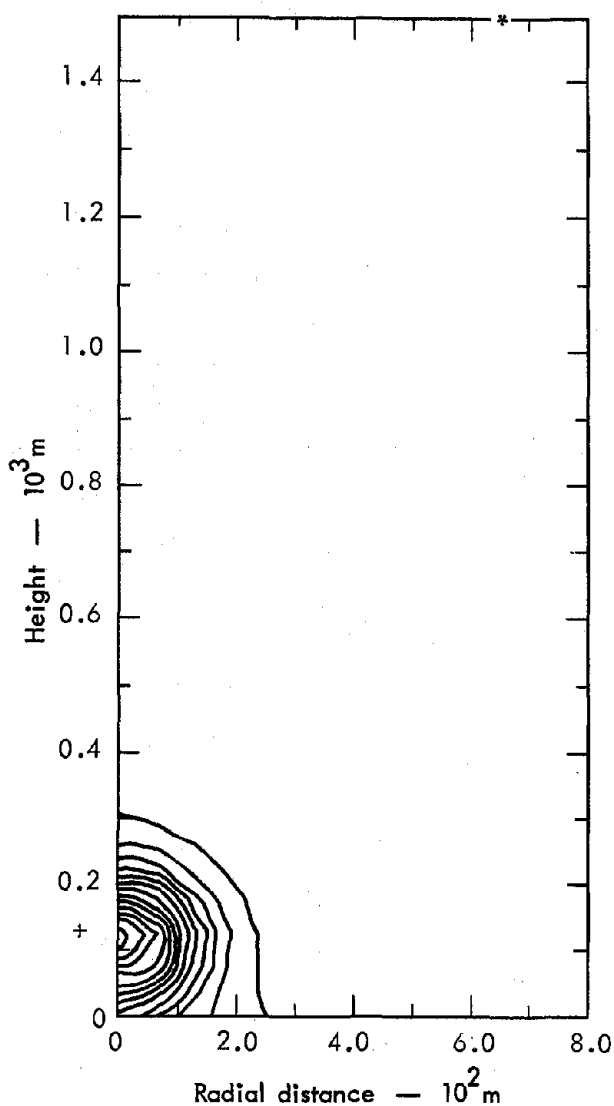


Fig. 46. Two-dimensional hydrodynamic calculation of the Sedan temperature field at 10 sec (+ = 670°K, * = 293°K).

pattern. This flow pattern has caused the "nose" of high temperature to extend radially outwards in the vicinity of 200 m from ground zero. During the organizing phase, the toroidal circulation has remained stationary and close to the ground surface. By 20 sec, the rise phase has clearly begun and the area of maximum velocity roughly coincides with the area of maximum temperature. The original "nose" of high temperature between 200

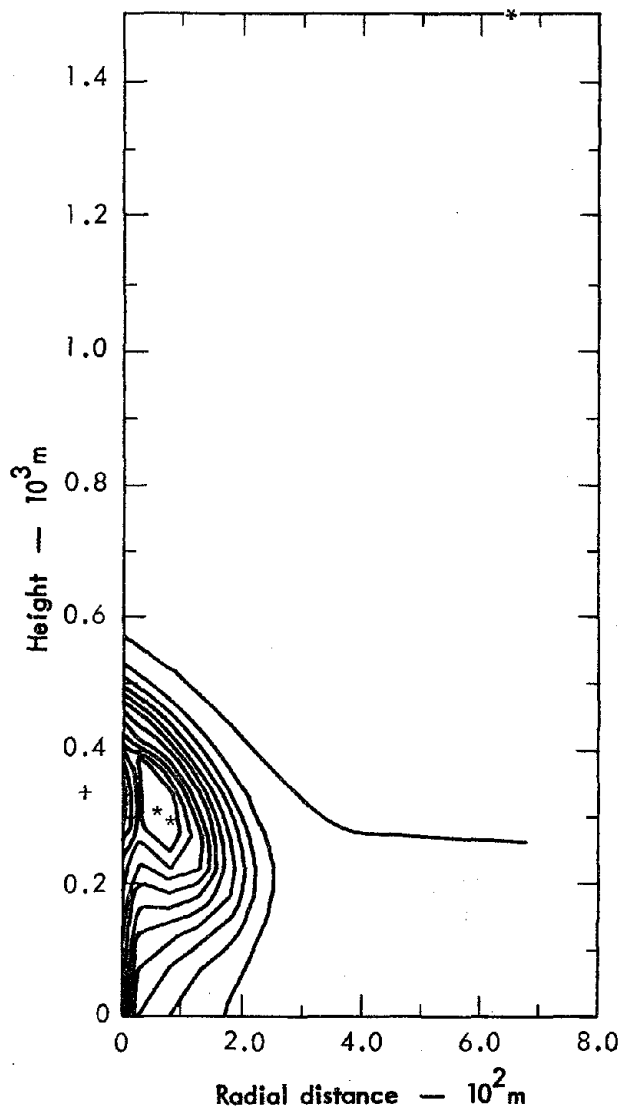


Fig. 47. Two-dimensional hydrodynamic calculation of the Sedan temperature field at 20 sec (+ = 464°K, * = 294°K, ** = 401°K).

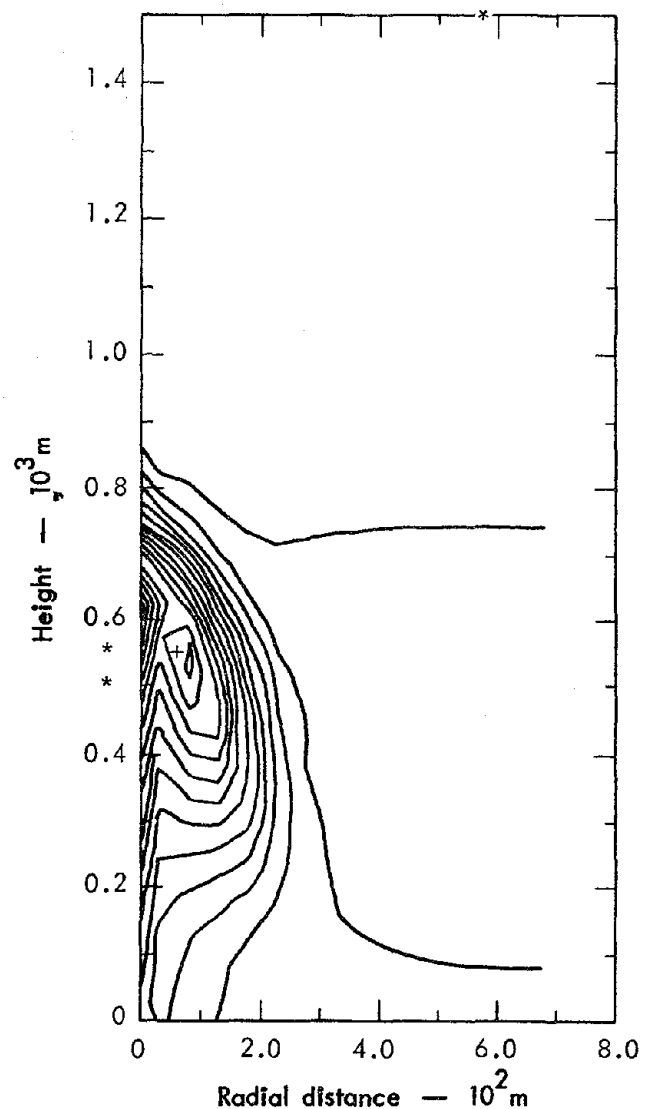


Fig. 48. Two-dimensional hydrodynamic calculation of the Sedan temperature field at 30 sec (+ = 361°K, * = 294°K, ** = 391°K).

and 300 m still persists. At 44 sec, the cloud is still in the rise phase with the temperature maximum coinciding with the maximum speed (51 m/sec) in the up-draft. It is interesting to note that the area of maximum thermal gradient near the circulation pole in Fig. 45 corresponds very nearly to the position of the outer edge of the observed main cloud at that time (Fig. 51). It appears that the edge of the thermal gradient and the edge of the main

cloud constitute the outer boundary for the rising jet of warm air and debris of the Sedan cloud. In Fig. 45, we have also noted the top of the visible main cloud at that time. The reasonable agreement between the shape of the temperature pattern and the observed dimensions of the Sedan cloud at 44 sec is taken as evidence that the GEM code has reasonably reproduced or simulated the early history of the Sedan buoyant bubble. It may be noted

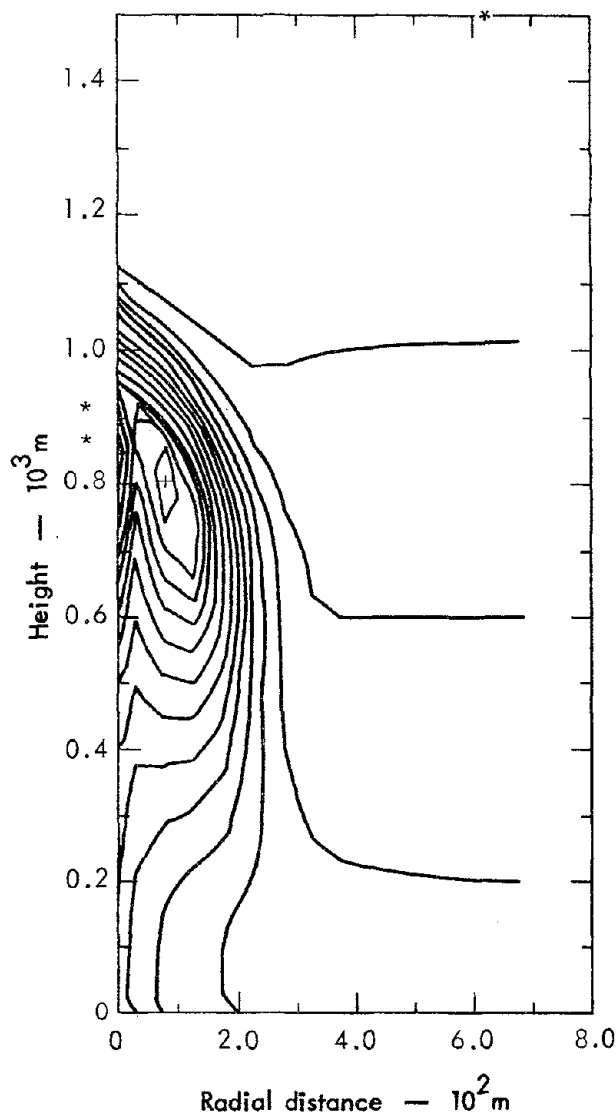


Fig. 49. Two-dimensional hydrodynamic calculation of the Sedan temperature field at 40 sec (+ = 341°K, * = 294°K, ** = 350°K).

that the maximum height of the zone of concentrated isotherms is about 1000 m at 44 sec, whereas the top of the visible cloud is at 1500 m at this same time. This discrepancy can be largely attributed to the fact that in reality the warm bubble was created a few hundred meters above the earth's surface rather than at the earth's surface as assumed in the calculation.

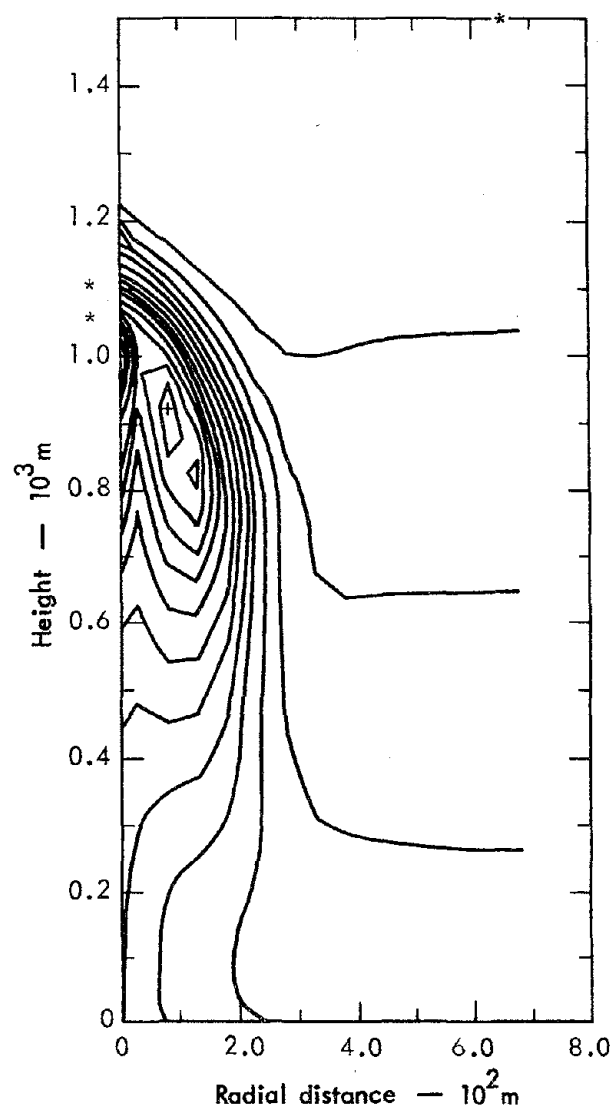
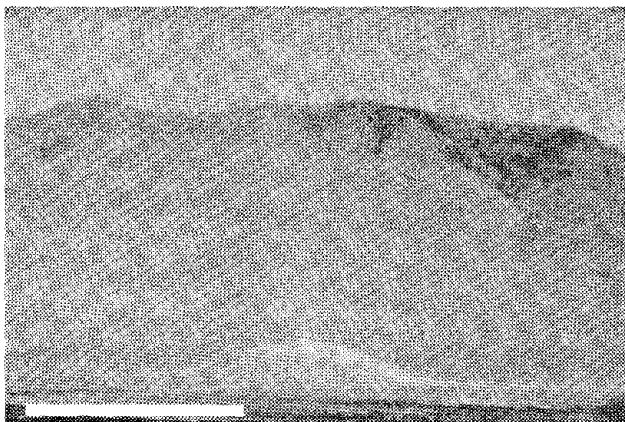


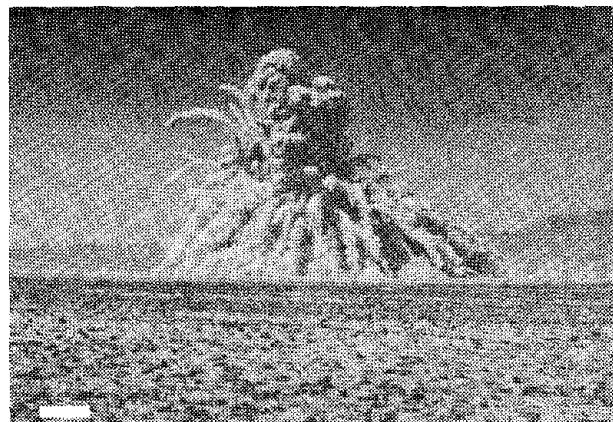
Fig. 50. Two-dimensional hydrodynamic calculation of the Sedan temperature field at 44 sec (+ = 333°K, * = 294°K, ** = 351°K).

CONCLUDING REMARKS

The investigation of numerical simulation of large-amplitude dry convection has resulted in the application of GEM to a test case—the Sedan main-cloud rise. The results suggest that here is at least one useful calculational tool for attacking the problem of nuclear-cloud formation.



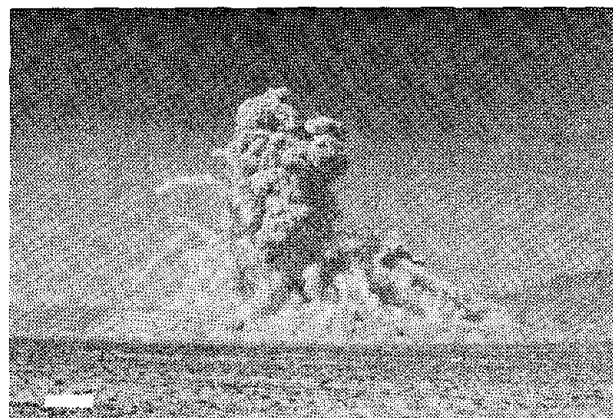
H + 1.9 sec



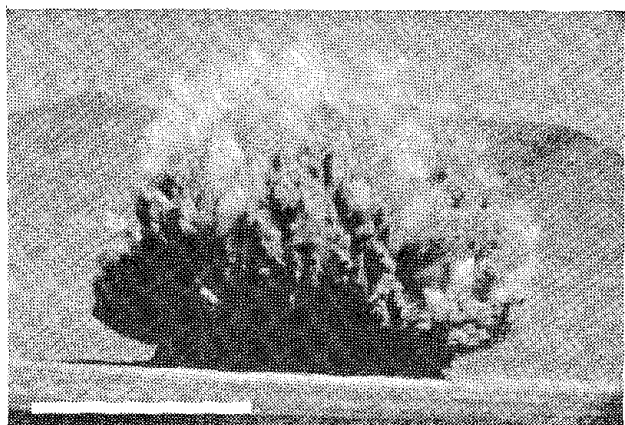
H + 27 sec



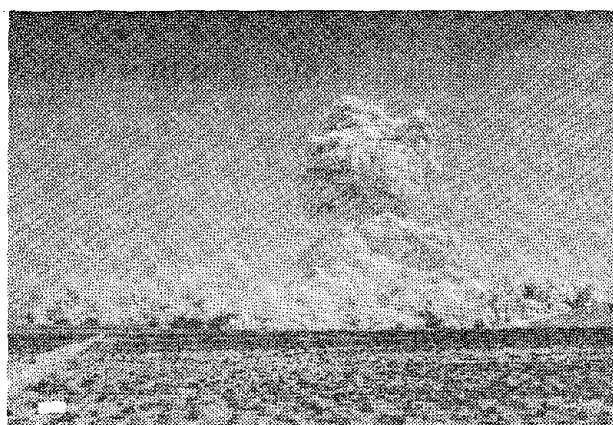
H + 2.8 sec



H + 39 sec



H + 4.0 sec



H + 360 sec

Fig. 51. Various stages of the Sedan cratering explosion (the white bar in each photograph represents a distance of 300 m; taken from Ref. 43).

If 15 kt of energy had been placed in the initial venting bubble for Sedan, the velocity of the central up-draft would have been 91 m/sec at 44 sec (separate GEM

calculation) as compared to our calculated value of 51 m/sec for 1 kt of released energy. These two calculational results indicate that the magnitude of the in-cloud

up-draft varies between the fourth and fifth power of the yield at early times. This finding is consistent with the empirical observation that nuclear-cloud heights are proportional to the 0.25 power of the yield. By simple scaling analysis, it can then be inferred that the vertical velocity in such clouds should be proportional to the 0.25 power of the yield. This seems to fit the results obtained by GEM for the cases calculated.

It appears that the GEM code can be used to explore variations of cloud growth with atmospheric thermal structure, and

probably the Huebsch code can be used in one dimension to explore the effect of water content in the bubble and water-vapor content in the atmospheric environment on cloud growth. In order to extend GEM runs to several minutes of real (cloud-development) time, future work will need to select the proper artificial viscosity.

ACKNOWLEDGMENT

The author is indebted to Mr. J. Viecegli for performing the GEM calculations referred to in this paper.

Chapter 8: Diffusion of Nuclear Clouds over Long Ranges

Todd V. Crawford

Previous chapters have dealt with the transport and fallout of clouds of particulate material. These particles, by and large, gravitationally fall to earth within 24 hr. In this chapter, the problem is extended further in time to include that material which falls with velocities the same order of magnitude as vertical transport velocities.

There are two logical subdivisions of the problem:

1. Predicting the location of the cloud as a function of time within a coordinate system fixed to the earth's surface.
2. Predicting the time and space variation of the pollutant concentration with respect to a coordinate system that travels with the cloud.

In order to predict realistically and numerically the location of the cloud within a coordinate system fixed to the earth over a time period of several days, it would be necessary to develop an isentropic trajectory-forecasting scheme and to incorporate this scheme into a multi-level numerical weather-prediction model. To our knowledge, this has never been done. What will be done here is to attack the second problem; that is, the prediction of the time and space variation of pollutants with respect to a coordinate system that travels with the cloud.

The cloud size of interest is from a few kilometers initially to a few hundred kilometers at several days. Since upper-air observational stations and the grid

interval in meteorological prediction models have spacings of about 300 km, it is not possible to predict the horizontal wind field with a resolution of less than 300 km. Hence, to include the effect of scales of motion smaller than 300 km, we must formulate a suitable diffusion model (or theory).

The use of diffusion theory implies that the motions responsible for changes in concentration are random. Almost any fluid motion can appear random if observed within the appropriate time or space scales. For instance, the Tiros satellite photographs give evidence that large-scale atmospheric motions are composed of many "eddies." However, it is necessary to examine some of the consequences of using a diffusion theory on space scales of a few kilometers to several hundred kilometers and time scales up to a few days. This will be done here; in addition, the implications of sampling nuclear clouds in the light of diffusion theory will be discussed and a particular diffusion model will be proposed. Since these subjects have been discussed in detail by Crawford,^{8,9} only a summary is given here.

TIME AND SPACE SCALES OF DIFFUSION

The classical solutions of various diffusion problems have resulted in Gaussian spatial distributions of concentration. The classical diffusion studies in micrometeorology, where the sources are continuous

point or line sources, have resulted in observed cross-wind Gaussian distributions. It has been observed, though, that the shape of the Gaussian distribution is dependent upon the sampling time of the measurement system.

The "eddies" that are most efficient in diffusion are those of the same size as the plume. Eddies that are much smaller than the plume have a small effect only on the plume shape; eddies that are much larger cause transport instead of diffusion. The looping smoke plume from a chimney is a good example of large eddies transporting but not diffusing the plume.

The observed Gaussian distributions result from operating each sampler on the arc for a time period longer than the period of the "most efficient eddies." In contrast to this result, the casual observation of any smoke plume reveals decidedly non-Gaussian conditions at any one time.

The data collection and analysis for a large cloud becomes much more complicated than for the plume from a continuous point source. Here, the coordinate system travels with the continually changing, deforming cloud. The size of and concentrations in large clouds are usually measured with aircraft-mounted instruments flown through the clouds in a time that is short compared to the time scale of the diffusion processes. For instance, if data were obtained with a space resolution of meters along the flight path in a cloud that was kilometers in size, one would expect the measured concentrations to fluctuate appreciably. Figure 5 in Chapter 3 illustrates the variability to be expected on a small time and space scale within a large cloud. This figure is anal-

ogous to a snapshot of a smoke plume from a chimney versus a time-exposure photograph. These considerations suggest that diffusion-theory predictions will more nearly correspond to space-smoothed parameters like integrated dose through a cloud or cloud area than to concentrations at any one location within the cloud or any one cloud width.

It is a separate, and valid, question whether any diffusion-theory prediction should be expected to fit space-smoothed data from any one cloud at any one time. It seems evident that some time averaging of the space-smoothed diffusion data is required in order to obtain agreement between data and predictions at any one point in time. A specific question then concerns what length of averaging time to use. Assuming that the minimum averaging time should include at least ten of the "most efficient eddies," and assuming that these eddies travel with a mean wind speed of 10 m/sec, the minimum averaging time is comparable to the time since cloud generation for kilometer-sized clouds. Such sampling times would be unsatisfactory because of the removal of time dependency from the problem. It is implied, then, that there will be a departure of space-smoothed data from a diffusion-theory prediction as a function of time, and that much data, taken at different times, needs to be available before comparisons can be made between prediction and theory. These considerations also indicate that a diffusion-theory prediction will do better when compared to the average of many clouds as a function of time than to any one cloud.

It is unfortunate that these conditions are forced upon us, but there is no other

approach feasible due to limitations of wind data. Without closer spacing of observation stations, it is not possible to predict the horizontal spreading of clouds in detail. These considerations do not negate the usefulness of a diffusion prediction, they merely establish that the predictions are statistical in nature. However, a realistic diffusion-prediction model has the advantage that different meteorological inputs can easily be tried; thus, one can investigate the expected range of cloud-concentration histories and/or depositions.

ATMOSPHERIC TURBULENCE AND DIFFUSION

The classical approach to atmospheric turbulence and diffusion characterizes the diffusive properties of the turbulent atmosphere by eddy diffusivities. This is analogous to using kinematic viscosity for momentum fluxes in sheared flow or thermal diffusivities in heat-conduction problems. The eddy diffusivities of atmospheric turbulence are many orders of magnitude larger than their molecular counterparts. For instance, the kinematic viscosity of air is about $0.2 \text{ cm}^2/\text{sec}$, whereas turbulent eddy diffusivities range from 10^2 to $10^{10} \text{ cm}^2/\text{sec}$ in the atmosphere.

If these eddy diffusivities are constant in time and space, as is the case in molecular transfers, then there are a variety of solutions to the basic diffusion equations.

The most appropriate classical solution for this chapter is the instantaneous point source. The basic equation is

$$\frac{\partial X}{\partial t} = \frac{\partial}{\partial r} \left(K \frac{\partial X}{\partial r} \right), \quad (9)$$

where X is the concentration per unit volume, r is the radial distance from the source, t is the time, and K is the eddy diffusivity. If K is truly a constant, it is possible to solve Eq. (9) under the following boundary conditions:

$$X \rightarrow 0 \text{ as } t \rightarrow 0 \text{ for } r > 0,$$

$$X \rightarrow 0 \text{ as } t \rightarrow \infty,$$

and

$$Q = \int_0^\infty X 4\pi r^2 dr.$$

Under these boundary conditions, the solution is

$$X = \frac{Q}{(2\pi\sigma^2)^{3/2}} \exp \left(-\frac{r^2}{2\sigma^2} \right), \quad (10)$$

where

$$\sigma^2 = 2Kt. \quad (11)$$

Equation (11) has been used to determine values of K from the observation of σ at different times.

Comparisons of the Fickian (constant- K) diffusion calculations (instantaneous point source, continuous point source, and continuous line source) with experimental data on diffusion in the atmosphere have consistently shown that the equivalent values of K vary systematically with the time of travel, with position, and with the scale of the diffusion processes.

For the case of an instantaneously produced cloud, Richardson⁹⁶ hypothesized that the rate of separation of pairs of particles (or the spread of a cloud—one particle of the pair being the cloud center) is dependent upon the separation itself. From a variety of data, Richardson found that

$$K = 0.2 \sigma^{4/3}, \quad (12)$$

where σ is the separation between two particles. For cloud diffusion, σ can also be the standard deviation in distance of the concentration along a path through the cloud center. Richardson's data involves σ 's over a range of 10^3 to 10^8 cm. This hypothesis is physically appealing because it implies that the "most efficient eddy" in a diffusion process is the same size as the separation of the particles.

Richardson⁹⁶ implied and Kolmogoroff⁹⁷ developed the concept of a continuous range of eddy sizes in the turbulent atmosphere. Turbulent energy is visualized as being input, at a constant rate, into the large eddies and then handed down from the larger to the smaller eddies and ultimately consumed in viscous dissipation. Kolmogoroff⁹⁷ proposed that there is a range of eddy sizes in the atmosphere called the inertial subrange, in which the eddies are smaller than the eddy size of energy input to the atmosphere and larger than the eddy size of energy lost. The turbulence characteristics of the initial subrange can be completely defined or characterized by the turbulent dissipation. From this hypothesis follows many predictions about the characteristics of atmospheric turbulence. These predictions are known as the predictions of similarity theory.

Batchelor⁹⁸ was one of the first to apply similarity theory to the atmospheric diffusion of a cloud. If $\sigma(t)$ is the separation of a pair of particles (one of which is the cloud center), then Batchelor shows that

$$\frac{d\overline{\sigma^2(t)}}{dt} = 2 C_1 t (\epsilon \sigma_0)^{2/3} \left(1 + \frac{1}{3} \frac{\sigma_0^2}{\ell_0^2} \right) \quad (13)$$

for early times where diffusion is only a function of t , σ_0 (initial separation), and ϵ (turbulent dissipation). The last term of Eq. (13) allows for the fact that σ_0 may not lie on the axis along which σ is evaluated; ℓ_0 is the component of σ_0 along this axis. If $\sigma_0 = \ell_0$, then Eq. (13) becomes

$$\frac{d\overline{\sigma^2(t)}}{dt} = 2.66 C_1 t (\epsilon \sigma_0)^{2/3}. \quad (14)$$

The C_1 is a constant of order unity that results from the dimensional analysis. The bar over $\sigma^2(t)$ indicates that it is the average of many pairs of particles that are expected to follow Eqs. (13) and (14).

Integrating Eq. (14) from $t = 0$ to $t = t$ gives

$$\overline{\sigma^2(t)} = \sigma_0^2 + 1.33 C_1 (\epsilon \sigma_0)^{2/3} t^2. \quad (15)$$

As time increases, finally $\sigma^2(t) \gg \sigma_0^2$ and the diffusion processes become independent of the way in which the particles were initially released. As long as the distance between particles is still small enough so that further dispersion is a result of eddies within the inertial subrange, then dimensional analysis indicates that

$$\frac{d\overline{\sigma^2(t)}}{dt} = C_2 \epsilon t^2, \quad (16)$$

where C_2 is another nondimensional constant of order unity. Integrating Eq. (16) from t_1 (the time at which Eq. (15) is no longer applicable) to t gives

$$\overline{\sigma^2(t)} = \sigma_1^2 + \frac{C_2}{3} \epsilon t^3, \quad (17)$$

where σ_1 is the value of σ at t_1 .

Dimensional arguments give

$$t_1 = C_3 \sigma_0^{2/3} \epsilon^{-1/3}, \quad (18)$$

where C_3 is another nondimensional constant of order unity.

The pertinent variables in this dimensional analysis of turbulent diffusion within the inertial subrange are σ_0 , t , and ϵ . Since diffusivity is not dependent upon the time of release,

$$K \propto \epsilon^{1/3} \sigma_0^{4/3} \quad (19)$$

initially. At any other time, then,

$$K = C_4 \epsilon^{1/3} \sigma^{4/3}, \quad (20)$$

where C_4 is another nondimensional constant of order unity. Thus, similarity theory results in the same form of K as Richardson⁹⁶ deduced empirically (see Eq. (12)).

Similarity theory also predicts that the power spectrum of turbulence is given by

$$E(\kappa) = C_5 \epsilon^{2/3} \kappa^{-5/3}, \quad (21)$$

where E is the power spectrum, C_5 is a nondimensional constant of order unity, and κ is the wave number. Equation (21) can also be rewritten in terms of wave length and in terms of frequency. The various forms of Eq. (21) have been more widely used than the diffusion equations to investigate the validity of similarity-theory predictions in the atmosphere. This is the reason for its presentation here.

Before proceeding with the use of similarity theory in a numerical-diffusion model, it is desirable to say something about its applicability to atmospheric diffusion. There are several questions which have to be answered:

- What is the smallest eddy size to which similarity theory applies?
- What is the largest eddy size to which similarity theory applies?
- How well do similarity-theory predictions agree with data within the eddy size range for which it is applicable?

Batchelor⁹⁸ suggests that the small-size end of the initial subrange is an eddy size on the order of 1 mm. Clearly, this is small compared to the space scales being considered in this chapter.

The large-eddy end of the initial subrange is not as well known. Crawford⁹ has extensively reviewed the literature on the applicability of similarity-theory predictions to atmospheric energy spectra and to atmospheric diffusion. This review is only summarized here. The various energy-spectra studies indicate that the large eddy size limit of the initial subrange for vertical turbulence is about twice the height of the measuring instrument above the ground. For horizontal turbulence (turbulence is defined as random variations within the sampling-time framework used), there are energy peaks for eddies having periods of 50 to 200 hr (1800- to 7200-km wave lengths if an average eddy speed of 10 m/sec is used). This is the scale of large synoptic storms and is a physically reasonable upper limit for a horizontal eddy size in the earth's atmosphere. This size is also consistent with the maximum horizontal-diffusivity values

of 1 to 3×10^{10} cm²/sec (see Eq. (12)) given by many investigators.

The various turbulent-energy-spectra studies indicate a more or less continuous decrease in turbulent energy with decreasing eddy size. The wave-number dependency (see Eq. (21)) for these energy spectra ranges from about -1.0 to -2.4 , so the $-5/3$ law lies about in the middle of the range. It should be remembered that there may be distortions in each spectral study due to instrument errors and limits on averaging and sampling times. It is conceivable that there may be a "gap" in eddy sizes at any one time or location; however, the studies indicate that all eddy sizes exist at some time. Thus, it is reasonable to expect, on the average, some sort of order in the turbulence data as a function of wave number.

The diffusion predictions of similarity theory have not been as well studied in the atmosphere as the turbulent-energy-spectra predictions. There have been a few diffusion studies of clouds of pollutants on space scales up to a few tens of meters and time periods of a few minutes that have been analyzed within a similarity-theory framework. Beyond that, systematic studies of clouds of pollutants or the dispersion of many balloon pairs within any one large cluster have not been done for long enough periods of time to compare with similarity-theory predictions of diffusion. Crawford⁹ summarized the existing data on cloud (or balloon-cluster) diffusion and showed that the available data are consistent with the predictions of similarity theory when reasonable values of turbulent dissipation are used and when the effect of the initial cloud size is included.

Lastly, several widely different studies have shown that Richardson's⁹⁶ equation fits data for a σ between 1.0 and 10^6 to 10^8 cm. This is consistent with similarity-theory predictions.

Thus, there is certainly strong evidence, within the limits of our knowledge, that similarity-theory predictions are applicable on a large scale if the sampling time is consistent with the time scales of the turbulent processes. Similarity predictions do a more realistic job of predicting the time and space behavior of large clouds than does the Fickian diffusion approach. Obviously, there is an upper limit to the diffusivities that should be permitted in the atmosphere. For horizontal diffusion, a variety of studies have indicated that a reasonable upper limit is about 10^{10} cm²/sec. Similarity-theory predictions of atmospheric diffusion require several days before a diffusivity of this value is reached.

For kilometer-sized clouds near the earth's surface, the similarity-theory approach gives values for vertical diffusivities that are too large to be credible in the surface boundary layer. Several studies have indicated maximum vertical-diffusivity values on the order of 10^5 cm²/sec in the troposphere above the surface boundary layers. Many micrometeorological studies have indicated vertical-diffusivity values of about 10^3 cm²/sec near the earth's surface. For clouds initially a kilometer or so in thickness, a similarity-theory approach would give unrealistically large values of more than 10^5 cm²/sec for vertical diffusivity. Consequently, in the development of a numerical model of large-scale diffusion, it was decided to use as input specifications the

vertical diffusivity as a function of height and time.

NUMERICAL DIFFUSION MODEL

It is assumed that the cloud's shape is approximated by a right cylinder. Thus, circular symmetry is assumed and the differential equation to be numerically integrated is

$$\frac{\delta X}{\delta t} = K_r \left(\frac{\delta^2 X}{\delta r^2} + \frac{1}{r} \frac{\delta X}{\delta r} \right) + \frac{\delta}{\delta z} \left(K_z \frac{\delta X}{\delta z} \right), \quad (22)$$

where X is the concentration per unit volume, r is the horizontal radial distance from the cylindrical axis, z is the vertical distance from the ground surface, K_r is the radial diffusivity, and K_z is the vertical diffusivity. Radial diffusivity is assumed to be independent of height, and vertical diffusivity is independent of the radial distance from the cloud center. Radial diffusivity is computed from the similarity-theory approach outlined in the preceding section, and K_z can be arbitrarily specified as a function of time and height.

The general form of the forward-time-step finite-difference equation used to approximate Eq. (22) is

$$X_{j,k}^{n+1} = X_{j,k}^n + \Delta t K_r^n \times \left[\frac{(X_{j+1,k}^n + X_{j-1,k}^n - 2X_{j,k}^n)}{(\Delta r)^2} + \frac{1}{r_j} \frac{(X_{j+1,k}^n - X_{j-1,k}^n)}{2\Delta r} \right]$$

$$+ \Delta t K_{z_k}^n \frac{(X_{j,k+1}^n + X_{j,k-1}^n - 2X_{j,k}^n)}{(\Delta z)^2} + \Delta t \frac{(K_{z_{k+1}}^n - K_{z_{k-1}}^n)}{2\Delta z} \times \frac{(X_{j,k+1}^n - X_{j,k-1}^n)}{2\Delta z}. \quad (23)$$

However, the exact equation used at any particular point in the r, z (j and k indexes respectively) grid or in time depends on the boundary conditions. The grid system contains 50 grid points in the vertical direction and 100 grid points in the horizontal direction; this is a total of 5000 points. The vertical grid point associated with the cloud center is externally specified. There are 121 grid points within the initial cylindrical cloud—11 in the vertical direction and 11 in the radial direction. For reasons of computing-time economy, and in order to maintain the cloud within the grid, the grid system grows outwardly from the cloud center with time. When the top or the bottom grid point reaches the top of the atmosphere or the ground level respectively, the growth of the vertical grid system is stopped in that direction and a reflection boundary condition is assumed. Prior to the grid system reaching a boundary, a "sink" boundary condition is assumed. It should be noted that the elevations of the ground surface, the cloud center, and the top of the atmosphere are input parameters and can be arbitrary functions of time.

In this numerical model, the diffusive properties of the atmosphere are characterized by the values of K_r and K_z . Horizontal diffusivity (K_r) is computed as a function of time from the predictions of similarity theory (Eqs. (12), (14), (16), and (18)). The σ_0 comes from the initial cloud radius and ϵ is externally specified. The ϵ can be an arbitrary function of time because Eqs. (14) and (16) are numerically integrated.

The details of K_z as a function of height and time are externally specified. Figure 52 gives K_z as a function of the height relationship that is currently being used. The K_z increases linearly with height in the boundary layer and then is

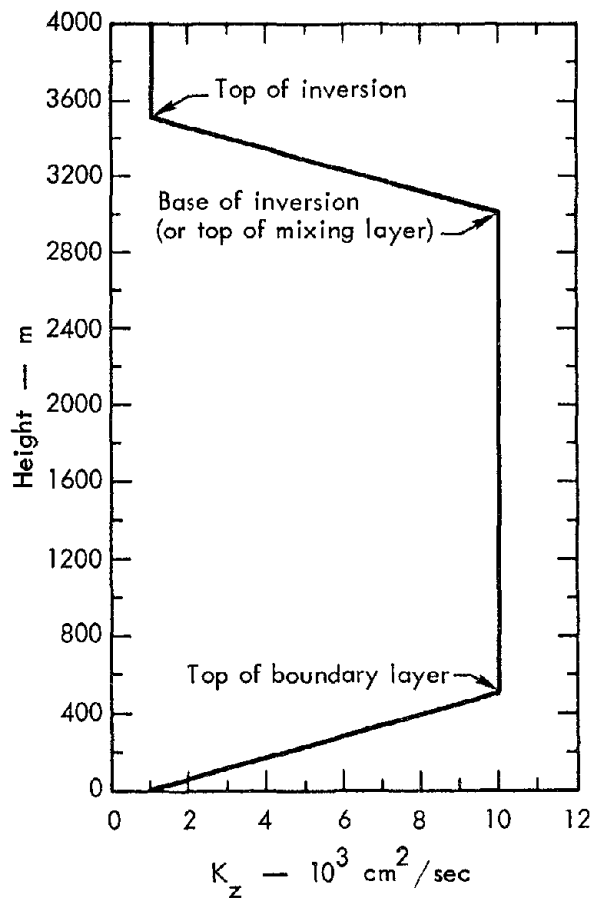


Fig. 52. Vertical diffusivity (K_z) as a function of height.

held constant with height until it reaches a stabilizing inversion. It is implied that the environmental lapse rate is almost dry adiabatic up to the stabilizing inversion. At the stabilizing inversion, vertical diffusivity decreases with height until it reaches a prescribed "ambient" value for the free atmosphere. The depth of the boundary layer, the altitude of the base of the stabilizing inversion, the altitude of the top of the stabilizing inversion, the value of K_z at 1 m above the ground, the value of K_z immediately above the top of the boundary layer, and the value of K_z above the stabilizing inversion are all externally specified. In the latest version of this computer code, these parameters, together with time, the altitude of the ground, the height of the cloud center, the atmospheric dissipation, and the rainfall rates are read in as an input table. Thus, all of these parameters can be made arbitrary functions of time. The code linearly interpolates between values specified at discrete time intervals in this table. It is obvious that all of these K_z parameters are not well measured for any one particular event. However, all of the details of K_z that are so important for micrometeorological calculations are not as important for predicting the gross characteristics of the large clouds of interest in this paper. By an examination of radiosonde data and judicious use of micrometeorological studies in the surface boundary layer, reasonable estimates of these K_z parameters can be made for any particular event. Although the details of the K_z parameters are not very important for the problem at hand, the gross features are significant.

In the numerical solution of the finite-difference analogues of differential equations, there are several sources of error that arise: (1) truncation—both space and time, (2) computational instability, and (3) rounding-off errors. Crawford⁹ discusses these errors in detail with respect to this particular code. It is sufficient to say here that the numerical errors in this computer code are small.

There are several nondiffusive depletion mechanisms included in this code. Even a nonfalling cloud loses some material to the ground by the impaction of submicron particles on vegetation or by the absorption of the gases by vegetation. The concept of a deposition velocity has been introduced in order to treat this form of deposition. The deposition velocity is defined by

$$V_d = \frac{F}{\bar{X}_{sfc}}, \quad (24)$$

where V_d is the deposition velocity (in cm/sec), F is the flux (in mass/cm²/sec) downward, and \bar{X}_{sfc} is the atmospheric concentration at the ground surface (in mass/cm³).

The value of V_d is a function of the turbulence in the lower atmosphere, the physical state of the cloud material, and the ground-surface characteristics. The V_d can be directly determined by measuring the terms of the right-hand side of Eq. (24). This has been done using continuous plumes. Values of V_d range from 10⁻¹ to 10⁺¹ cm/sec,⁹⁹⁻¹⁰¹ with most of the reported values being quite close to 1 cm/sec. In the numerical model of this chapter, V_d is an input parameter.

If the cloud has diffused to the ground so that \bar{X}_{sfc} is not zero, the code inte-

grates Eq. (24) over Δt to calculate the mass removed from the cloud by deposition. Then, the concentrations throughout the lowest one-half vertical grid increment of the cloud are reduced to be consistent with the mass removed at each particular radial distance from the cloud center.

Precipitation is another nondiffusive depletion mechanism. The general equation for the change in concentration due to rain falling through a cloud of particles (or gas) is given by

$$X = X_0 e^{-\Lambda t}, \quad (25)$$

where X_0 is the concentration at the time the rain starts, Λ is a washout coefficient, and t is the time since the rain started. In the code, Δt is substituted for t in Eq. (25) and the concentration at every grid point in the cloud is reduced by Eq. (25) for every time cycle in the code when there is some rain. The top of the rain as well as the inner and outer radii of the "ring" of rain can be externally specified. The rain either has to cover the entire cloud or be a ring of rain due to the assumption of circular symmetry. The main physical difficulty in this rain option is the specification of a realistic washout coefficient (Λ). This washout coefficient is a function of the particle size within the cloud, the chemical composition of the particles, the rainfall rate, and the density of the particles. There have been some empirical studies relating Λ to rainfall rate for different particle sizes and densities in the cloud. The results of most of these studies can be approximated by

$$\Lambda = A \text{ Rain}^B, \quad (26)$$

where A and B are empirically determined constants and Rain is a rainfall rate. In this code, A and B are externally specified parameters. A limitation with this option in the code is that A and B normally only refer to one particle size in the cloud. In reality, most pollutant clouds have a particle-size spectrum.

This code also has a radioactive-decay option. A t^{-n} type of radioactive decay can be assumed for both the cloud and for any material deposited by the cloud on the ground. The outputs of the code are then given in units of concentration of radioactivity instead of in units of mass concentration. The exponent n is externally specified.

PARAMETER SENSITIVITY AND A SAMPLE PROBLEM

One of the most useful features of numerical models of atmospheric processes is the ease with which one can investigate the influence of particular parameters on the end results. Some parameters have been studied with this model and are summarized here; other parameters are yet to be studied.

The larger the initial cloud radius, the larger is the initial K_p , the initial size terms in the similarity-theory equations, and the time before transition from one similarity-theory regime to another. Calculations done on a one-dimensional version of this code, for radial diffusion only, indicated that a difference of a factor of 3 in initial size make a difference of a factor of about 10 in the final concentration at some point late in time. The larger the initial cloud, the larger is the concentration at late times if both clouds start with the same initial concentration. The initial

concentration is inversely proportional to the square of the radius of the initial cloud; thus, if the predicted initial cloud radius is overestimated by a factor of 3, then the initial cloud concentration is too low by a factor of 9. However, a cloud whose radius is a factor of 3 too large will have a concentration after 24 hr that is high by a factor of about 10. Thus, the errors in predicting the initial cloud size, as far as establishing an initial concentration is concerned, are about equally compensated for by the size effect on the diffusion calculation. At late times, the σ for an initial cloud with a radius of 10 m is about the same as the σ for an initial cloud with a radius of 1 km. Thus, for the same initial cloud burden, an initial 1-m-radius cloud will have about the same concentration as an initial 1-km-radius cloud after several days. This is fortunate because it is often easier to predict the total amount of pollutant released in a particular event than it is to predict the initial cloud concentration.

The important atmospheric parameter for radial diffusion is atmospheric dissipation (ϵ). The one-dimensional version of this code was run for four different values of ϵ . This computation indicates that a change of an order of magnitude in the atmospheric dissipation ultimately makes a difference of a factor of about 4 in the concentration.

Vertical diffusion is controlled by the form of K_z used and by the depth of the initial cloud. The relationship of the initial cloud depth to the depth of the diffusing layer determines the ultimate possible dilution of the cloud due to vertical diffusion only. Thus, with a total cloud depth of 1 km and a tropopause height of

10 km, there can, at most, be dilution by a factor of 10 due to vertical diffusion. In practice, additional inversions besides the tropopause may limit this possible dilution. Thus, it is important to reflect the significant inversion heights in the way one specifies K_z . The other details of the K_z specification influence the concentration history in a vertical plane but do not have much effect on the ultimate dilution. In clouds that are initially below an inversion layer and that are deep compared to the boundary layer, the maximum value of K_z (see Fig. 52) is probably far more influential on the concentration history than any of the other details of the K_z profile.

Calculations have been done to investigate the importance of the maximum value of K_z with a boundary layer of 500 m, an inversion base of 1.8 km, an inversion top of 3.4 km, and an initial cloud extending from 1.2 to 1.9 km above the ground. These calculations indicate that a change of an order of magnitude in the maximum K_z results in a difference of a factor of 2 in the center-point concentration at the end of one day. This factor of 2 strictly applies only to the above example. It should also be mentioned that a deposition velocity of 0.5 cm/sec was in effect during these computations.

The K_z specification affects cloud depletion due to deposition velocities because of the K_z influence on the ground-level air-concentration history. However, it can be shown⁹ that for large clouds over a period of a few days, cloud depletion due to reasonable values of deposition velocity are small. For instance, if a cloud with a depth of 1 km is assumed to

be initially based at the ground surface, and if a deposition velocity of 0.5 cm/sec is used, then the cloud burden is only reduced by about a factor of 3 in about two days due to deposition only.

It was mentioned earlier that a t^{-n} type of radioactive decay is an option in this code. The consequences of the use of this option are obvious.

In order to illustrate the capabilities and the outputs of this computer code, the following sample problem is presented. The input parameters are not necessarily consistent with diurnal atmospheric variations. They are chosen here to exercise, in a simple manner, all of the various options of the code.

An initial cloud radius of 1 km and an initial cloud depth of 1 km are assumed. The cloud center is at the tenth grid point in the vertical direction. The top of the atmosphere is assumed to be at 9.5 km, and the cloud is assumed to be moving horizontally with a speed of 5 m/sec. A deposition velocity of 1 cm/sec is used to remove material from the cloud after the cloud has diffused to the ground. Rainfall is assumed to scavenge material from the whole cloud. In other words, the top of the rain is at the top of the atmosphere and the horizontal extent of the rain encompasses the total horizontal extent of the cloud. In the specification of the wash-out coefficient (see Eq. (26)), values are chosen to be consistent with a $a^2\rho = 42$, where a is the particle radius (μ) and ρ is the particle density (g/cm^3).¹⁰² For particles with a density of 2.5 g/cm^3 , this Λ is applicable for particles approximately 4μ in radius. The constant n in a t^{-n} radioactive decay is arbitrarily assumed

to be 0.5. (A larger n in combination with the rain would have run the predictions off of the graphs.)

The various meteorological parameters that are allowed to be functions of time in the computer program are given in Table 8.

The computer code prints out tables and graphs at specified time intervals throughout the calculation and stores other information on magnetic tape to be printed as a function of time after the calculation is completed. Figure 53 gives the concentration of radioactivity ($n = 0.5$) as a function of height through the center point of the cloud at different times. The numbers alongside the lines in Fig. 53 indicate the time (in hours) after the start of the computation. Of interest in this figure are (1) the effect of changing the altitude of the cloud center between 1 and 2 hr; (2) the initial decrease in the center-point concentration by radioactivity decay and radial diffusion; (3) the effect of rain on the concentrations between 14 and 16 hr; and (4) the restriction on the vertical dif-

fusion due to the small vertical diffusivities above the inversion.

Figure 54 is the relative concentration as a function of radial distance from the cloud center. Again, the effect of rain is evident between 14 and 16 hr.

Figure 55 gives the fallout mass per square centimeter as a function of down-wind distance from ground zero. In this case, the cloud and specifically the bottom grid point had not diffused to the ground surface until between 7 and 8 hr. At this time, the deposition process started removing material from the cloud. This is evident in Fig. 55. As time went on, the cloud continued to move away from ground zero and material continued to be deposited on the ground.

At the same time, the material on the ground underwent radioactive decay. Again, the effect of the rain, which started at 13.9 hr, is clearly apparent in Fig. 55. As would be expected, the first few minutes of rain had a much more significant effect on the deposited mass than on the

Table 8. Input for the sample problem.

Time (hr)	Ground- surface elevation (10^4 cm)	Cloud- center elevation (10^5 cm)	K_z at 1 m (10^3 cm ² / sec)	Depth of boundary layer (10^5 cm)	K_z above boundary layer (10^4 cm ² / sec)	Base of inversion elevation (10^5 cm)	Top of inversion elevation (10^5 cm)	K_z above inversion (10^3 cm ² / sec)	ϵ (erg/ g/sec)	Rainfall rate (mm/hr)
0	1.0	2.5	1.0	0.5	1.0	4.0	5.0	1.0	0.1	0
1	5.0	2.5	1.0	0.5	1.0	4.0	5.0	1.0	0.1	0
2	5.0	1.8	1.0	0.5	1.0	4.0	5.0	1.0	0.1	0
3	5.0	1.8	1.0	0.5	1.0	4.0	5.0	1.0	0.1	0
4	5.0	1.8	1.0	1.0	1.0	4.0	5.0	1.0	0.1	0
5	5.0	1.8	1.0	1.0	5.0	4.0	5.0	1.0	0.1	0
6	5.0	1.8	1.0	1.0	5.0	4.5	5.0	1.0	0.1	0
7	5.0	1.8	5.0	1.0	5.0	4.5	5.5	1.0	0.1	0
8	5.0	1.8	5.0	1.0	5.0	4.5	5.5	5.0	0.1	0
9	5.0	1.8	5.0	1.0	5.0	4.5	5.5	5.0	1.0	0
13.9	5.0	1.8	5.0	1.0	5.0	4.5	5.5	5.0	1.0	0
14	5.0	1.8	5.0	1.0	5.0	4.5	5.5	5.0	1.0	10
15	5.0	1.8	5.0	1.0	5.0	4.5	5.5	5.0	1.0	10
15.1	5.0	1.8	5.0	1.0	5.0	4.5	5.5	5.0	1.0	0
60	5.0	1.8	5.0	1.0	5.0	4.5	5.5	5.0	1.0	0

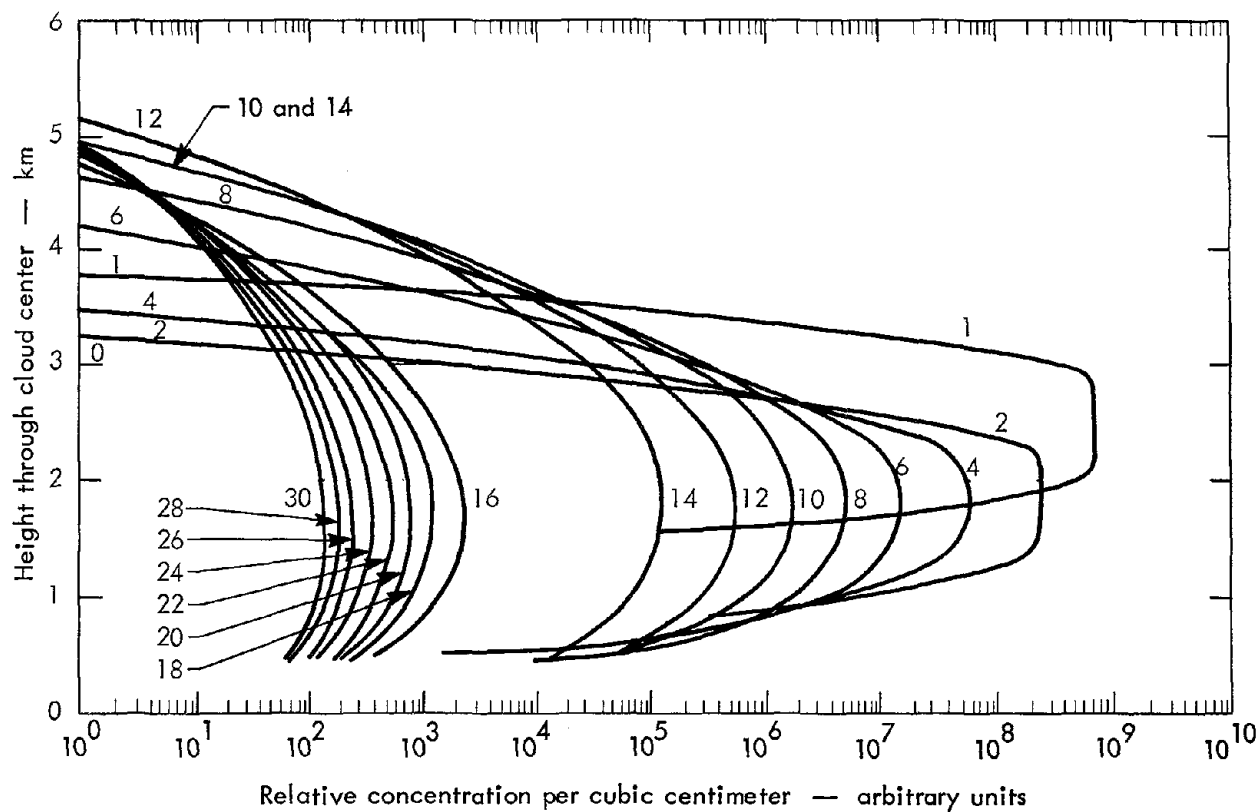


Fig. 53. Relative concentration as a function of the height through the cloud center at different times.

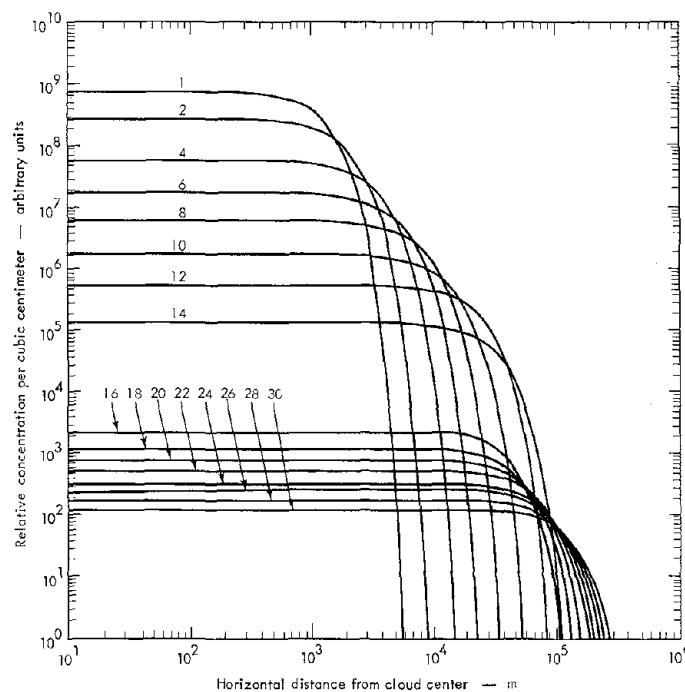


Fig. 54. Relative concentration as a function of the horizontal distance from the cloud center at different times.

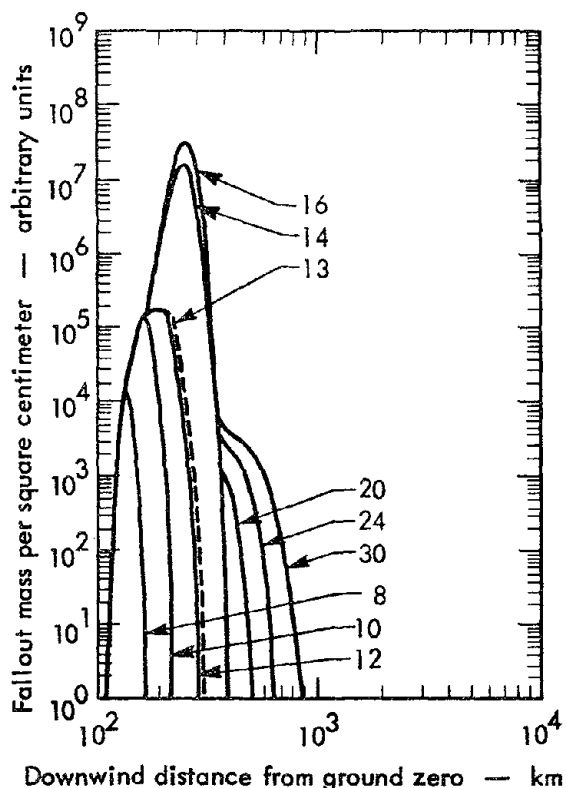


Fig. 55. Deposited mass per square centimeter along the cloud center line at different times.

concentrations. As the rain continued, the concentrations continued to decrease while the mass was more slowly accumulated on the ground. After the rain stopped at 15.1 hr, the cloud continued to move downwind and material continued to be removed from the cloud by deposition. By 30 hr, radioactive decay had shifted the left-hand side of the deposited pattern slightly to the right, but it was not possible to draw the slight shift clearly in Fig. 55. The above three figures (Figs. 53, 54, and 55) are output from the code at specified time intervals during the computation. The individual outputs are obviously single-curve drawings.

At the end of the computation, various information that has been stored on magnetic tape is plotted as a function of time.

This is shown in Figs. 56 through 63, which are self-explanatory. In all of these figures, units of concentration of radioactivity were used because the option of a t^{-n} type of radioactive decay was employed throughout this computation.

Lastly, it should be mentioned that this code takes 1 to 2 hr of IBM-7094 computer time to diffuse a realistic large cloud over a period of 1 to 2 days.

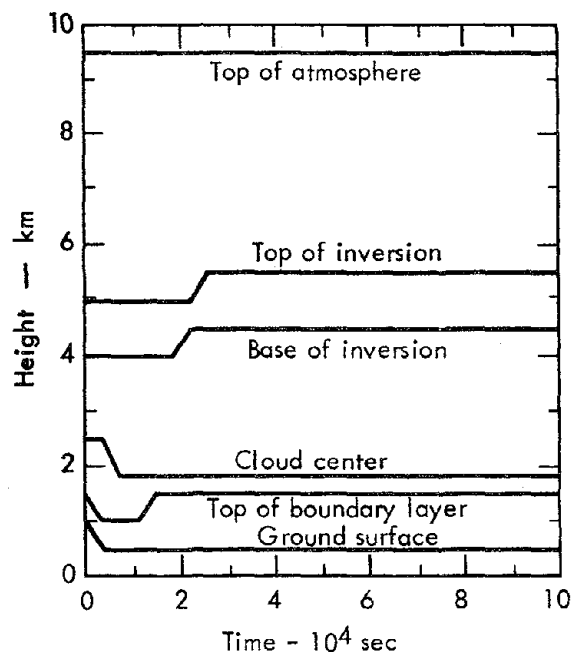


Fig. 56. Input geometry as a function of height and time.

CONCLUDING REMARKS

Limitations in available wind data require a diffusion-theory approach to the problem of predicting the time and space behavior of kilometer-sized clouds for several days. Consequently, the predictions are only expected to apply in a statistical sense. Space-smoothed quantities are expected to be better predicted than are localized quantities, and the averaged time-dependent behavior of many clouds

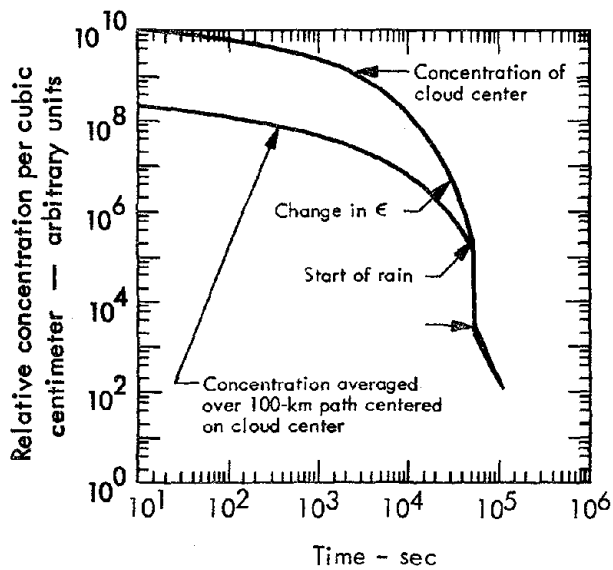


Fig. 57. Center-point concentration as a function of time.

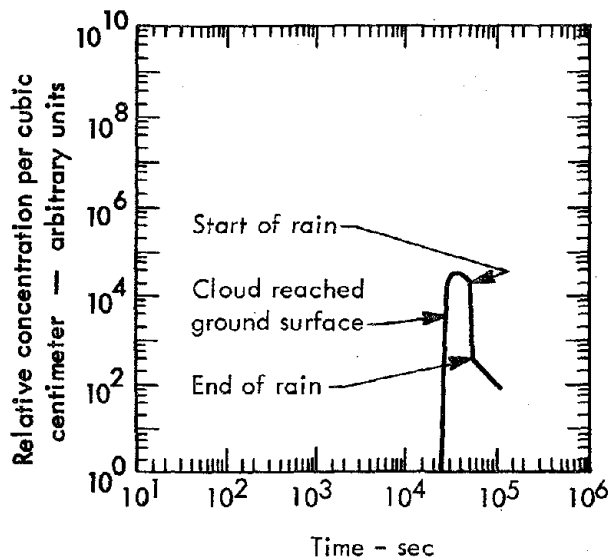


Fig. 58. Ground-surface concentration under the cloud center as a function of time.

is expected to be better predicted than is the time-dependent behavior of any one cloud.

A numerical diffusion model has been developed that uses similarity theories of atmospheric turbulence for horizontal diffusion and permits the use of time- and

height-dependent vertical diffusivities. Although not vindicated for diffusion of kilometer-sized clouds, similarity-theory predictions are consistent with available atmospheric data.

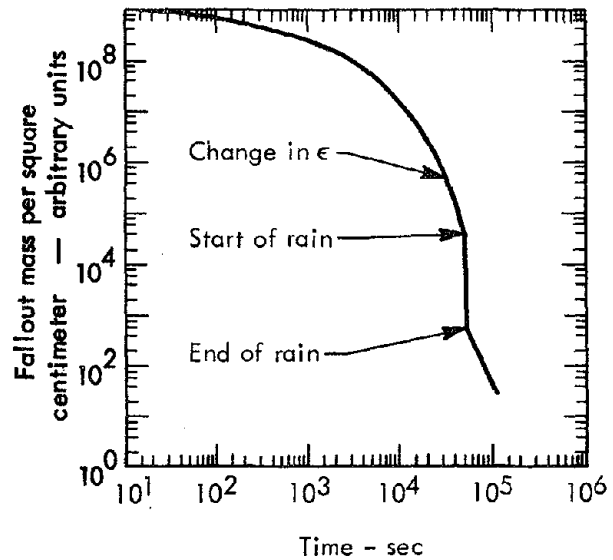


Fig. 59. Vertical summation of mass through the cloud center as a function of time.

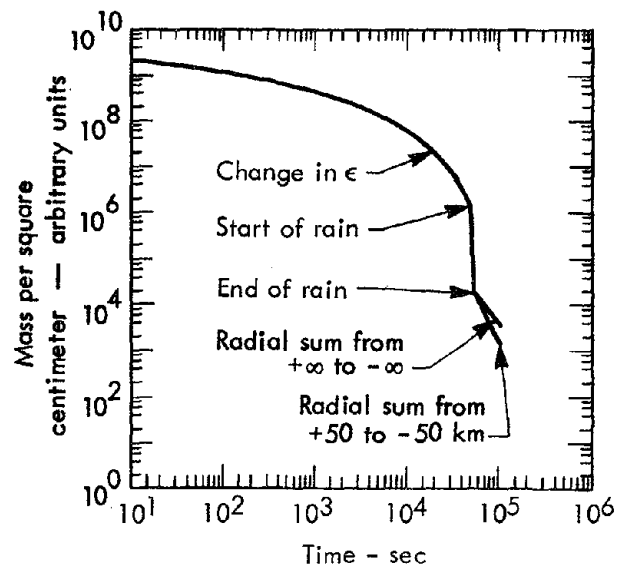


Fig. 60. Horizontal summation of mass through the cloud center from $-\infty$ to $+\infty$ and over a specified path (100 km in this example) centered on the cloud center as a function of time.

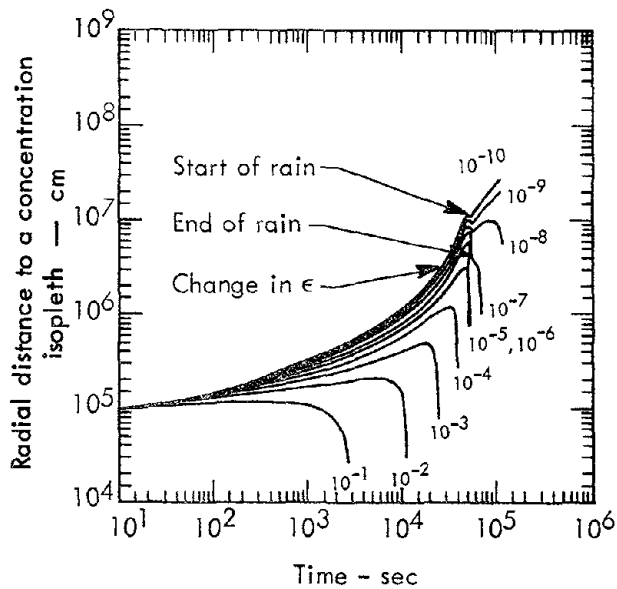


Fig. 61. Radial distance to an isopleth of concentration at the altitude of the cloud center as a function of time. The numbers alongside the lines indicate the particular concentration used to define that isopleth.

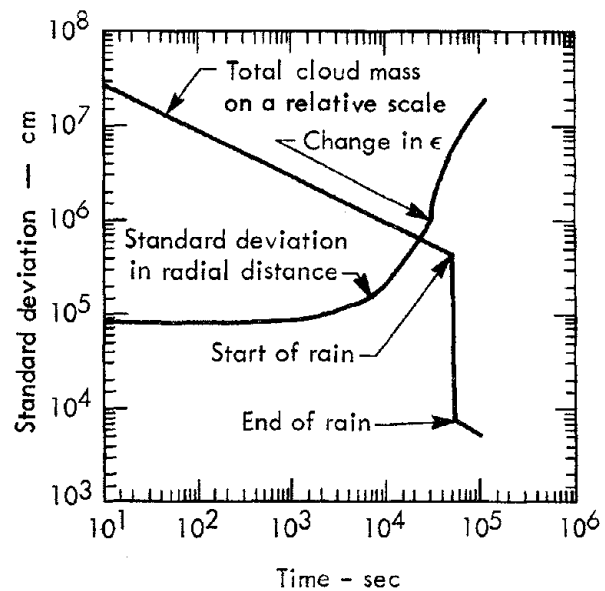


Fig. 63. Horizontal σ ($\sigma_0^2 = 0.68 R_0^2$, where R_0 is the initial cloud radius) as a function of time. This is the similarity-theory prediction. The total cloud mass is also given on a relative scale as a function of time. The initial decrease in the total mass is due only to radioactive decay.

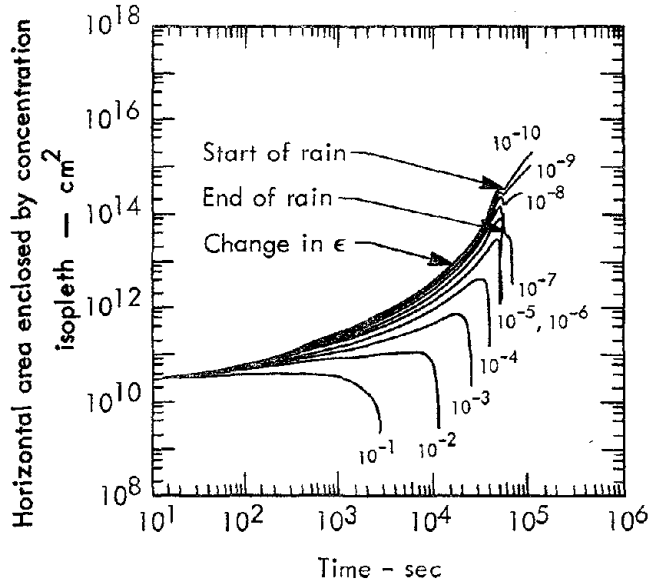


Fig. 62. Horizontal area (circular) enclosed by an isopleth of concentration at the altitude of the cloud center as a function of time. The numbers alongside the lines indicate the particular concentration used to define that isopleth.

Depletion by ground deposition and rainfall has been included in the model, but the diluting effects of vertical shears in the horizontal wind field have not yet been included.

Parameter studies have indicated that the effect of any one atmospheric parameter is not too important in a long-time concentration calculation. It is obvious, though, that elimination of many of the real physical parameters in this model would have a significant effect on predictions. It also is evident that for a particular project or event, this computer code could be used with several physically realistic values of atmospheric parameters to investigate the possible range in cloud concentrations as a function of time.

Vindication of this code with a few case studies has not yet been done. This will be difficult because of the statistical nature of the predictions and because adequate measurements of the meteorological and cloud parameters do not exist. There have been few measurements of K_z and ϵ outside the boundary layer. In the analysis of aircraft concentration data, caution must be exercised in evaluating apparently slow diffusion caused by using averaging paths that are long compared to cloud size and by having

a finite threshold of sensitivity in the measurement technique. On the other hand, missing the cloud when collecting the sample and nondiffusive depletion mechanisms not presently considered in the code would give the appearance of faster diffusion.

(Case studies of two reactor rocket tests and three Plowshare cratering experiments have been done since this chapter was first written. For details, contact T. V. Crawford, Lawrence Radiation Laboratory, Livermore.)

Chapter 9: Hot-Spot Mechanisms

Joseph B. Knox

This section covers the physical processes that contribute to the creation of hot-spots in the fallout at close range and/or in the deposition pattern at longer ranges. By "hot-spot" we mean the deposition of radioactive material in amounts that exceed those in the surrounding area by at least a factor of 2 due to processes enhancing deposition. In addition to describing the physical processes contributing to hot-spots, we shall rank them in order of importance by estimating the magnitude of the enhancement from experimental data and calculations.

Consider the Danny Boy Event (a 0.42-kt nuclear explosive detonated in basalt at an optimal depth of burial). The nuclear-explosive package for this event had a mass of about 3 tons, the mass of shock-vaporized rock was about 24 tons, and the mass of ejected material was about 80,000 tons. From studies of mass deposition and fallout, we know that about 5% of the ejecta and vaporized material appeared in the close-in fallout pattern (about 4000 tons of material). The radionuclides constituting a small fraction of the 4000 tons of airborne debris may be considered either as associated with the fine ejecta in the form of silicates or as independent particles. Recent experimental evidence has tended to confirm that radioactive material is in fact associated with two different particle-size distributions.¹⁵ Such particles may serve as nucleation centers, hence our interest in cloud-physics considerations.

Results of recent studies of fallout particles by Hicks¹⁰³ indicate that this latter statement is correct. Hicks calculates the supersaturation required for the hygroscopic fallout particles to serve as nucleation centers. He finds that the required supersaturation is on the order of 0.029%; that is, the same order of magnitude as is required for natural nucleation particles in the atmosphere.

A few key definitions are:

- "Nucleation" is defined as the process by which certain loci (or particles) initiate a phase change of atmospheric water vapor into liquid.
- "Rainout" of particulates or gases is defined only as the removal of particulates and gases from the cloud volume by precipitation elements formed within the cloud.
- "Washout" is defined as the removal of particulates and/or gases from the volume of air beneath the cloud layer from which the precipitation falls.

Although considerable literature related to the production of hot-spots exists, a general review is given by Junge¹⁰⁴ and selective contributions are contained in Ref. 105. An excellent discussion of washout is given by Engelmann¹⁰²; this paper contains the data basic to the inclusion of washout in the numerical-simulation model for atmospheric diffusion (Crawford⁹ and Chapter 8). A case study of the processes of nucleation (growth by agglomeration resulting from Brownian motion

and subsequent growth by coalescence of water drops during sedimentation) for the Baker shot* is given by Hicks and Penney.¹⁰⁶ Hicks and Penney estimated that by means of nucleation, agglomeration, and coalescence, about 90% of the water in the base-surge cloud was precipitated in a period of about 3 min. The rain drops produced at the end of this period were about 2500 μ in diameter. This case study illustrates that under certain conditions, the deposition of water droplets is a significant and rapid process. Some data have recently been given by Larson¹⁰⁷ on the occurrence of orographic

hot-spots for Operation Plumbbob. These papers serve in part as a basis for our discussion here.

ENUMERATION OF HOT-SPOT MECHANISMS

The hot-spot-producing mechanisms that may alter the normal fallout patterns from cratering shots are enumerated in Table 9, along with their importance at distances of more than 50 miles from the detonation site. Numerical estimates of the order of magnitude of the last five processes in Table 9 are given in Table 10.

DISCUSSION

From the preceding tables, it appears that rainout and washout of particulates

* A 20-kt device fired 90 ft below the surface of Bikini Lagoon in the 1946 Operation Crossroads.

Table 9. Hot-spot-producing mechanisms.

Mechanism	Important off-site?
Random jets of venting material resulting in lumpiness of the early debris cloud and hence in uneven deposition	No
Massive fallback and ejecta deposition producing streaks of enhanced deposition around or in the crater	No
A ground-level neutral point in the wind field (see Fig. 2) associated with a mesoscale wind system or an orographically induced circulation	Can be
Rainout of particulate and gaseous radionuclides from within natural or debris-cloud volumes; effective for removing particles down to sizes as small as about 0.1 μ	Can be
Washout of particulate and gaseous products from debris clouds beneath natural precipitating clouds; effective only for particles of 4 μ or more	Can be
Field of deformation of the horizontal wind field distorting the debris cloud into a very elongated configuration, hence extending the period of deposition under the major axis of the distorted cloud	Yes
In a thermally stable atmosphere, debris clouds should be transported along isentropic surfaces; if an isentropic surface passing through the debris cloud intersects terrain or surfaces on flat terrain, locally enhanced deposition can occur	Yes

Table 10. Numerical estimates of the last five processes in Table 9.

Data source	Process or mechanism	Enhancement factor ^a	Reference
1. Plumbbob, four shots (NTS)	Orographically induced circulations	2 to 3	Larson ¹⁰⁷
2. Upshot Knothole, Shot 7 (NTS) (Hot-spot, Troy, New York)	Rainout	10 ³ or more	Clark ¹⁰⁸
3. Baker (PPG; estimated from mathematical analysis and observed phenomenon)	Rainout (about 90% of the total water aloft is removed from the base surge in about 3 min by coagulation and gravitational accretion)	Unknown	Hicks and Penney ¹⁰⁶
4. Calculation	Washout	10 ² to 10 ³ (at long range)	Crawford ⁹ and Chapter 8
5. Estimate	Horizontal deformation of the wind	2 to 10 (at intermediate and long ranges)	Knox ¹⁰⁹
6. Calculation	Surfacing of isentropic surfaces	≥10 (at 2 to 3 hr)	Crawford ⁹ and Chapter 8
7. Estimate	Washout of gases and particulates in the base surge during the first hour after detonation	~2	Knox, Crawford and Ellsaesser ¹¹⁰

^aThe enhancement factor is defined as the ratio of "enhanced" radioactivity deposit (or exposure rate) to a typical deposit of radioactivity (or exposure rate) in the vicinity. Exposure-rate comparisons were employed in item 1, radioactivity depositions in items 2, 4, 5, 6, and 7.

are the most important hot-spot-producing mechanisms. This is consistent with the findings of many investigators that the principal process for the removal of fallout from the atmosphere is deposition involving rainout or washout.¹¹¹

In planning a large excavation project, maximum control over the generation of off-site hot-spots is desirable. Thus, periods of rainfall should be avoided. In this regard, Knox et al.¹¹⁰ found, in a preliminary analysis of the proposed Panama Canal excavation, that the maximum frequency of in-sector winds (>5

knots) occurred during the dry season.

The meteorological program associated with site surveys for any excavation project should not only define what an acceptable shot day is, but also ascertain from the data if natural rain occurs on such days.

Recently, a few investigators have made the suggestion that cratering shots detonated during heavy rain might well have enhanced local deposition; that is, more deposition within the exclusion zone and less at intermediate ranges. On the surface, this idea has technical merit;

however, it must be examined thoroughly from the point of view of scaling analysis. The horizontal scale of the nuclear clouds made in Panama will probably be much larger than the scale of the natural convective clouds producing rain. Hence, it is likely that the fraction of fallout material removed within the debris cloud would be spotty. If this is the case, then those parts of the debris cloud that are not entrained and scavenged by rain must have deposition patterns within the exclusion zone. As discussed above, this is improbable during the wet season in Panama.

The idea of detonating a cratering shot during a rain storm has merit only if the rain cell is at least as large in horizontal extent as the debris cloud and the two coincide. Superficially, it would appear that radar climatology of the appropriate areas would answer this question. Provisional information from ESSA indicates that radar-signal attenuation prevents them from obtaining data on precisely this case. Hence, we have no firm data on which to discard or accept the idea of shooting in a rain storm for Panama Canal excavation. It clearly requires significantly more effort to evaluate this suggestion.

The distinction between washout and rainout is a very important one in that washout is ineffective for removing fine particles ($r \leq 3 \mu$), whereas rainout, if it involves nucleation, could be a very effective remover of both fine and large particulates.

The enhancement factors presented above for the various mechanisms do not give information on the fraction of airborne activity that is removed; estimates

of the fraction removed from the atmosphere can come only from calculational models like that given in Chapter 8 or from other "realistic" solutions of the washout equation ($X = X_0 e^{-\Lambda t}$) in a diffusing two-dimensional cloud. In the sample 2BPUFF problem (Chapter 8), the enhancement factor for the washout hot-spot is about 100, while the corresponding fraction of airborne activity removed is about $1 - 1/50$, or 0.98, for the conditions assumed.

It should be noted that the enhancement factor is a function of the geometry of the debris cloud if the other parameters are held fixed. Hence, even if the fraction of a cloud removed by washout were held constant, quite different enhancement factors could occur for clouds of differing heights.

It should also be stressed that the enhancement factor is a function of range—as suggested from the estimates given in Table 10. On-site, or during the first hour of deposition, it is difficult to conceive of hot-spots with a geometrical scale of 10 km that are characterized by an enhancement factor of more than about 2. We support this statement with the following consideration. List¹¹² has studied the hourly rate of deposition of gamma activity for the surface shot, Johnie Boy. If it is assumed that at cloud-stabilization time all of the produced activity is in the cloud, then the fraction of the activity deposited in the close-in pattern as a function of time is as shown in Table 11.

The above simple analysis shows that if precipitation on a scale larger than the Johnie Boy debris cloud had occurred continuously during the first hour of

Table 11. Activity in close-in pattern.

Time interval (hr)	Fraction in dry deposition	Fraction airborne	Fraction of particles subject to washout	Enhancement factor (washout)
0 to 1	0.410	0.590	0.40 (0.70 × 0.59)	1.96 $\left(\frac{0.41 + 40}{0.41}\right)$
1 to 2	0.045	0.545	0.38	9.4
2 to 3	0.024	0.521	0.365	16.2
3 to 4	0.012	0.509	0.355	30.6
4 to 5	0.006	0.503	0.35	59.4
5 to 6	0.005	0.498	0.35	71.0
6 to 7	0.003	0.495	0.345	115.0

deposition, then the gamma-dose-rate intensity would have been increased only about a factor of 2. As stated, the process for wet deposition is washout that does not involve nucleation or entrainment, as does rainout. If rainout were the wet-deposition process, the enhancement factor should be multiplied by 10 or 20 to account for entrainment. The dependency of the enhancement factor on range, shown above, is consistent with experimental data previously cited. The above estimate of the enhancement factor as a function of time for Johnie Boy probably represents a reasonable first estimate of the enhancement factor for cratering shots similar to Sedan, whose early clouds are relatively unfractionated. Hence, we find that if washout occurs on a scale greater than the nuclear debris cloud, about 70% of the activity in the stabilized cloud would be removed by a 5-mm/hr rain, with an increase of less than an order of magnitude in the exposure within the exclusion zone. The other 30% of the activity, on fine particles or as gaseous material, would largely remain

airborne since washout coefficients for gases are significantly lower than for particulates.

In planning for an excavation project, the above assessment of the order of magnitude of various hot-spot mechanisms, together with data from the vicinity of the site on the frequency of occurrence of precipitation (its distribution, intensity, and duration), would provide a basis for analyzing hot-spot production probability with state-of-the-art information. In regard to the prediction of washout and rainout during the execution phase of a large-scale excavation project, the state of the art of predicting the size of precipitating regions of clouds and rates of precipitation prior to the onset of convection is generally poor. Hence, the preshot detailed prediction of the enhancement and distribution of hot-spots from rainout or washout would not be reliable. However, it is believed that a categorical forecast statement such as "for a morning shot time, hot-spots are likely in the afternoon due to showers..." might be attainable. During an actual operation, if

17. T. A. Gibson, Capability of Probability Distributions of $Dr > Dr_1$ (KFOC) Gross Gamma, from Given Climatological Wind Data, unpublished report, Lawrence Radiation Laboratory, Livermore (1964).
18. A. Foldvik and M. G. Wurtele, The Computation of the Transient Gravity Wave, unpublished report, University of California, Los Angeles (1965).
19. J. Viecelli, Explosion of a 500 Megaton Bomb at the Surface of the Earth: A Numerical Calculation of Atmospheric Effects, report UCID-15048, Lawrence Radiation Laboratory, Livermore (1966).
20. J. A. Miskel, "Characteristics of Radioactivity Produced by Nuclear Explosives," Proceedings, 3rd Plowshare Symposium, report TID-7695, Lawrence Radiation Laboratory, Livermore (1964), p. 153.
21. R. A. James, Calculation of Radioactive Iodine Concentrations in Milk and Human Thyroid as a Result of Nuclear Explosions, report UCRL-7716, Lawrence Radiation Laboratory, Livermore (1964).
22. N. A. Bonner and J. A. Miskel, "Radioactivity: Distribution from Cratering in Basalt," Science **150**, 489 (1965).
23. Private communication from J. A. Miskel, Lawrence Radiation Laboratory, Livermore.
24. R. A. James and E. H. Fleming Jr., Relative Significance Index of Radionuclides for Canal Studies, report UCRL-50050, Rev. 1, Lawrence Radiation Laboratory, Livermore (1966).
25. S. Glasstone, Effects of Nuclear Weapons (U.S. Government Printing Office, Washington, D. C., 1962).
26. L. E. Weaver, P. O. Strom, and P. A. Killeen, Estimated Total Chain and Independent Fission Yields for Several Neutron-Induced Fission Processes, report USNRDL-TR-633, U.S. Naval Radiological Defense Laboratory, San Francisco (1963).
27. R. C. Bolles and N. E. Ballou, Calculated Activities and Abundances of U^{235} Fission Products, report USNRDL-456, U.S. Naval Radiological Defense Laboratory, San Francisco (1956).
28. E. H. Fleming Jr., The Fission Product Decay Chains (Pu^{239} with Fission Spectrum Neutrons), report UCRL-50243, Vols. I, II, and III, Lawrence Radiation Laboratory, Livermore (1967).
29. D. W. Dorn, "Mike Results—Implications for Spontaneous Fission," Phys. Rev. **126**, 693 (1962).
30. Private communication from E. F. Plechaty, Lawrence Radiation Laboratory, Livermore.
31. R. L. Macklin and J. H. Gibbons, "Neutron Capture Data at Stellar Temperatures," Rev. Mod. Phys. **37**, 166 (1965).
32. H. Neuert and H. Pollehn, Tables of Cross-Sections of Nuclear Reactions with Neutrons in the 14-15 MeV Energy Range, manual EUR-122, e, University of Hamburg, Hamburg, West Germany (1963).

33. P. Jessen, M. Bormann, F. Dreyer, and H. Neuert, "Experimental Excitation Functions for (n,p), (n,t), (n, α), (n,2n), (n,np), and (n,n α) Reactions," Nucl. Data 1A, 103 (1966).
34. P. J. Brancazio, unpublished thesis, New York University, New York (1966).
35. Private communication from J. W. Truran, Yeshiva University, New York.
36. J. W. Truran, C. J. Hansen, A. G. W. Cameron, and A. Gilbert, "Thermonuclear Reactions in Medium and Heavy Nuclei," Can. J. Phys. 44, 151 (1966).
37. A. G. W. Cameron, N. H. Lazar, and H. W. Schmitt, "Fast Neutron Capture Cross Sections," Fast Neutron Physics (John Wiley & Sons, Inc., New York, 1963), Part II.
38. Private communication from D. W. Dorn, Lawrence Radiation Laboratory, Livermore.
39. Private communication from F. W. Guy, Lawrence Radiation Laboratory, Livermore.
40. Private communication from F. W. Guy, Lawrence Radiation Laboratory, Livermore.
41. R. M. Lessler and F. W. Guy, Gamma Dose Rates and Integrated Doses from Neutron-Induced Residual Radioactivity in Soil, report UCRL-12339, Vol. 1, Lawrence Radiation Laboratory, Livermore (1965).
42. Private communication from J. A. Miskel, Lawrence Radiation Laboratory, Livermore.
43. M. D. Nordyke and M. M. Williamson, The Sedan Event, report PNE-242F, Lawrence Radiation Laboratory, Livermore (1965).
44. Private communication from H. G. Hicks and G. W. Barton Jr., Lawrence Radiation Laboratory, Livermore.
45. Yu. A. Izrael', "Mode of Origin of Radioactive Fallout Particles and the Fractionation of Isotopes in an Underground Nuclear Explosion with Ejection of Ground," Dokl. Akad. Nauk USSR 169, 573 (1966).
46. T. R. Butkovich, The Gas Equation of State for Natural Materials, report UCRL-14729, Lawrence Radiation Laboratory, Livermore (1967).
47. Private communication from T. R. Butkovich, Lawrence Radiation Laboratory, Livermore.
48. R. G. Bedford and D. D. Jackson, Volatilities of the Fission Product and Uranium Oxides, report UCRL-12314, Lawrence Radiation Laboratory, Livermore (1965).
49. J. B. Knox, Water Quality in Flooded Craters Produced by Nuclear Excavation, report UCID-4741, Lawrence Radiation Laboratory, Livermore (1964).
50. T. A. Gibson Jr., Observed Fractionation in Ground Level Fallout from Three Nuclear Cratering Detonations, report UCRL-50409, Lawrence Radiation Laboratory, Livermore (1968).
51. P. W. Krey and R. E. Fried, "Long Range Fallout from Sedan and Small Boy," Radioactive Fallout from Nuclear Weapons Tests, report CONF-765, U.S. Atomic Energy Commission, Washington, D. C. (1965), ed. A. W. Klement Jr., p. 82.

52. H. M. Mark, K. H. Larson, B. W. Kowalewsky, R. A. Wood, D. E. Paglia, and W. A. Rhoads, Project Sedan: Part I. Characteristics of Fallout from a Deeply Buried Nuclear Detonation from 7 to 70 Miles from Ground Zero, report PNE-225F, University of California, Los Angeles (1966).
53. W. B. Lane, Project Sedan: Some Radiochemical and Physical Measurements of Debris from an Underground Nuclear Detonation, report PNE-229P, U.S. Naval Radiological Defense Laboratory, San Francisco (1963).
54. Private communication from L. L. Schwartz, Lawrence Radiation Laboratory, Livermore.
55. J. J. Cohen, Cabriolet Special Cloud Content Studies, report UCRL-50452, Lawrence Radiation Laboratory, Livermore (1968).
56. T. M. Tami and W. C. Day, Predicted Exposure Rates Within the Crater and Lip Areas, technical memorandum NCG/TM 69-7, Nuclear Cratering Group, Livermore (1969).
57. T. V. Crawford, Long-Range Diffusion of the NRX/EST EP-4A Effluent Cloud, report UCRL-50299, Lawrence Radiation Laboratory, Livermore (1967).
58. T. V. Crawford, The Long Range Diffusion of the Effluent Cloud from the Phoebus 1B EP-IV Reactor Test of February 23, 1967, report UCRL-50418, Lawrence Radiation Laboratory, Livermore (1968).
59. J. G. Edinger, The Influence of Terrain and Thermal Stratification on Flow Across the California Coast Line, report AFCRL-TR-60-438, University of California, Los Angeles (1960).
60. M. Todsen, A Computation of the Vertical Circulation in a Frontal Zone from the Quasi-Geostrophic Equations, technical note 4, University of Oslo, Oslo, Norway (1964).
61. J. D. McDonald, "Rates of Descent of Fallout Particles from Thermonuclear Explosions," J. Meteor. 3, 380 (1960).
62. Private communication from P. McCready, Meteorological Research, Inc., Altadena, California.
63. Private communication from J. J. Cohen, Lawrence Radiation Laboratory, Livermore.
64. J. W. Oblanas and R. T. H. Collis, Project Pre-Gondola I: Lidar Observations of the Pre-Gondola I Clouds, report PNE-1110, Stanford Research Institute, Menlo Park (1967).
65. E. S. Batten, D. S. Inglehart, and R. R. Rapp, Derivation of Two Simple Methods for the Computation of Radioactive Fallout, report RM-2460, The RAND Corporation, Santa Monica (1960).
66. Private communication from M. M. Williamson, U. S. Atomic Energy Commission, Washington, D. C.
67. J. B. Knox and R. W. Terhune, Cratering Physics Concepts Derived from an Analysis of Ground Surface Motion, report UCID-4664, Lawrence Radiation Laboratory, Livermore (1963).

68. J. T. Cherry, "Computer Calculations of Explosion-Produced Craters," Int. J. Rock Mech. Min. Sci. 4, 1 (1967).
69. J. B. Knox and R. W. Terhune, "Calculations of Explosion-Produced Craters — High-Explosive Sources," J. Geophys. Res. 70, 2377 (1965).
70. Military Engineering with Nuclear Explosives, manual DASA-1669, Nuclear Cratering Group, Livermore (1966).
71. F. H. Harlow, J. P. Shannon, and J. E. Welch, "Liquid Waves by Computer," Science 149, 1092 (1965).
72. Private communication from W. R. Wray, U.S. Army Corps of Engineers, Washington, D.C.
73. W. C. Dry and R. F. Rohrer, Project Pre-Schooner II: Cloud Development Studies, report PNE-511, Nuclear Cratering Group, Livermore (1966).
74. Private communication from T. R. Butkovich, Lawrence Radiation Laboratory, Livermore.
75. L. J. Vortman, Project Sulky: Close-In Air Blast from a Relatively Deep Low-Yield Nuclear Detonation in Basalt, report PNE-711F, Sandia Laboratories, Albuquerque (1966).
76. Private communication from J. T. Cherry, Lawrence Radiation Laboratory, Livermore.
77. Private communication from G. H. Higgins, Lawrence Radiation Laboratory, Livermore.
78. R. R. Rapp and J. D. Sartor, Rate of Fall Through the Atmosphere of Irregularly Shaped Particles, report RM-2006, The RAND Corporation, Santa Monica (1957).
79. V. G. Khorguani, "The Character and Settling Velocity for a System of Equal Size Particles," Atmos. Ocean. Phys. 2, 234 (1966).
80. M. D. Nordyke and W. Wray, "Cratering and Radioactivity Results from a Nuclear Cratering Detonation in Basalt," J. Geophys. Res. 69, 675 (1964).
81. E. Graves, W. R. Wray, and R. B. Pierce, Project Pre-Buggy: Scope of Chemical Explosive Cratering Experiment, report PNE-300, Nuclear Cratering Group, Livermore (1963).
82. G. A. Young, Base Surge Analysis — HE Analysis, Operation Jangle, report NOLR-1169, U.S. Naval Ordnance Laboratory, White Oak, Maryland (1952).
83. Classification bulletin WNP-11(R), U.S. Atomic Energy Commission, Washington, D. C. (1967).
84. E. Graves Jr., M. D. Nordyke, and L. J. Cauthen Jr., Isthmian Canal Plans — 1964. Annex III, Appendix 1: Nuclear Excavation Plan, report PNE-2000, Nuclear Cratering Group, Livermore (1964).
85. Private communication from H. W. Ellsaesser, Lawrence Radiation Laboratory, Livermore.
86. I. O. Huebsch, The Development of a Water-Surface Burst Fallout Model: The Rise and Expansion of the Atomic Cloud, report USNRDL-TR-741, U.S. Naval Radiological Defense Laboratory, San Francisco (1964).

87. J. S. Malkus and G. Witt, The Evolution of a Convective Element: A Numerical Calculation (Oxford University Press, New York, 1959).
88. D. K. Lilly, "On the Numerical Simulation of Buoyant Convection," Tellus 14, 148 (1962).
89. D. K. Lilly, "On the Inclusion of Turbulent Diffusion in the Numerical Simulation of Moist and Dry Convection," Proceedings, 4th Numerical Weather Prediction Conference (University of California, Los Angeles, 1962).
90. Y. Ogura, "A Numerical Experiment in Shallow Convection in the Atmosphere," Proceedings, 4th Numerical Weather Prediction Conference (University of California, Los Angeles, 1962).
91. H. D. Orville, "A Numerical Study of the Initiation of Cumulus Clouds Over Mountainous Terrain," J. Atmos. Sci. 22, 684 (1965).
92. F. W. Murray and A. B. Hollinden, The Evolution of Cumulus Clouds: A Numerical Simulation and Its Comparison Against Observations, report SM-49372, Douglas Aircraft Company, Inc., Santa Monica (1966).
93. J. B. Knox, "Venting, Air Blast, and Radioactivity," lecture given at Stanford University, Palo Alto (1966).
94. G. Maenchen and S. Sack, "The Tensor Code," Meth. Comp. Phys. 3, 181 (1964).
95. J. Viecelli, "Atmospheric Refraction and Focus of Blast Waves," J. Geophys. Res. 72, 2469 (1967).
96. L. F. Richardson, "Atmospheric Diffusion Shown on a Distance-Neighbor Graph," Proc. Roy. Soc. (London) A110, 709 (1926).
97. A. N. Kolmogoroff, "The Local Structure of Turbulence in Incompressible Viscous Fluid for Very Large Reynolds' Numbers," Dokl. Akad. Nauk USSR 30, 301 (1941).
98. G. K. Batchelor, "The Application of the Similarity Theory of Turbulence to Atmospheric Diffusion," Quart. J. Roy. Meteor. Soc. 76, 133 (1950).
99. F. Pasquill, Atmospheric Diffusion (D. Van Nostrand Company, Ltd., London, 1962).
100. N. F. Islitzer and R. K. Dumbauld, "Atmospheric Diffusion-Deposition Studies over Flat Terrain," Int. J. Air Water Pollution 7, 999 (1963).
101. A. C. Chamberlain, "Aspects of the Deposition of Radioactive and Other Gases and Particles," Aerodynamic Capture of Particles (Pergamon Press, Ltd., New York, 1960), ed. E. G. Richardson, pp. 63-88.
102. R. J. Engelmann, Calculation of Precipitation Scavenging, report BNWL-77, Battelle-Northwest Laboratory, Richland, Washington (1965).
103. B. B. Hicks, "Nucleation and the Wet Removal of Fallout," J. Appl. Meteorol. 5, 169 (1966).
104. C. E. Junge, Air Chemistry and Radioactivity (Academic Press, Inc., New York, 1963), p. 382.
105. Radioactive Fallout from Nuclear Weapons Tests, report CONF-765, U. S. Atomic Energy Commission, Washington, D. C. (1965), ed. A. W. Klement Jr.

106. E. P. Hicks and W. G. Penney, The Base Surge: The Mechanism of Fall-Out, report FWE-19, Atomic Weapons Research Establishment, Aldermaston, England (1954), p. 21.
107. K. H. Larson, Operation Plumbbob: Distribution, Characteristics, and Biotic Availability of Fallout, Operation Plumbbob, report WT-1488, University of California, Los Angeles (1966), p. 276.
108. H. M. Clark, "The Occurrence of an Unusually High-Level Radioactive Rainout in the Area of Troy, New York," Science **119**, 619 (1954).
109. J. B. Knox, An Appraisal of Sources of Error in Calculated Gamma Radiation Fields, internal report SDK 66-32, Lawrence Radiation Laboratory, Livermore (1966).
110. J. B. Knox, T. V. Crawford, and H. Ellsaesser, Introduction and Summary Concerning Meteorological Feasibility of Nuclear Excavation of the Panama Canal, internal report SDK 65-4, Lawrence Radiation Laboratory, Livermore (1965).
111. L. Machta, "Meteorological Processes in the Transport of Weapon Radioiodine," Health Phys. **9**, 1123 (1963).
112. Private communication from R. List, Environmental Science Services Administration, Silver Spring, Maryland.

